DEPARTMENT OF PHYSICS
UNIVERSITY OF JYVÄSKYLÄ
RESEARCH REPORT No. 11/2016

INSTRUMENTATION FOR TIME-OF-FLIGHT ELASTIC RECOIL DETECTION ANALYSIS

BY

JAAKKO JULIN

Academic Dissertation
for the Degree of
Doctor of Philosophy

To be presented, by permission of the
Faculty of Mathematics and Science
of the University of Jyväskylä,
for public examination in Auditorium FYS1 of the
University of Jyväskylä on September 16th, 2016
at 12 o'clock noon

Jyväskylä, Finland
September 2016

ABSTRACT

Julin, Jaakko
Instrumentation for time-of-flight elastic recoil detection analysis
Jyväskylä: University of Jyväskylä, 2016, 80 p. (+included articles)
Department of Physics Research Report No. 11/2016
ISSN 0075-465X
ISBN 978-951-39-6703-1 (paper copy)
ISBN 978-951-39-6704-8 (PDF)
Diss.

Time-of-flight elastic recoil detection is an ion beam based method to analyze the elemental composition of thin film samples at different depths.

In order to improve the mass resolution and to enable kinematic correction a position sensitive gas ionization chamber energy detector was constructed. This detector along with pre-existing timing detectors were connected to a modern fully digitizing data acquisition setup.

This thesis describes the design of these instruments, including all aspects from the mechanical design of the gas ionization detector to the algorithm and software development of the digitizing acquisition setup. The performance of the system has been studied with measurements and Monte Carlo simulations. New methods to study the data acquisition and instrumentation related effects are introduced and these methods are extended to study a proposed low energy time-of-flight ERDA instrument design.

Keywords: elastic recoil detection analysis, time-of-flight, gas ionization chamber, digitizer, digital pulse processing

Author

Jaakko Julin
Department of Physics
University of Jyväskylä
Jyväskylä, Finland

Supervisor

Professor Timo Sajavaara
Department of Physics
University of Jyväskylä
Jyväskylä, Finland

Reviewers

Professor Jyrki Räisänen
Department of Physics
University of Helsinki
Helsinki, Finland

Dr. Max Döbeli
Labor für Ionenstrahlphysik
ETH Zürich
Zürich, Switzerland

Opponent

Dr. Ian Vickridge
Institut des NanoSciences de Paris (INSP)
Université Pierre et Marie Curie
Paris, France

TIIVISTELMÄ (ABSTRACT IN FINNISH)

Lentoaika-ERDA on ionisuihkupohjainen materiaalianalyysimenetelmä, jonka avulla voidaan ohutkalvonäytteen alkuainepitoisuuksia määrittää eri syvyyksiltä pinnan läheltä. Menetelmällä voidaan määrittää samanaikaisesti kevyiden alkuaineiden, ml. vedyn, ja raskaampien aineiden pitoisuuksia.

Menetelmän massaerotuskyvyn parantamiseksi ja kinemaattisen korjauksen mahdollistamiseksi tässä työssä rakennettiin paikkaherkkä kaasun ionisaatioon perustuva energiailmaisin lentoaika-ERDA-laitteiston osaksi. Tämä ilmaisin ja aiemmin rakennetut lentoaikaportit kytkettiin moderniin täysin digitoivaan datankeruuseen.

Tässä väitöskirjassa kuvataan näiden laitteiden suunnitteluun vaikuttavia asioita, kaasuionisaatiokammion mekaanisesta suunnittelusta datankeruujärjestelmän algoritmi- ja ohjelmistokehitykseen. Kehitetyn laitteiston suorituskykyä tutkittiin mittausten ja Monte Carlo -tietokonesimulaatiomenetelmien avulla. Väitöskirjassa esitetään uusia menetelmiä datankeruujärjestelmään ja ilmaisimiin liittyvien ilmiöiden mallintamiseksi ja näitä menetelmiä käytetään uuden laitteistokonseptin suunnittelussa.

PREFACE

The work presented in this thesis has been carried out at the Accelerator laboratory of the Department of Physics, University of Jyväskylä, during the years 2011–2016. I want to thank my supervisor Prof. Timo Sajavaara for introducing me to the world of ion beam analysis already back in 2008 and for guidance over the years.

In addition to my supervisor I wish to thank my other close collaborators, Dr. Mikko Laitinen, whose work on time-of-flight ERDA made it possible for me to continue on the subject and Dr. Kai Arstila for his work on MCERD and for helpful discussions on the simulations. The electrical and mechanical workshop staff must also be thanked.

The past and present members of the Accelerator Based Materials Science group at the Accelerator Laboratory all deserve thanks, especially Ms. Mari Napari for enduring me for five years in a small shared office.

Special thanks are extended to my friends and Dr. Ville Toivanen in particular for continuing friendship since the beginning of our university studies both at work and on our time off.

I would like to thank my parents Jorma and Eija and my sister Essi for supporting me and always encouraging me to study.

The work presented in this thesis was supported by the Finnish Funding Agency for Technology and Innovation Tekes through EU regional funds project HIU-DAKE and Academy of Finland Center of Excellence in Nuclear and Accelerator Based Physics (Ref. 251353).

Jyväskylä, September 2016,

Jaakko Julin

ACRONYMS AND NOMENCLATURE

ADC	Analog-to-digital converter
ALD	Atomic layer deposition
ARC	Amplitude and rise time compensated (timing)
CFD	Constant fraction discriminator
CPU	Central processing unit (of a computer)
CSP	Charge sensitive preamplifier
CVD	Chemical vapor deposition
DES	Dual edge sampling
DPP	Digital pulse processing
ENOB	Effective number of bits
ERDA	Elastic recoil detection analysis
FET	Field effect transistor
FIFO	First in, first out (queue)
FPGA	Field-programmable gate array
FWHM	Full width at half maximum
GIC	Gas ionization chamber
GUI	Graphical user interface
HI	Heavy ion
IBA	Ion beam analysis
LSB	Least significant bit
MCA	Multichannel analyzer
MCP	Microchannel plate
MC	Monte Carlo (simulation)
PC	Personal computer
PEEK	Polyether ether ketone, an engineering thermoplastic
PHA	Pulse height analysis
POM	Polyoxymethylene, an engineering thermoplastic
POSIX	Portable operating system interface
RBS	Rutherford backscattering spectrometry
RMS	Root mean square
SSD	Solid state detector
TAC	Time-to-amplitude converter
TDC	Time-to-digital converter
TFA	Timing filter amplifier
TOF	Time-of-flight

LIST OF INCLUDED ARTICLES

PI Jaakko Julin, Mikko Laitinen, Timo Sajavaara. Time-of-flight ERD with a 200 mm^2 Si_3N_4 window gas ionization chamber energy detector. *Nuclear Instruments and Methods in Physics Research Section B: Beam Interactions with Materials and Atoms 332 (2014) 271–274*.

PII Jaakko Julin, Timo Sajavaara. Digitizing data acquisition and time-of-flight pulse processing for ToF-ERDA. *Nuclear Instruments and Methods in Physics Research Section B: Beam Interactions with Materials and Atoms 366 (2016) 179–183*.

PIII Jaakko Julin, Kai Arstila, Timo Sajavaara. Simulations on time-of-flight ERDA spectrometer performance. *Review of Scientific Instruments 87 (2016) 083309*.

PIV Jaakko Julin, Timo Sajavaara. Conceptual study of a heavy-ion-ERDA spectrometer for energies below 6 MeV. *Submitted to Nuclear Instruments and Methods in Physics Research Section B: Beam Interactions with Materials and Atoms*.

The author of this thesis did all of the development work, experiments and data analysis in articles PI, PII, PIII and some of the experiments and data analysis in PIV. The author performed all simulations in PIII and PIV. The author wrote the manuscripts of all the papers.

CONTENTS

1 INTRODUCTION

Time-of-flight elastic recoil detection analysis (ToF-ERDA) is a material analysis method developed in the early 1980s [1, 2] as a refinement of the more conventional ERDA method, first demonstrated by L'Ecuyer et al. [3, 4] in the 1970s.

The analysis provides elemental depth profiles, i.e. the concentration of an element in a sample as function of depth. The method usually does not have lateral resolution and is therefore mostly used in the analysis of featureless (1D) thin films ranging in thickness from 1 nm to 1 µm. The depth resolution at the surface can be as good as one atomic layer [5].

ERDA, like the more well known Rutherford backscattering spectrometry (RBS), is categorized as an ion beam analysis (IBA) method. RBS, ERDA and other IBA methods are usually described as sensitive, non-destructive and quantitative, although these properties are often somewhat exaggerated. The quantification relies on the knowledge of fundamental scattering cross sections and the energy loss of ions in matter.

The experimental setup requires an accelerator providing a heavy ion beam, anything from helium to gold ions with energies in the MeV range. At the end of a beamline there is an experimental station consisting of a high vacuum system with a sample holder, which holds the sample tilted away from the beam in a well known angle. As the heavy ions hit the atoms in the sample these atoms can be recoiled out of the sample. These recoils are detected in a spectrometer located at a forward angle typically of 25° to 45° relative to the incoming beam. The other alternative for thin targets is to use transmission geometry [3]. Conventional ERDA is used to depth profile only the lightest elements, nowadays typically only hydrogen. Mylar absorber foils are used to stop other recoils than hydrogen before the energy measurement with a silicon detector.

A ToF-ERDA spectrometer usually consists of two timing detectors and an energy detector. The timing detectors are used to measure the time-of-flight over a fixed distance. With the help of the energy detector different masses can be separated. A recoil originating from deeper in the sample will have less energy, or correspondingly longer time-of-flight, than a recoil from the surface as both the incident ion and the recoil will have lost some energy upon traversing the sample. There are other means to determine the energy and mass of the recoils, for example Bragg chambers, $\Delta E - E$ telescopes and magnetic spectrometers, all of which have been or are used successfully.

Time-of-flight telescopes have the advantage over other spectrometers of being able to detect all elements present in the sample simultaneously with better mass resolution than $\Delta E - E$ telescopes. The species-independent time-of-flight calibration simplifies the analysis significantly.

Thin films suitable for ToF-ERDA analysis are used in fabrication of microelectronics, batteries and in industrial applications as protective or friction reducing coatings. In the past decade many ToF-ERDA spectrometers have been built [6–10] suggesting the importance of light element analysis in thin film research and development and the suitability of the method to this task. The popularity of the method has been historically limited by unavailability of commercial instrumentation and the need for a large heavy ion accelerator, i.e. an electrostatic accelerator with a >4 MV terminal voltage.

Better depth resolution and sensitivity can be achieved at lower energies. By improving the mass resolving power of the instrument a smaller <2 MV accelerator becomes feasible. The reduction in probing depth, the maximum depth from which information is obtained is not necessarily a limitation when <100 nm films are studied. In order to make ToF-ERDA even more attractive the instrumentation should be optimized for lower energies and made more accessible to the scientific community.

In this thesis means to improve the instrumentation are introduced. In order to improve the mass resolution and depth resolution at the surface a position sensitive gas ionization chamber with a thin entrance window was developed. The data acquisition was modernized by implementing a system which uses waveform digitizers and a combination of FPGA and software algorithms for pulse processing. The system is also used as a diagnostic tool to facilitate further development of instrumentation. Finally the performance of the entire system with the data acquisition setup and the energy detector are simulated in order to understand the count-rate and position sensitive effects of the newly developed system.

2 ION-MATTER INTERACTION

As ion matter interaction is an extensive topic the reader is referred to more complete reviews on the topic such as Ref. [11]. Only the more relevant effects for heavy ion elastic recoil detection and gas ionization chambers are briefly discussed here.

2.1 Elastic scattering

The elastic scattering of charged particles from the Coulomb potential of an atomic nucleus is known as Rutherford scattering, after Lord Ernest Rutherford. Under the supervision of Rutherford Hans Geiger and Ernest Marsden performed experiments in which alpha particles were scattered from thin metal foils. These experiments and theoretical work allowed Rutherford to argue "it seems simplest to suppose that the atom contains a central charge distributed through a very small volume, and that the large single deflexions are due to the central charge as a whole, and not to its constituents" [12]. The first part of this claim is the starting point of nuclear physics as we know it today. The latter is a key observation for scattering of nuclei to be used as an analytical technique in material science.

In an elastic collision both energy and momentum are conserved. The laboratory energy E_1 of a particle with mass m_1 scattering from a target atom with mass m_2,

see Fig. 1, is given by [13]

$$\frac{E_1}{E} = 1 - \frac{2m_1m_2}{(m_1+m_2)^2}(1-\cos\theta) \tag{1}$$

$$= \frac{m_1^2}{(m_1+m_2)^2}\left(\cos\theta' \pm \sqrt{\left(\frac{m_2}{m_1}\right)^2 - \sin^2\theta'}\right)^2, \tag{2}$$

where E is the initial energy, θ is the center of mass scattering angle and m_2 the target atom mass.

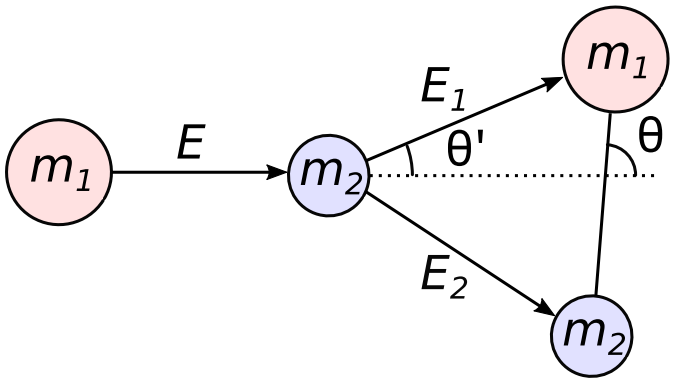

FIGURE 1 Schematic of forward scattering of particle with mass m_1 and energy E from a stationary target atom, mass m_2. The center of mass scattering angle is θ.

The differential Rutherford scattering cross section, i.e. the intrinsic rate of scattering events to a given angle per unit time per unit solid angle divided by the flux, is usually given as [14]

$$\frac{d\sigma_R}{d\Omega} = \left(\frac{Z_1Z_2e^2}{16\pi\epsilon_0E}\right)^2 \mathrm{cosec}^4\left(\frac{\theta}{2}\right), \tag{3}$$

where θ is the scattering angle in center of mass coordinate system, E is the energy of the incident ion. Z_1 and Z_2 are the atomic numbers of the incident ion and the target atom, respectively.

Deviations from Rutherford cross sections exist at high energies, however for the purposes of this work they have little consequence.

Low energy deviations are of much greater importance. Cross-sections deviate from Rutherford formula due to screening of nuclear charges by the electrons of both the projectile and the target. Energy dependent first order correction for backscattering angles was given by L'Ecuyer et al. [15] as

$$\sigma(\theta) = \sigma_R(\theta)\left(1 - \frac{(0.049\,\mathrm{keV})Z_1Z_2^{\frac{4}{3}}}{E}\right). \tag{4}$$

More accurate energy and scattering angle dependent correction by Andersen et al. [16] should be used instead of Eq. 4 at low energies and for small angle collisions e.g. in low energy ERDA.

2.2 Stopping

The energy loss due to excitation and ionization of target particles is usually called electronic stopping, while the transfer of energy to the center-of-mass motion of target atoms is called nuclear stopping [11]. Additionally changes in the internal state of the projectile or emission of radiation can affect the velocity of a projectile [11].

The average loss of energy per unit distance is called the stopping force[1], which is a property of the stopping medium for a given projectile. Often the radiative processes are ignored and the total stopping can be written as a sum of electronic and nuclear stopping

$$S(E) = -\frac{dE}{dx} = -\left(\frac{dE}{dx}_{\mathrm{e}} + \frac{dE}{dx}_{\mathrm{n}}\right). \tag{5}$$

The minus sign makes the quantity positive. The primary contribution for stopping at higher energies is the electronic stopping.

There is no single theory to give a complete picture of stopping of different ions in matter from first principles. Most theories rely on experimental scaling and corrections. The experimentalists quite often prefer to use values given by SRIM [17], which are combinations of fits to theory and interpolation of measured experimental data.

In Fig. 2 the stopping force of silicon for alpha particles (^{4}He) is plotted, with data from SRIM 2013.

The electronic stopping force in the velocity range $\approx 0.1 v_0$ to $Z_1^{2/3} v_0$ is approximately proportional to velocity [18], where v_0 is the Bohr velocity $e^2/\hbar \approx c/137$, i.e. the orbital speed of an electron in the ground state of a hydrogen atom [11]. At higher energies $v \gg v_0$ the ion will become fully stripped and the theory of Bethe formula predicts decrease as v^{-2}, until relativistic effects start to play a role.

The electronic structure of the matter is important. Stopping in compounds is usually estimated using Bragg rule [19], which simply assumes the stopping of compounds to be linear combination of the constituent elements. This estimation

[1] Stopping force has been and still sometimes is called the stopping power, even though the quantity clearly has the unit of force.

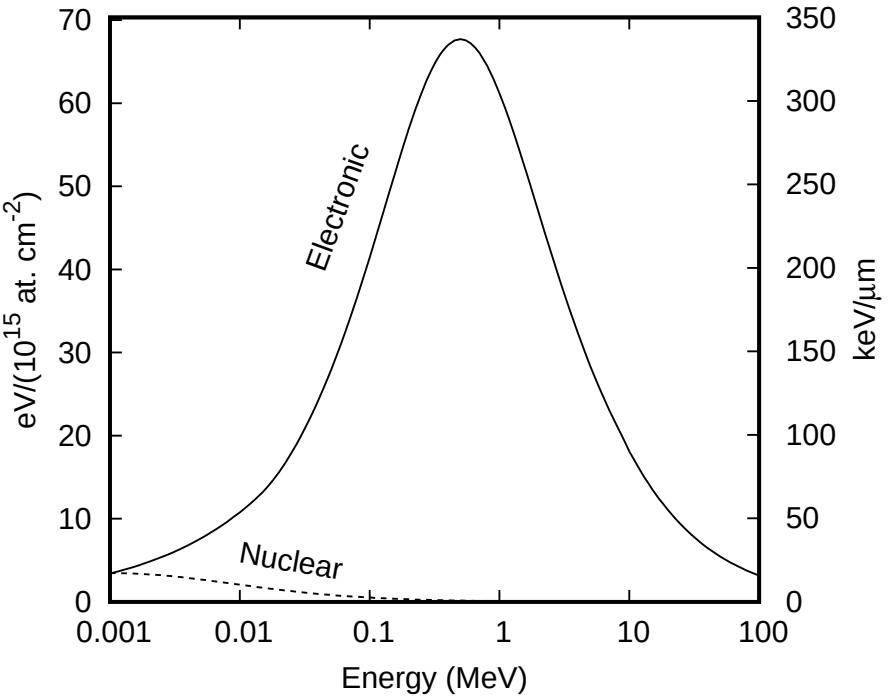

FIGURE 2 The electronic and nuclear stopping forces of silicon for ^{4}He. The data is from SRIM. The electronic stopping has a pronounced maximum and the nuclear stopping contribution is only significant at low energies.

is shown not to be valid for example in hydrocarbons, where the more accurate estimations can be made by taking into account the number of different C-H and C-C bonds [20]. This kind of core and bond (CAB) approach is used by SRIM for some compounds to make corrections to Bragg rule [17]. The inaccuracy of Bragg rule and discrepancies between heavy ion stopping measurements are evident in Fig. 3, since in these measurements [21] stopping in the same silicon nitride membrane, with a composition of $Si_3N_{3.57}H_{0.13}C_{0.02}O_{0.08}$ was measured and compared to stopping values obtained from SRIM and MSTAR, which both use the Bragg rule to calculate the stopping from elemental values without corrections.

Nuclear stopping is the energy lost by projectile to the collisions between the nuclei of the matter, which at high energies is essentially Rutherford scattering. This implies that the probability of scattering from nuclei is low at high energies, but individual collisions may transfer significant amount of energy to target nuclei.

The stopping described above is based on averages. The actual stopping process is a statistical process and subject to certain fluctuation around the average, called energy straggling. According to a simple model developed by Bohr, the variance of initially monoenergetic ion, atomic number Z_1 after passing through matter, atomic number Z_2 with thickness x and N atoms per volume is [11]

$$\Omega^2_{\text{Bohr}} = 4\pi Z_1^2 Z_2 e^4 N x. \tag{6}$$

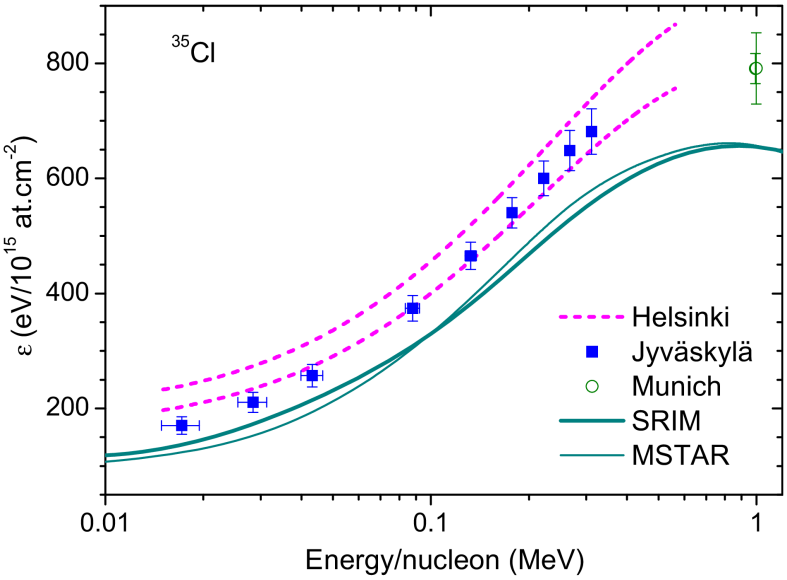

FIGURE 3 Stopping cross section of silicon nitride for ^{35}Cl. Reprinted from Ref. [21], with permission from Elsevier.

This theory has been improved, notably by Chu [22], who took into account the Z_2 structure of straggling at low energies, by calculating the charge distribution for the target atom using a Hartree-Fock-Slater model. Empirical fits were made by Yang et al. [23] based on Chu's calculations, which take into account the effective charge state of the incident ion. These values are used often when heavy ion straggling needs to be calculated.

2.3 Ionization

A fast particle traversing through a gas or liquid will ionize the molecules, creating electrons and singly or multiply charged positive ions. The mean energy expended in a specific gas per ion pair formed, W is defined as [24]

$$W = \frac{E}{N}, \tag{7}$$

where E is the initial kinetic energy of a charged particle and N is the mean number of electron-ion pairs formed when this energy is completely dissipated in the gas. The total electron charge created is $Q = Ne$, where e is the charge of the electron.

The liberated electrons may recombine with a positive ion or in some gases attach to a neutral molecule, forming negative ions [25].

All the various mechanisms producing ionization must be accounted for. Sec-

ondary ionization occurs by fast electrons, or delta-rays, and recoiling gas molecules and ions. Some of the energy is dissipated by non-ionizing mechanisms, for example excitations of the target atoms can lead to non-ionizing photons to be emitted.

The quantity W is sometimes mistaken to be a constant – an approximation which holds relatively well when the incident particle is much faster than the valence electrons of the molecules of gas. W has been observed to be species and energy dependent [24, 26, 27]. Different ions have different energy varying cross-sections for ionization and excitation and there is transfer of kinetic energy to gas molecules through recoil cascades [24, 28].

It should be noted that the W in semiconductors is noticeably smaller than in gases.

3 TIME-OF-FLIGHT ERDA

In order to understand time-of-flight ERDA as an analytical technique it is not enough to understand fundamental physics of ion-matter interaction but it is also necessary to appreciate the capabilities and limitations of the instruments and analysis tools that are used to perform the measurements and extract quantitative information on sample composition from the collected data.

3.1 Accelerators and ion beams

Time-of-flight ERDA requires a monoenergetic 1 MeV to 100 MeV heavy ion beam, typically of some nanoamperes with a beam spot of a few mm^2. There are several possible accelerator systems that can be used, the most usual combination is a sputtering ion source capable of producing negative ions from a solid target and an electrostatic tandem accelerator. Due to the high voltages these electrostatic accelerators are always housed in vessels filled with high pressure insulating gas, such as CO_2 or SF_6.

A caesium sputtering ion source is capable of providing a variety of negative ions from solid targets, some of the more useful ones in time-of-flight ERDA are $^{35}Cl^-$, $^{63}Cu^-$, $^{127}I^-$ and $^{197}Au^-$. These negative ions are accelerated with a typical 2 MV to 6 MV terminal voltage, some electrons are stripped with a gas or carbon foil stripper inside the high voltage terminal. The resulting positive ions with a charge state from 1+ to 10+ or even higher are then further accelerated with the same positive terminal voltage, which now repels the positive ions. A dipole magnet is used to analyze the beam, in order to choose the ion with the correct mass to charge ratio, and to select a beamline. Focusing and steering elements, either electrostatic or magnetic, and collimators are usually necessary to fine tune

the beam to the target and to define a beam spot.

In this work the 1.7 MV Pelletron 5SDH-2 accelerator of the Accelerator Laboratory of the Department of Physics at the University of Jyväskylä was used. The time-of-flight ERDA telescope is installed into a spherical near-UHV vacuum chamber at the 15° beamline. The chamber is equipped with a six axis goniometer and a load lock. The base pressure during measurements is maintained at the 1×10^{-7} mbar level by a turbomolecular pump at the base of the chamber and other pumps in the beamline. The most often used beams with ToF-ERDA with this setup are 8.5 MeV $^{35}Cl^{4+}$ and 13.6 MeV $^{63}Cu^{7+}$.

3.2 Kinematics and depth profiling

When an incident ion, mass m_1, energy E_0 causes a target atom, mass m_2 to be elastically recoiled to an angle of θ respective to the direction of the incident particle the energy of the recoil post-collision in the laboratory frame of reference is

$$E_2 = \frac{4m_1m_2}{(m_1+m_2)^2} cos^2\theta E_0. \tag{8}$$

This equation can be used to calculate the energies of different recoils at the sample surface. Some of the recoil energies with beams used in Jyväskylä are tabulated in Table 1. The time-of-flight of the recoil between two detectors placed a distance of L apart is given by the non-relativistic formula

$$t = \frac{L}{v} = L\sqrt{\frac{m_2}{2E_2}}. \tag{9}$$

TABLE 1 Energy (in keV) of various recoils ejected from the surface towards the detectors ($\theta = 41.3°$) with typical beams used in ToF-ERDA in Jyväskylä.

Incident ion	E_0	^{1}H	^{12}C	^{28}Si	^{48}Ti	^{64}Zn
$^{79}Br^{7+}$	13 600	382	3518	5933	7218	7591
$^{63}Cu^{7+}$	13 600	476	4130	6541	7536	7675
$^{35}Cl^{4+}$	8 500	523	3650	4738	4680	4386
$^{35}Cl^{2+}$	5 100	314	2190	2843	2808	2632

Due to the measurement geometry the sample is tilted in respect to both the beam and the detectors. A layer of matter, thickness d appears thicker to the ion beam due to the tilt. The effective thickness can be calculated as

$$d' = \frac{d}{\sin\alpha}, \tag{10}$$

where α is the angle between the direction of the beam and the sample surface. The effective thickness for the recoils need not be the same as for the incident ions. The effective thicknesses are equal when mirror geometry is used, i.e. the angle between sample surface and detectors β is equal to α, see Fig. 4.

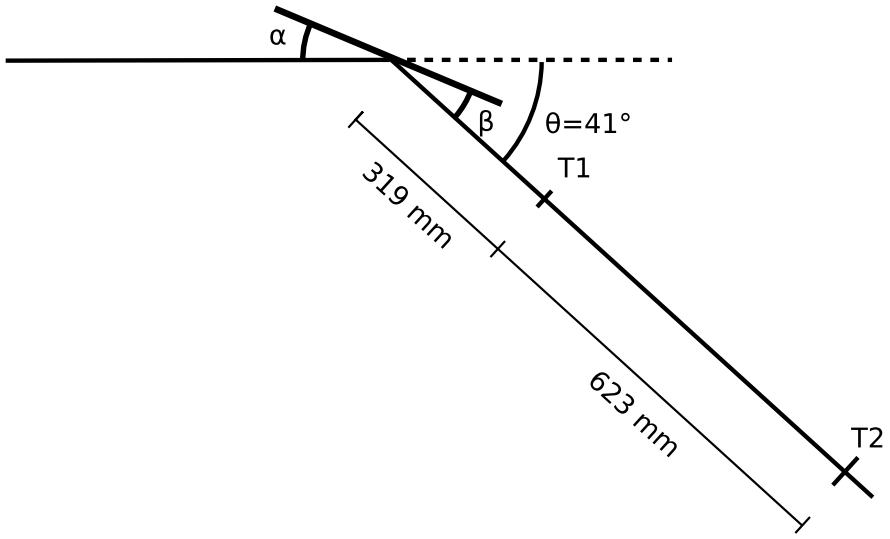

FIGURE 4 A typical time-of-flight ERD geometry. The dimensions correspond to the Jyväskylä setup.

When the recoil is ejected beneath the surface of the sample both the energy lost by the incident ion and the subsequent recoil must be taken into account. Stopping is discussed in Section 2.2. The mean energy [1] of an ion recoiling from depth d (effective depth d' for the incident ion and d'' for the recoil) can be written as

$$E = \frac{4m_1m_2}{(m_1+m_2)^2}cos^2\theta\left(E_0 - \int_0^{d'} S(E,x)dx\right) - \int_{d''}^{0} S'(E,x')dx' \qquad (11)$$

where $S(E(x),x)$ and $S'(E(x'),x')$ are the stopping forces along the path of the incident and recoil ions, respectively. The energy loss in the sample forms the basis for depth profiling. The experimentalist can affect the depth resolution by choosing the incident ion species, energy and sample tilt. The time-of-flight spectra of various recoils can and usually does overlap. Measuring time-of-flight (velocity) and energy in coincidence will allow different masses to be separated, allowing the identification of mass and energy unambiguously.

Many of the so-called energy detectors actually measure ionization, and as such have a non-linear mass-dependent energy calibration. The time-of-flight measurement usually offers better energy resolution once the mass has been identified.

[1] Effects such as plural scattering are ignored for the sake of clarity.

In Fig. 5 two nearly identical time-of-flight–energy histograms are plotted. The samples were grown by atomic layer deposition (ALD) using $TiCl_4$ and water at 110 °C. The sample in Fig. 5(b) was annealed at 300 °C. All elements present in the samples (H, C, O, Si, Cl, Ti) can be detected. The time-of-flight range of interest is approximately 50 ns to 200 ns.

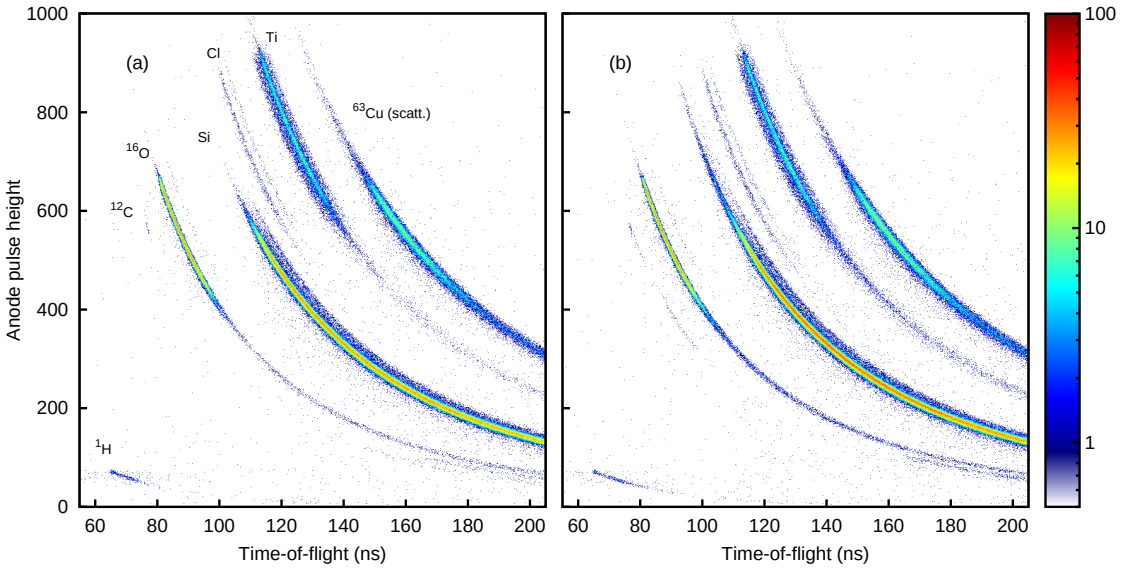

FIGURE 5 Two time-of-flight–energy histograms of 100 nm TiO_2 samples on silicon substrate. The sample in (b) was annealed at 300 °C. The samples were measured with 13.6 MeV ^{63}Cu beam in mirror geometry. The vertical axis is the anode pulse height from a gas ionization chamber, which is proportional to the energy deposited in the detector. The horizontal axis is the time-of-flight between the timing detectors, placed 623 mm apart. The distribution of some elements can be seen qualitatively from these histograms, for example in (a) there is trace amount of carbon at the surface of the film

Eq. 8 is often used with an assumption that the θ angle is characteristic for the given setup. However finite solid angle Ω of any realistic detector and finite beam spot size will cause θ to be slightly different in each collision. The variation in E_2 for the same E_0 due to variations in θ is known as *kinematic broadening*. Increasing the accuracy of E_2 measurement beyond some point does not improve the depth resolution unless θ can be measured. Spectrometers with large Ω should be position sensitive at least in the scattering plane.

3.3 Detectors and data acquisition

Time-of-flight of a recoiling particle in a two timing detector ToF-ERDA spectrometer is the time difference between a pulse from the T1 detector and the T2 detector, which are induced by the passage of the recoil through the timing detectors. A typical analog electronics chain consists of a time-to-amplitude converter (TAC) which uses the T1 signal as a start and T2 signal as a stop and creates an output pulse with an amplitude proportional to the time difference. The start signal can also be used from T2, in which case the T1 signal is delayed and used as the stop.

The energy detector signals, after preamplification, are filtered with a shaping amplifier. The time-of-flight and energy information are digitized using conventional peak-sensing ADCs and a multiparameter data acquisition setup. Collection of data in list mode is advantageous, since the measured samples can be damaged by ion bombardment during the measurement and only an initial part of the measurement can be used in the analysis. A more advanced data acquisition setup timestamps the energy and time-of-flight ADC events and allows the coincidence criteria set post measurement, which usually results in reduced background since the coincidence window can be set more accurately.

An alternative to the conventional electronics chain is to directly digitize the detector signal after the preamplifier. The shaping amplifiers and discriminators are replaced by programmable logic or software algorithms.

3.4 Analysis of data

The results of an ERD analysis are elemental concentration depth profiles. In IBA many pieces of software have been created to serve the analysis needs of the community. Some, like DataFurnace [29] are automatic fitting codes operating on experimental spectra while others like SimNRA [30] simulate energy spectra analytically.

In time-of-flight ERD analysis when elements can be unambiguously identified it is also possible to extract depth profiles from measured data by an iterative procedure where the sample is first assumed to be homogenous and then the yield of every element is corrected with scattering cross sections associated with the detected events, for which the depth of origin can also be calculated using known stopping values. The process can be repeated using the new guess and after a few iterations the depth profiles will converge. This approach is used by Allegria [31] and Potku [32].

Multiple and plural scattering are not taken into account in these backwards calculating codes and the codes based on analytical formulas do not model them perfectly. The experimental data can also be compared with Monte Carlo simulations, for example using MCERD [33] or CORTEO [34]. These tools are however rather time consuming and usually not preferred for routine analysis.

Examples of depth profiles extracted from the same measurements as histograms presented in Fig. 5 are plotted in Fig. 6. The differences between the samples are explained when scanning electron micrographs in Fig. 7 are studied. The film annealed at 300 °C had cracked during this process and the ERD analysis of the sample in 6(b) is not valid, as the film does not cover the substrate evenly. One needs to be careful when drawing conclusions from depth profiles alone, as effects like these can be misinterpreted as mixing of layers or diffusion.

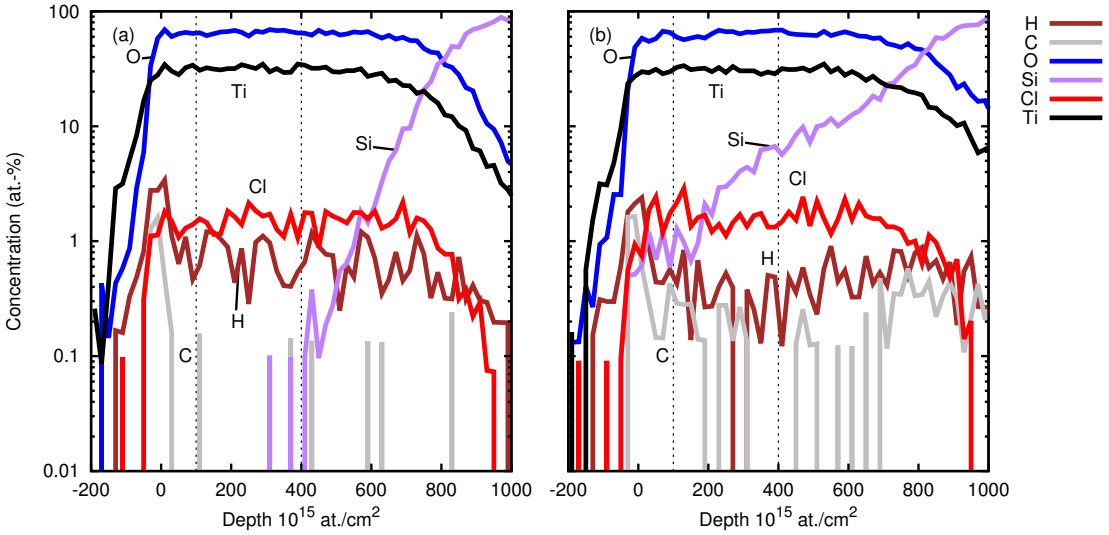

FIGURE 6 Depth profiles of the two samples. The measurements correspond to histograms presented in Fig. 5. In addition to Ti and O there are some Cl and H impurities remaining from the precursors in the film. Additionally there is some C at the surface. In (b) there is seemingly some Si in the film, the presence of which is explained in the text.

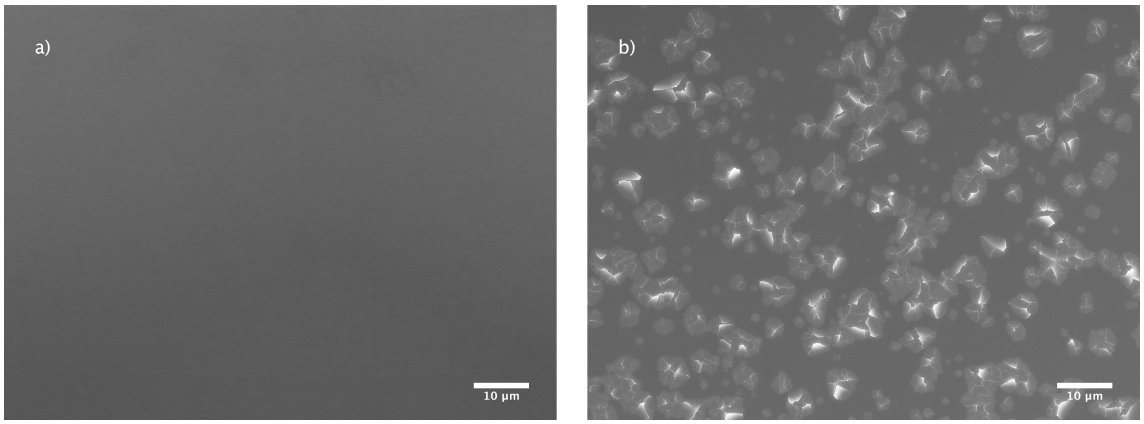

FIGURE 7 Scanning electron microscope images of the two TiO_2 samples, courtesy of Dr. Kai Arstila. In (a) the film is as deposited and in (b) post anneal. The film in (b) has cracked during the annealing process.

4 GAS IONIZATION CHAMBER

Gaseous particle detectors are based on direct electronic detection of the ionization resulting from a passage of a particle. Detectors based on supersaturated vapor (cloud chamber), superheated liquid (bubble chamber) or optical detection of avalanches (streamer chambers) are therefore not treated here. Since the first detectors were used already in the early 1900s many designs have reached maturity and even obsolescence.

A simple chamber for ion beam applications is the DC chamber, which detects the total current resulting from ionization by a flux of particles. An electric field is applied in a volume of gas with an external voltage. Both the liberated electrons and positive gas ions contribute to the charge collected from an electrode.

Most detectors however work in pulse mode, i.e. single particle pulses are detected. If the detector response is fast enough only the electron pulse contributes and slow moving ions can be neglected.

If high electric fields are used an electron drifting in the gas can achieve enough velocity so it can knock out another electron from a gas molecule. The resulting cascade of electrons is known as a Townsend discharge or a Townsend avalanche. In proportional counters, as the name suggests, the total signal will still be proportional to the number of primary electrons. Smaller amounts of primary ionization can be detected, which is useful for example in multi-wire proportional chambers (MWPC) used to detect the position of the particle. In this case the proportionality of signal is not of great concern.

Perhaps the most familiar of all gaseous detectors is the Geiger counter, which uses the Geiger-Müller tube to create a strong avalanche. The detector operates in the so-called saturation region i.e. the avalanche amplifies the original ionization so much that it no longer is proportional to the primary ionization. The signal can

be read out with a simple electronic circuitry, and therefore the Geiger counter has become an ubiquitous radiation survey and monitoring instrument.

The following sections will focus mainly on pulse mode gas ionization chambers with unity gain, i.e. no gas amplification, used to detect particles primarily in the 100 keV to 10 MeV range. Many factors affecting the operation and design of high energy particle detectors, X-ray detectors etc. are therefore omitted.

4.1 Physical foundations of gaseous detectors

4.1.1 Induced currents on electrodes

In ionization chambers electric fields are used to drive the electrons and ions created by incident radiation towards biased wires, plates or other surfaces. These moving charges induce currents on conductors, some of which can be sensing electrodes. The often used term "charge collection" should only be used when there is no misconception that currents on electrodes appear instantly when electrons are collected by electrodes.

The induction of currents by charges is better described as the change of electric flux through a given surface, as then by Gauss's law

$$\oint_S \vec{E} \cdot d\vec{a} = \frac{Q_{enc}}{\epsilon_0} \tag{12}$$

there is a corresponding change on the right hand side – induced charge.

A theory describing currents induced by moving charges was developed simultaneously by Shockley [35] and Ramo [36]. The theory is convenient when radiation detectors are studied [37]. In order to calculate currents induced on a conductor, all charges are removed and other conductors are grounded. Then the conductor under study is raised to unit potential. Now the resulting potentials and fields can be calculated and the instantaneous current induced by a moving electron is given simply as

$$i = E_v e v, \tag{13}$$

where v is the instantaneous velocity and E_v is the component of the electric field in the direction v. The same equation can be derived using the image charge method. When the theory is applied to many moving charges like in a gas ionization chamber space charge effects are neglected. The electric fields are assumed to propagate instantaneously.

The induced charge by a charge of q moving from $\vec{r}_0$ to $\vec{r}$ on a conductor can be

written as

$$\Delta Q = \int i \, dt = q \left[\varphi(\vec{r}) - \varphi(\vec{r}_0) \right], \tag{14}$$

where φ is the weighting potential, i.e. the electrostatic potential under the assumptions mentioned above. In the conductor $\varphi = 1$. If the charge moves from a region where $\varphi = 0$, for example from somewhere near another conductor, the total charge induced on the conductor of interest will be equal to q. The weighting potentials depend on the geometry of the conductors and dielectrics, not on the actual voltages present in the system.

The path the charges take can not be calculated from Eq. 14. The path depends on the actual applied voltages (local electric field) and therefore $Q(t)$ is better written as

$$\Delta Q(t) = \int_{t_0}^{t} i(t) \, dt = q \left[\varphi_A(\vec{r}(t)) - \varphi_A(\vec{r}(t_0)) \right], \tag{15}$$

where the path $\vec{r}(t)$ is determined by the drift of the charge carrier in the detector gas.

4.1.2 Drift and diffusion

The free electrons and ions in the gas are subject to random collisions due to thermal motion. The motion of electrons driven by the applied electric field is a collective drifting motion opposite to the direction pointed by the electric field vector[1]:

$$\frac{d\vec{x}}{dt} = -v_d(|E|)\hat{E}. \tag{16}$$

The average drift velocity v_d depends on the gas, the electric field strength and the pressure. The drift velocity is proportional to the electric field and inversely proportional to the collision cross section [38]. Since the gas atoms are essentially independent the drift velocity scales by the reduced electric field E/p, where p is the pressure. The drift velocity of electrons in isobutane is plotted in Fig. 8, which shows linear proportionality at low electric fields.

Using classical diffusion the transverse diffusion after a drift of x is given by [38, 40]

$$\sigma_x = \sqrt{\frac{2\epsilon_k}{eE} x}, \tag{17}$$

where ϵ_k is the characteristic energy of electrons at the field E. At low drift velocity this is primarily thermal motion and $\epsilon_k \approx 2kT$. The thermal motion gives the lower limit to diffusion, in practice the values are always higher and can be

[1] Positive charges drift to the direction of the electric field. Drift velocity v_d is usually given as a positive quantity even for electrons.

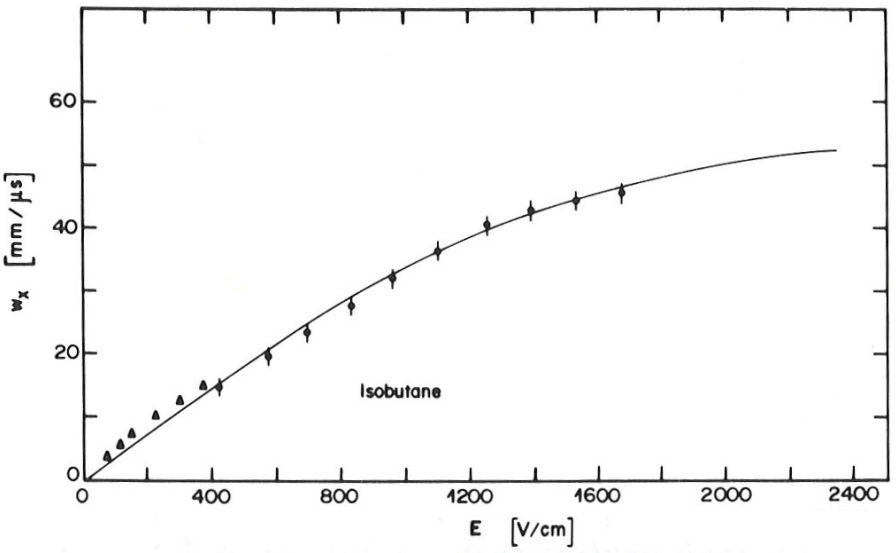

FIGURE 8 Drift velocity w_x in isobutane. Theoretical curve is compared with the experimental points measured at CERN or by the authors of Ref. [39] (▲) at 294 K and 760 mm of Hg. Reprinted from Ref. [40], with permission from Elsevier.

an order of magnitude different between gases. In Ref. [38] a numerical example is given, in argon $\langle v_d \rangle \approx 5\,\mathrm{cm\,\mu s^{-1}}$ and in 1 cm drift distance the diffusion is ≈ 1 mm while for carbon dioxide the diffusion is only $\approx 100\,\mu$m.

4.1.3 Fill gas

The choice of detector gas greatly depends on the intended use of the detector. Detection of X-rays and gammas favors large Z gases, such as Kr or Xe. For particle detectors scattering from heavy nuclei can be an issue, so light elements are preferred.

In a detector with a thin entrance window the detector gas pressure should be minimized while the stopping force is maximized, because the goal is to stop incident particles in the active volume. Following Bragg rule outlined in Section 2.2 the stopping of a compound is estimated by the linear combination of stopping forces of individual elements. When we write the ideal gas law as

$$\begin{aligned} pV &= nRT \\ p &= \frac{\rho}{M} RT, \end{aligned} \tag{18}$$

it follows that for a gas with the same elemental composition and the same mass density ρ, i.e. the same amount of constituent atoms and as a result same stopping force, the one with heavier molecules, i.e. larger M, will have lower pressure. Combination of light elements and heavy molecules makes hydrocarbons good candidates for the detector gas.

The intrinsic energy resolution of an ionization chamber is determined by the fluctuation in the number of electron-ion pairs

$$N = \frac{E}{W}. \tag{19}$$

See Sec. 2.3 for a discussion on W. If the formation of individual electron-ion pairs would be statistically independent process the fluctuation in the number of electron-ion pairs formed, N would obey Poisson statistics. However the observed variance is smaller, and a Fano factor F is introduced:

$$F = \frac{\sigma_{\text{observed}}}{\sigma_{\text{Poisson}}} = \frac{\sigma_{\text{observed}}}{N}. \tag{20}$$

The reason for this deviation from Poisson statistics is that electron-ion pairs are formed in many steps, each depositing a different amount of energy. There is however the constraint of energy conservation, which reduces the fluctuations and improves resolution [41, 42]. The Fano factor, like W, is energy and species dependent, and as a result the factor is often used semi-empirically. Gases with smaller Fano factors will yield better intrinsic energy resolution. The ionization yield of noble gases can be increased while the fluctuations in the yield can be reduced by adding even a small concentration ($\approx 0.5\%$) of some admixture, for example hydrocarbons [43]. This is due to the lower ionization potential of the admixture allowing the excited noble atoms to de-exite by ionization of the admixture molecules. These so called Penning-mixtures are quite often used in proportional counters, since they combine good energy resolution and convenience of achieving avalanche at lower fields [44]. The organic gas will quench avalanches by absorbing UV-photons, however the disassociation of polyatomic organic molecules necessitates operation under continuous flow of gas [44]. An often used low cost detector gas is the "P-10" – a mixture of 90% argon and 10% methane.

Electronegative gases, such as oxygen or water vapor are to be avoided, especially in ionization chambers. The electron capture will reduce pulse heights [44].

Faster drift velocity means faster pulses, which is advantageous at higher count rates or if good timing resolution is of interest.

In drift chambers the drift time of electrons is used to measure the position of ionization. If the drift velocity is not very sensitive to electric fields the position resolution of these chambers is improved, for example for isobutane filled detector according to Fig. 8 the drift velocity is relatively insensitive to the electric field when $E/p \gtrapprox \frac{1600\,\text{V/cm}}{760\,\text{mmHg}} \approx 1.6\,\text{V/cm/mbar}$. Also the diffusion discussed in previous section can limit the position resolution.

4.1.4 Frisch grid

Electron pulse chambers are inherently position sensitive, since the electrons will induce their charge only partially on any of the electrodes. This problem was solved by O. Frisch [45] by introducing a grid electrode in front of the anode. The Frisch grid shields the anode from the motion of the electrons until they pass through the grid [25]. The electrons will induce a full charge while passing between the grid and the anode. The ions drift in the opposite direction and never enter the volume between the grid and the anode.

There are two complications to this matter, namely the collection of electrons by the grid and the shielding inefficiency. The first problem can be mitigated by having a larger electric field between the grid and the anode than elsewhere in the detector volume, as then the electric field lines curve around the wires. This electron transparency was first studied by Bunemann et al. [46] and a recent paper suggests a procedure to characterize the transparency of mesh electrodes [47].

The shielding inefficiency has been solved analytically under certain approximations also by Bunemann and more recently improved numerical methods and Shockley-Ramo theorem have been applied in order to study the inefficiency with increased accuracy [48, 49].

4.2 Detector for ToF-ERDA

In time-of-flight ERDA the purpose of an energy detector is to complement the time-of-flight measurement by allowing mass separation. Light elements are usually easily separated even with the help of an energy detector with a modest energy resolution. Improvement in mass resolving power can be achieved by improving the energy resolution of the energy detection and in low-energy ERDA work the detector should also be able to detect low energy recoils. Since the resolution and minimum detectable energy are related quantities the detector should therefore have good resolution for all ion species at all energies.

The recoils can have a broad range of energies so also the range of the recoils in gas varies greatly. Low energy heavy recoils might have a range of only millimeters when the GIC pressure is just enough to stop the lightest recoils in the active gas volume.

However, according to Eq. 8 using heavier incident particles will reduce the momentum transfer to light target atoms compared to using a beam of lighter particles with the same energy. This has the interesting corollary that for example

TABLE 2 Energy, time-of-flight between the timing detectors (L=623 mm) and range in 20 mbar isobutane of various surface recoils with 13.6 MeV ^{63}Cu beam ($\theta = 41.3°$). Range data is from SRIM.

Recoil	E (keV)	ToF (ns)	Range (mm)
^{1}H	476	65	120
^{12}C	4130	76	98
^{28}Si	6541	93	89
^{48}Ti	7536	113	95
^{64}Zn	7675	129	90

when using 13.6 MeV ^{63}Cu beam the expected range of different surface recoils in isobutane is quite similar, see Table 2.

In addition to measuring the energy the detector can also be position sensitive. The simplest way of achieving position sensitivity is to place the electrodes perpendicular to the direction of intended position measurement, see Fig. 9. The position can be calculated either by comparing the amplitudes of the cathode and anode signals or by timing the drift of the electrons to the grid [50].

4.2.1 Mechanical and vacuum design

The vacuum chamber of the GIC was designed to be slightly larger than what was strictly necessary, to leave room for later changes in design. The construction is shown in cross-sectional view in Fig. 10.

The vacuum chamber and electrodes were made of stainless steel, except for the window frame which is made of aluminium, a choice motivated by the large number of frames manufactured and the necessary machining time. Vacuum compatible plastics were used for insulating parts, polyether ether ketone (PEEK) for finely machined parts and polyoxymethylene (POM, acetal) for others. Kapton (polyimide) film was used to insulate the edge of the electrodes from the entrance window frame.

The vacuum chamber is connected to the rest of the spectometer using a CF100 flange with a copper gasket. The rest of the flanges, one for the window frame, one for the top lid and KF16 and KF25 connections for gas handling and a vacuum gauge use FPM O-rings. The leak rate was tested with a Pfeiffer HLT 260 QualyTest helium leak detector to be less than 1×10^{-8} mbar L s^{-1}.

The isobutane bottle is connected through a regulator and a needle valve, al-

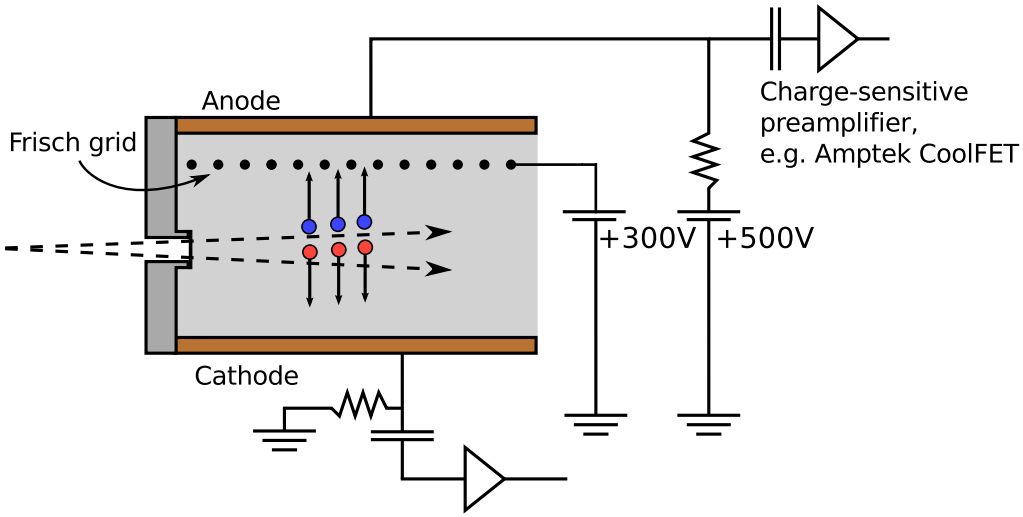

FIGURE 9 Schematic of the gas ionization chamber used as an ERDA energy detector. Recoils (dashed lines) enter the detector through a thin entrance window. The anode and cathode placement allows position sensitivity in the scattering plane. The electrons (blue circles) will drift to the anode through the Frisch grid, which shields the anode from the motion of electrons before they pass through the grid. Preamplifiers are AC-connected to the biased anode and cathode.

lowing the detector pressure to be set precisely. The gas (99.95% purity) is not circulated during the measurements, in fact the detector gas can be used for tens of hours of measurements over several days or even weeks. The possible degradation of resolution due to gas poisoning has not been confirmed. If the highest resolution is necessary the gas is replaced before measurements as a precautionary measure.

The pressure of the gas is measured with a Pfeiffer CMR 361 capacitive absolute pressure gauge. The accuracy of the gauge is 0.2% of reading and the full scale pressure is 1 bar.

4.2.2 Entrance window

Silicon nitride entrance windows have improved the resolution and particle identification in accelerator mass spectrometry (AMS) and IBA detectors [6, 52], where plastic windows were previously used. Silicon nitride is deposited on silicon using chemical vapor deposition (CVD) and etched chemically so that a frame around the opened nitride window remains. The primary advantages over polymer windows are lower energy loss, better thickness uniformity and gas tight-

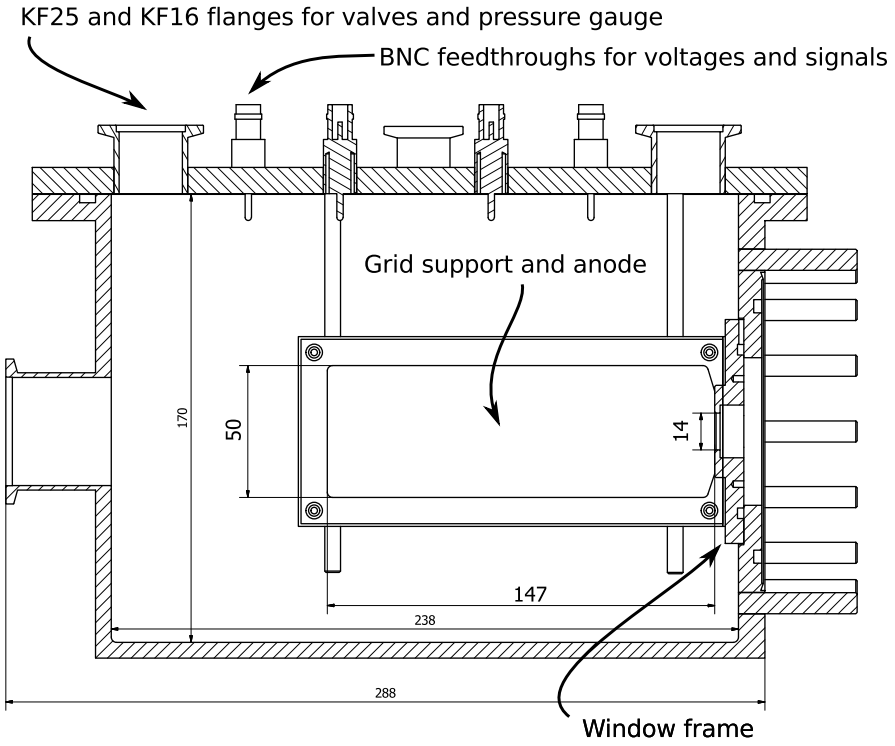

FIGURE 10 Cross-sectional view of the GIC. Reprinted from Ref. [51], PI, with permission from Elsevier.

ness. For the ERDA detector 100 nm thick windows were purchased from HS Foils Oy in various sizes.

While 20 mm by 20 mm window size was the original design goal, see Fig. 11, it was found that 25 mbar pressure difference was sufficient to burst a window of this size in tests. As the designed operating pressure was 20 mbar this size was deemed unsafe for regular use. A 14 mm by 14 mm window was found to withstand up to 40 mbar. The windows that have been used in the actual setup were always tested before installation by pressure cycling a test chamber with the window to 30 mbar overpressure several times to guarantee safe operation at a pressure up to 25 mbar.

4.2.3 Electrodes

The Frisch grid wires are gold plated tungsten with a diameter of 100 µm, purchased from Luma Metall Ab. The thickness of the coating is 0.5 µm according to the manufacturer. The coated tungsten wire is easy to weld on the 1 mm thick steel frame of the grid electrode.

A custom setup was used to weld the wires to the frame, where the wire pitch

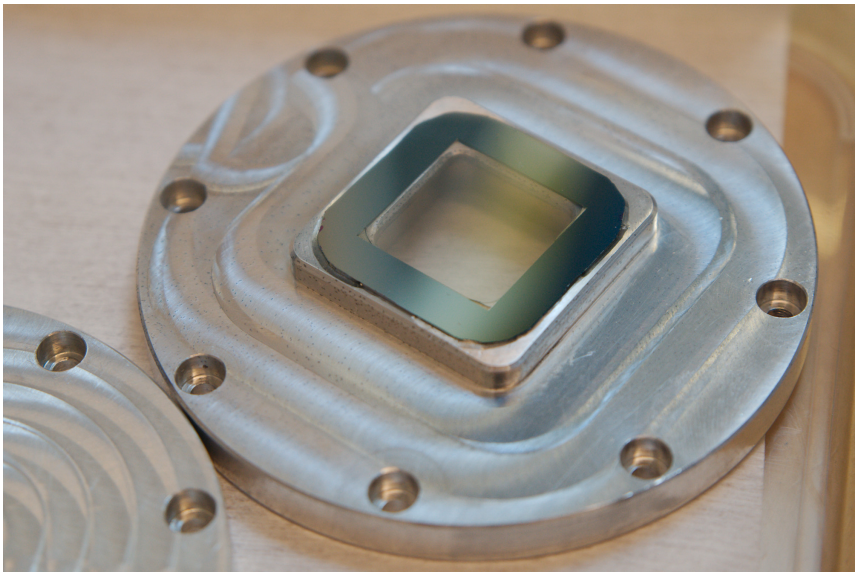

FIGURE 11 A photograph of a 100 nm thick silicon nitride entrance window on a silicon frame, which has been glued with epoxy to the aluminium window frame. The size of the window is approximately 20 mm by 20 mm.

is determined by placing the wire to the grooves of threaded rods. In order to achieve 1 mm pitch ISO metric M6 threaded rods were used. The rods remain stationary with the frame until the wires are welded. The wires should be tightened so that they remain under some tension, in order to reduce wire sag. The tension was set by using a fixed weight, resulting in approximately 1 N tension in each wire. Even though the frame is already mounted on the anode with the help of grid-anode spacer, see Fig. 12, the post-weld tension of the wires will be uneven. The mounting of the electrode allows the tension of the wires to be adjusted after welding by means of screws placed 15 mm apart on either side of the frame.

The BNC feedthroughs are nominally rated for 500 V, so the highest anode voltage used is 500 V. Grid voltage is typically 300 V and cathode is either grounded or biased to a negative voltage not more than -50 V. With these voltages the field in the grid – anode region is stronger than in grid – cathode drift region by more than a factor of two, ensuring good transmission of electrons through the grid. The field in the drift region is still more than enough to avoid recombination. Lowering the cathode voltage is not an option unless the window frame is biased, since at some point the potential of the near-window region will be lower than the potential of the detector walls and the window frame (0 V) and some electrons will drift to the walls instead of the anode.

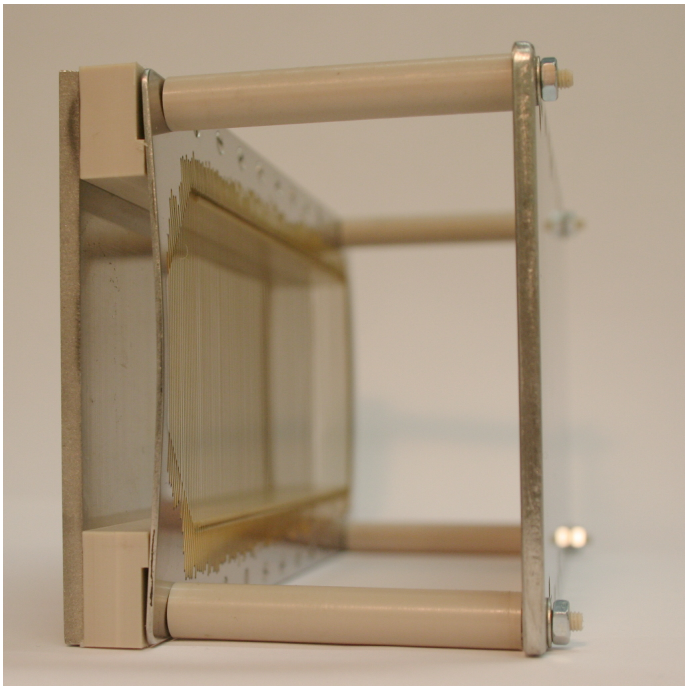

FIGURE 12 The electrodes of the GIC. The anode is the thick stainless steel plate on the left hand side of the figure, the grid electrode is separated from it by 9 mm tall PEEK plastic block. The cathode is separated from the grid by 50 mm. By adjusting the grid electrode screws it is possible to control the tension of the wires, this results in visible arching of the grid electrode.

4.2.4 Electronics and noise

Compared to a silicon detector the signal of a GIC is always weaker, due to the higher W value. Electronics noise limits the energy resolution for light elements and also sets the threshold for pulse detection.

Charge sensitive preamplifiers (CSP) are often used with detectors based on ionization. These amplifiers replaced voltage sensitive amplifiers, since CSPs are not sensitive to variations of detector capacitance [53]. For short pulses the charge sensitive preamplifier acts as a current integrator and the output rise time is ideally set by charge collection time. Typical pulses from the GIC, after amplification by charge sensitive preamplifiers are plotted in Fig. 13.

In this work Amptek CoolFET preamplifiers were used. The first field effect transistor of the operational amplifier stage is cooled by a Peltier cooler, which reduces the electronics noise. The electronic noise contribution was measured to be 26 keV for α-particles with the use of a known energy calibration and precision pulse generator. However almost similar resolution was achieved with more conventional preamplifiers.

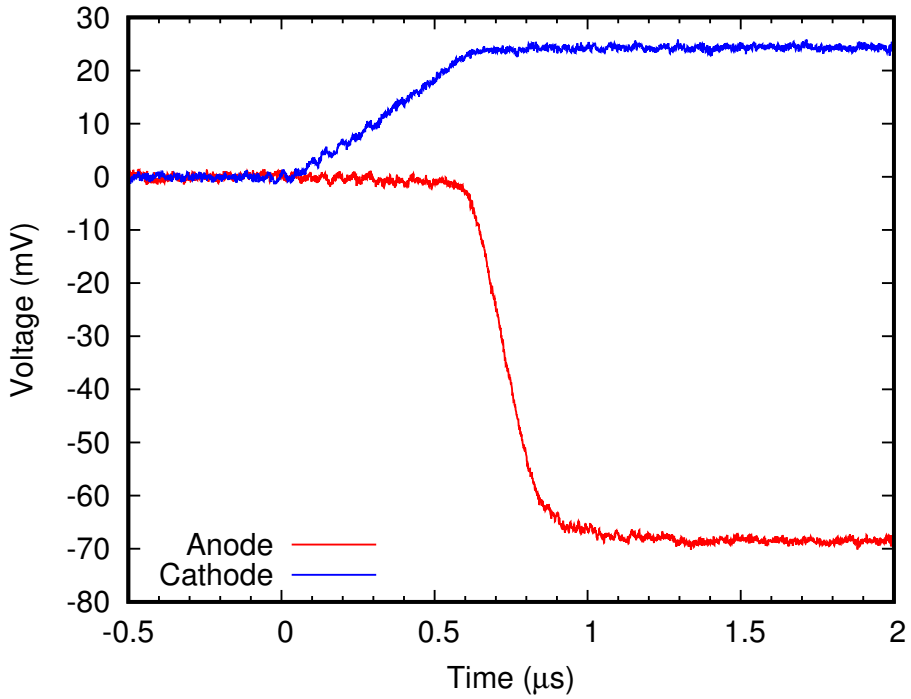

FIGURE 13 Typical anode and cathode oscilloscope traces from the GIC after preamplification by Amptek CoolFET preamplifiers. The original ionization was created by a few MeV recoil.

In addition to thermal noise in the amplification the signals can be affected by external electromagnetic pickup and vibrations. The large plates of the detector act as a rudimentary condenser microphone, creating electrical current from mechanical motion. The low frequency contributions are filtered out in a later signal processing stage. Some baseline fluctuations are plotted in Fig. 14.

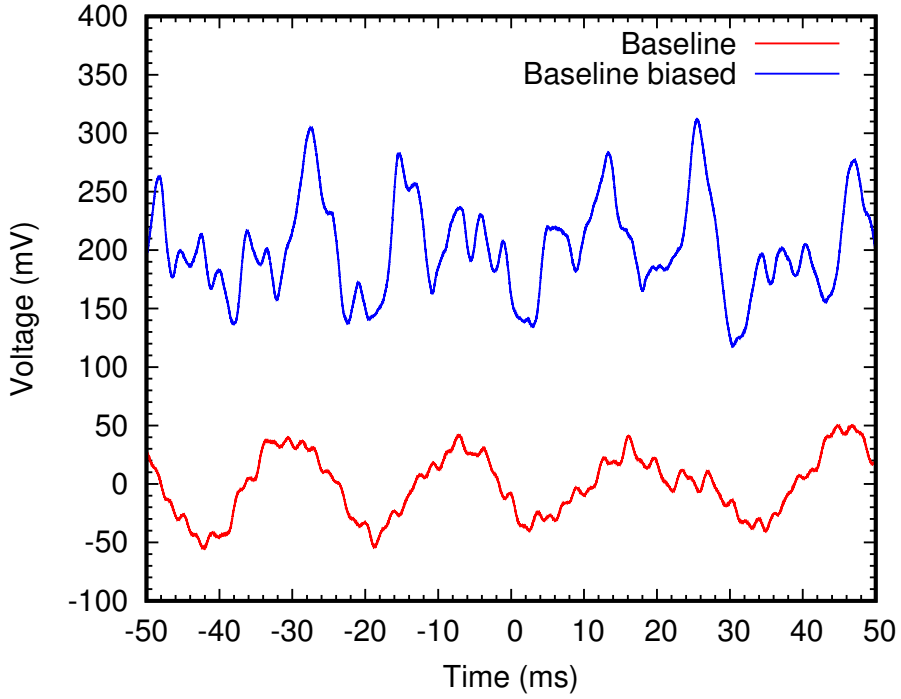

FIGURE 14 Oscilloscope traces from the anode after the preamplifier. There is a significant amount of low frequency noise present in the system. Some of it is attributed to 50 Hz and 100 Hz electrical noise, but also to vibrations. Especially the contribution of vibrations becomes larger as the detector is biased. The shift in preamplifier output DC-level is due to leakage current and charging of the bias voltage filter capacitors.

5 DIGITIZING DATA ACQUISITION AND PULSE PROCESSING

5.1 Waveform digitizers

An analog-to-digital converter (ADC) is an electronic device which (periodically) samples an analog signal and quantizes it. A waveform digitizer is a device which consists of a sufficiently fast analog-to-digital converter (ADC) to acquire an analog signal and means to process or transmit the quantized digital waveform or parts of it. A digitizer might also contain analog signal conditioning electronics before the ADC and digital signal processing (DSP) electronics.

The nominal voltage resolution is given in number of bits corresponding to a certain full scale voltage. The smallest unit of measurement, the least significant bit (LSB) is then the nominal resolution Q

$$Q = \frac{V_{\mathrm{FS}}}{2^{\mathrm{M}}}, \tag{21}$$

where V_{FS} is the full scale voltage and M number of bits. The sample rate F and sampling interval t_s are simply related by

$$F = \frac{1}{t_s}. \tag{22}$$

A more realistic figure for the vertical (voltage) resolution is often used than the number of bits. The effective number of bits (ENOB) of a digitizer is defined as [54]

$$\mathrm{ENOB} = N - \log_2\left(\frac{\mathrm{NAD}}{\epsilon_Q}\right), \tag{23}$$

where N is the number of digitized bits, NAD is the RMS noise and distortion

and $\epsilon_Q = \frac{Q}{\sqrt{12}}$ is the ideal RMS quantization error. The ENOB value is measured for a sine wave of some amplitude and frequency.

Waveform digitizers for nuclear instrumentation usually feature sample rates from 10^6 samples per second (1 MS/s) to several 10^9 samples per second (GS/s) and 8 to 16 bits of vertical resolution. The specifications vary depending on the intended use, the higher number of bits are common in high resolution pulse amplitude applications while faster digitizers are required for timing critical applications and capturing faster pulses or higher frequency signals.

A CAEN N6751 digitizer was used in this work. The 4 channel 1 GS/s 10-bit digitizer can also be used as a 2 channel 2 GS/s digitizer by enabling dual edge sampling (DES). In DES mode ADC samples the input twice during the 1 GHz cycle. This is used for time-of-flight processing, described in section 5.3. A 4 channel CAEN N6724 digitizer with 100 MS/s sampling rate and 14 bits was used to read out gas ionization detector or silicon detector pulses, described in section 5.5. An external clock generator, based on AD9548, provides a 50 MHz square wave which the digitizers use to create the sampling clock with a phase-locked loop (PLL). Additionally an external start signal is provided to one of the digitizers by another, so the start of the acquisition is synchronized.

5.2 Analogue front-end electronics

The typical analogue electronics for time-of-flight ERDA described in section 3.3 form the basis of signal processing also in the case of digitizers. Fig. 15 shows how the digitizers are connected to the amplifiers.

The digitizers used in this work have 50 Ω single-ended inputs and fixed voltage ranges. The range can be used between fully positive or fully negative voltages, since the ADC input is differential and there is a user adjustable DAC feeding the other input of the ADC.

The T1 and T2 timing signals are amplified by a wideband DC to 300 MHz amplifier (Phillips Scientific 776), with a voltage gain of 10. The amplifier has two independent low-impedance outputs capable of driving 50 Ω loads. The CAEN N6751 digitizer has a 1 V_{p-p} range and the input should not be allowed to exceed 3 V, which means the MCP gain should be adjusted by tuning the voltage over the MCP so that the output remains below 300 mV. Alternatively attenuators can be used after the amplification. The goal is to achieve high enough amplification for the digitizers to be able to pick up small pulses while keeping the maximum pulse amplitude safe for digitization.

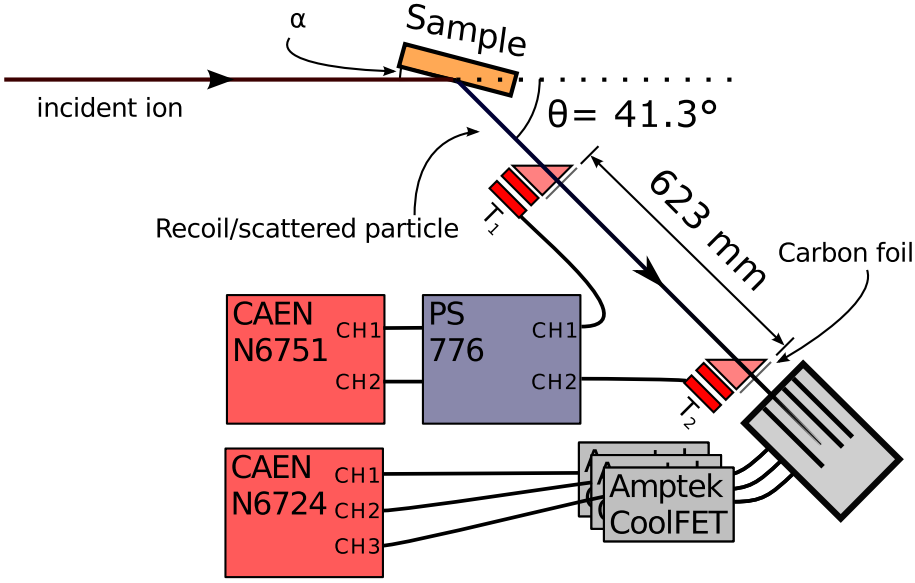

FIGURE 15 Schematic of the Jyväskylä ERDA setup with the digitizers (red). The signals from detectors are digitized after appropriate amplifiers. Reprinted from Ref. [55], PII, with permission from Elsevier.

Gas ionization detector signals are amplified by a charge sensitive preamplifier, Amptek A250CF CoolFET. The amplifier is the lowest noise general purpose CSP on the market. The preamplifier consists of a A250 operational amplifier followed by a 2x voltage gain amplifier, the nominal gain of the amplifier is 0.64 µV/electron, for a 50 Ω load the gain is reduced by a factor of two. The CAEN N6724 digitizer used has a nominal 2.25 V_{p-p} range, which seems a bit too large considering the typical signal might be 10 000 to 1 000 000 electrons, corresponding to 3 mV to 300 mV on the digitizer input. However the signal due to vibrations, as explained in section 4.2.4, is superimposed on this signal. The digitizer input range must be sufficiently large to account for CSP output signal pile-up and this superimposed low frequency signal, unless a high pass filter is installed between the preamplifier and the digitizer.

5.3 Time-of-flight pulse processing

There are three important effects that affect the resolution in any time spectrometer: jitter, walk and drift. *Jitter* refers to a random statistical fluctuations, *walk* is error in timing which is somehow proportional to the input signal amplitude or shape and *drift* is the variation of timing properties due to aging of components or temperature effects [56].

In digital electronics drift tends to be small, due to reduction of complex analogue

circuitry. Jitter inherent in digitizers is related to sample clock generation. Most often the sample clock is based on a crystal oscillator and a PLL which can be controlled to achieve stable multiplication of the oscillator frequency. The pulse processing always introduces some jitter and walk, which should be minimized by selection of appropriate algorithms and parameters.

The time-of-flight was determined by the N6751 digitizer either self-triggering to the T2 signal, or using an analogue circuitry to provide an external trigger from the T2 signal. The digitizer captures pulses on two independent channels simultaneously, one for T1 and one for T2. Since the channels share a common time base, the software algorithm has to detect the rising edge of a pulse and give this point an exact time. The number of samples between the pulses determines the time difference between T1 and T2 signals. An example of this is plotted in Fig. 16.

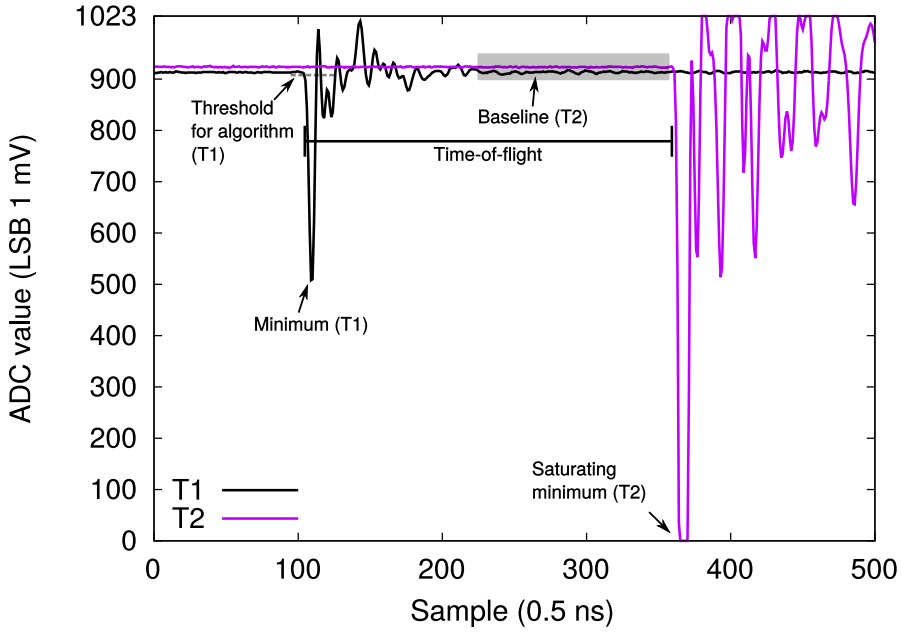

FIGURE 16 Digitized T1 and T2 pulses after amplification. The time-of-flight is determined by timing the pulses on a common time scale, set by the sampling rate of the digitizer. Reprinted from Ref. [55], PII, with permission from Elsevier.

5.3.1 Interpolation

The digitizer used for timing has a sampling rate of 2 GS/s when DES mode is used. This gives a sampling interval of 500 ps. Since the goal is to achieve at least 200 ps timing resolution it is therefore imperative to use interpolation of some kind to achieve sub-sample resolution. The timing information is pulse-like, so methods suitable only for periodic waveforms must be disregarded. The interpolation method should suit the needs of the timing algorithm and preferably not require too much resources, especially CPU time.

Timing algorithms similar to those used in analogue electronics can be implemented when it is possible to evaluate the waveform $V(t)$ at any t, where $t_i \leq t < t_{i+1}$ from the digitized waveform where ith sample is $V(t_i)$. Alternatively timing algorithms can operate on only the discrete-time waveform and use interpolation only to refine the result. Here we introduce some methods intended to be used in the former case, where waveform can be evaluated at an arbitrary point in time.

An obvious choice is to use linear interpolation between two adjacent samples $V(t_i)$ and $V(t_{i+1})$. Then the continuous waveform becomes

$$V(t) = \frac{V(t_{i+1}) - V(t_i)}{(t_{i+1} - t_i)}(t - t_i) = \frac{V(t_{i+1}) - V(t_i)}{t_s}(t - t_i) \tag{24}$$

where t_i is the largest value smaller than t. This function is now piecewise-defined by first order polynomials. While it is continuous, it is not smooth, since the slopes of the piecewise polynomials can be different. In order to achieve a function which is smooth it is possible to use higher order polynomials. A common choice is to use third order polynomials. The resulting function is then called a cubic spline.

A spline constructed like this goes through every point of data, but interpolating splines also exist, such as B-splines. These are formed by a set of points known as knots which do not have to be points of the original data. The spline is fitted using least squares to data. Alternatively it is possible to smooth or filter the data before constructing an exact spline. In this study spline interpolation was used, both with first (linear) and third order (cubic) splines. The optional smoothing of data with an arbitrary kernel was implemented, but not used.

One might also be tempted to use the perfect reconstruction which according to sampling theorem exists for band-limited signals, using a formula given by Shannon [57]. Both this ideal sinc filter and splines can produce unwanted results when the data is not ideal. The most notable nonideality is input saturation, i.e. the digitized voltage exceeds the range of the ADC. A practical lower computational cost version of the sinc filter is a windowed sinc filter called a Lanczos

filter [58]. The Lanczos kernel is defined as

$$L(x) = \begin{cases} 1 & \text{if } x = 0 \\ \dfrac{\sin(\pi x)}{\pi x}\,\dfrac{\sin(\pi x/a)}{\pi x/a} & \text{if } -a < x < 0 \text{ or } 0 < x < a \\ 0 & \text{otherwise.} \end{cases} \tag{25}$$

The interpolation formula is simply a convolution with the Lanczos kernel,

$$V(t) = \sum_{i=t_i-a+1}^{t_i+a} V(t_i)L(t-i). \tag{26}$$

The above formula was implemented and used with $a = 2$.

5.3.2 Timing algorithm

The simplest timing algorithm is perhaps the humble level trigger. The time of a pulse is determined as the time when the voltage exceeds certain predetermined level. Provided that the signal has a fast rise time and low noise the level triggering can have excellent timing resolution. The resolution is usually limited by considerable timing walk in case of slow signals and large jitter in noisy signals.

In many, if not in most, time-of-flight instruments analogue constant fraction discriminators (CFD) are used. The discriminator outputs a logic pulse, after some delay, giving the time when a signal reaches certain fraction of full amplitude. The circuitry sums the original waveform with an attenuated, delayed and inverted version of itself and uses the zero crossing of that pulse to fire the logic pulse. The delay determines the point of full amplitude, with the inherent assumption that the input is somewhat step like. The attenuation factor gives the fraction of full amplitude used in the timing. Commercially available analogue CFD modules differ in some details in implementation and may offer some improvements over the fundamental method described here.

The CFD method can be implemented digitally by seeking the zero crossing

$$V(t) - f \cdot V(t - t_d) = 0. \tag{27}$$

If the delay parameter t_d is shorter than signal rise time the timing is sensitive to only the rising part of the pulse. The corresponding analogue method is known as amplitude and risetime compensated timing (ARC) [59, 60]. For saturating signals this is a necessity, as the full amplitude can not be determined reliably. In the software implementation the pulse is first found by a level trigger and baseline removal, smoothing, interpolation and ARC algorithm are applied to find the precise timing point. The left hand side of Eq. 27 is visualized in Fig. 17,

where ARC timing is used to time two different pulses. The zero crossing can be found by approaching the point first stepwise and finally using Newton's method to find the root more precisely and faster.

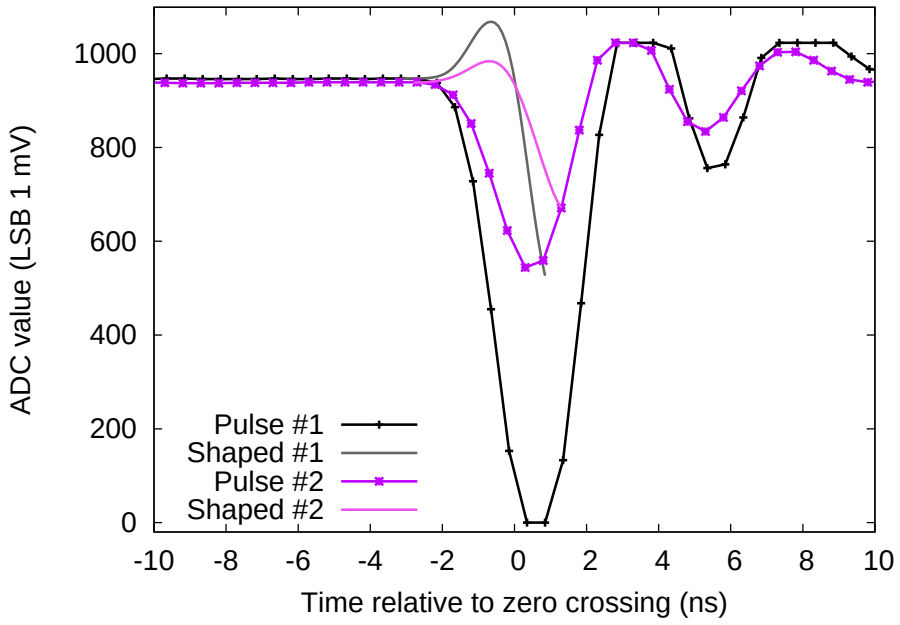

FIGURE 17 Two T2 pulses with different amplitudes together with the shaped waveforms used in the timing. The shaped waveform uses the ARC algorithm with parameters $t_d = 1.5$ (0.5 ns samples) and $f = 0.5$ and cubic spline interpolation. The baseline has been restored to the shaped pulse. Reprinted from Ref. [55], PII, with permission from Elsevier.

5.3.3 Timing resolution and efficiency

The time-of-flight resolution was investigated by scattering beams of 5.1 MeV ^{4}He and 6.8 MeV ^{12}C from a 1 nm thick evaporated gold film on silicon. Due to the low stopping of He at this energy the scattered spectrum will have a narrow peak. The width of the peak is limited by the timing resolution of the spectrometer. From the digitized events only those scattering from Au are selected based on the energy and the long tail due to scattering from the substrate are removed. The parameters of the timing algorithms can then be varied and timing data reprocessed rapidly. The resulting peak is then fitted with a gaussian. The FWHM of the fit is plotted in Fig. 18. These results were obtained using cubic spline interpolation. Differences between linear, cubic and Lanczos interpolation using the best timing parameters were negligible (< 10 ps).

The number of events with valid timing information is plotted in Fig. 19. The algorithm will reject some low amplitude pulses with certain parameter combinations. The detection efficiency must therefore also be investigated when timing parameters are varied.

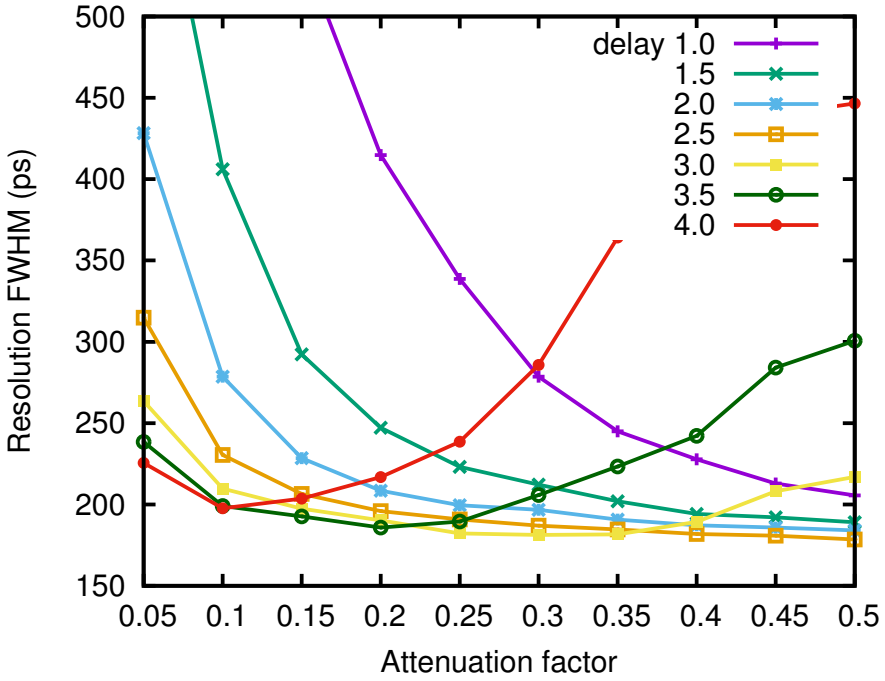

FIGURE 18 Timing resolution achieved for scattered He as T1 timing algorithm parameters t_d and f are varied. Reprinted from Ref. [55], PII, with permission from Elsevier.

5.4 Data acquisition

The algorithms and pulse processing are realized in practice as a computer program, which communicates through the operating system with the digitizers and then processes the acquired data. The software can dump raw data and later recall it, process these events with the appropriate algorithms to form list-mode data and sort the list-mode events into coincidence events in order to allow online monitoring of the measurement. The flow of data is plotted schematically in Fig. 20.

All pulse processing can be performed on-line, the primary limitations are mass storage size and speed when raw events are stored or the maximum data rate between the digitizer and the PC. The digitizers used in this work are connected using a two channel CAEN A3818 PCI-Express optical link card, allowing 80 MB/s

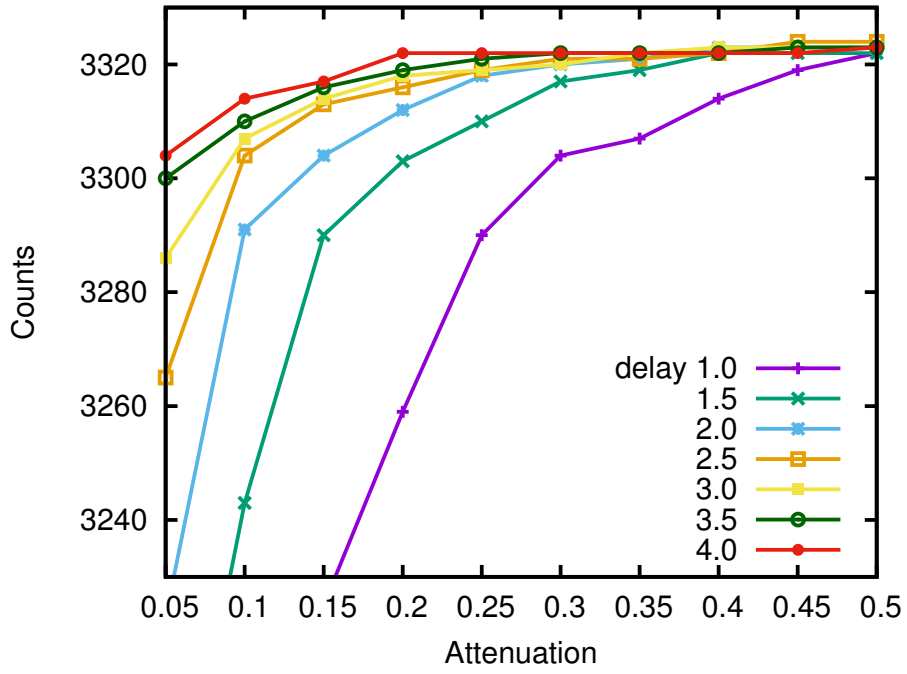

FIGURE 19 Number of counts in the peak from which resolution in Fig. 18 was determined. Some combinations will cause small amplitude pulses to be rejected.

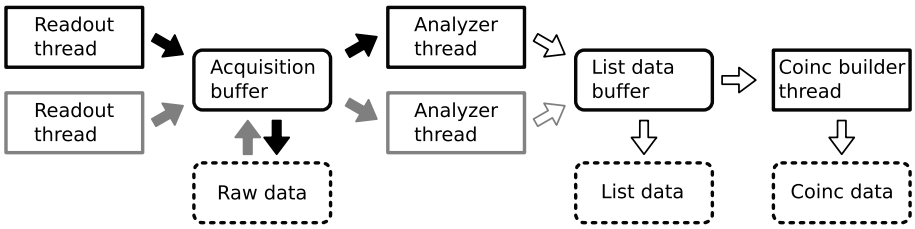

FIGURE 20 The flow of data in the data acquisition software. Reprinted from Ref. [55], PII, with permission from Elsevier.

data rate from both digitizers simultaneously. More digitizers can be connected by daisy chaining the optical links.

In addition to controlling the acquisition the software allows the user to select appropriate algorithms and change their parameters on-line. The main window of the user interface is shown in Fig. 21. Simple histograms can also be viewed in the user interface.

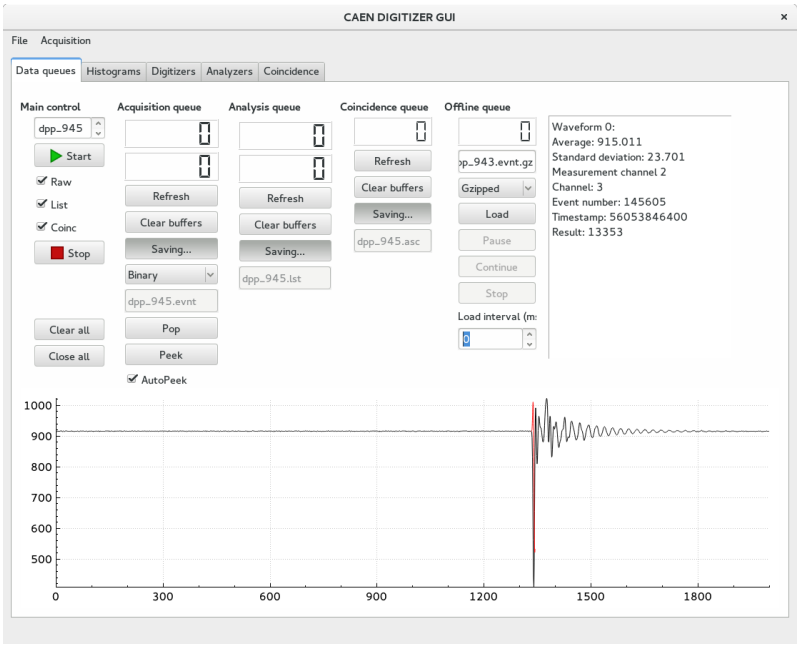

FIGURE 21 The main user interface of the data acquisition software.

5.5 GIC pulse processing

Techniques employing recursive digital triangle, trapezoidal and cusp shapers [61, 62] allowing real-time shaping of charge sensitive preamplifier signals are standard techniques in high resolution and high count rate spectroscopy. In IBA such techniques are used in conjunction with silicon drift detectors in particle induced X-ray emission (PIXE) measurements to detect X-rays, while in most other IBA experiments the more traditional combination of shaping amplifiers and peak-sensing ADCs, or multichannel analyzers (MCA), is used.

Trapezoidal shapers implemented using an FPGA on a digitizer are available commercially, either as standalone units or integrated to the detector, like in the case of some X-ray detectors. The implementation of the trapezoidal shaper, or interchangeably trapezoidal filter, always fundamentally uses the same recursive formula, but there are differences to improve pile-up performance, timing properties or stability. The fundamental formula for a trapezoidal filter with rise time k (in samples) and flat top m is [62]

$$s(n) = s(n-1) + v(n) - v(n-k) - v(n-l) + v(n-l-k), \tag{28}$$

where $l = k + m$, and $v(n)$ is the nth digitized sample. The step response of this filter is a trapezoid, see Fig. 22. The simplicity of the formula is the key to its success – it can be implemented with minimal hardware. Yet the inclusion of a flat top makes it superior to some analogue electronics, since it reduces or eliminates ballistic deficit, i.e. the filter is not sensitive to rise time variations present in Ge γ-detectors.

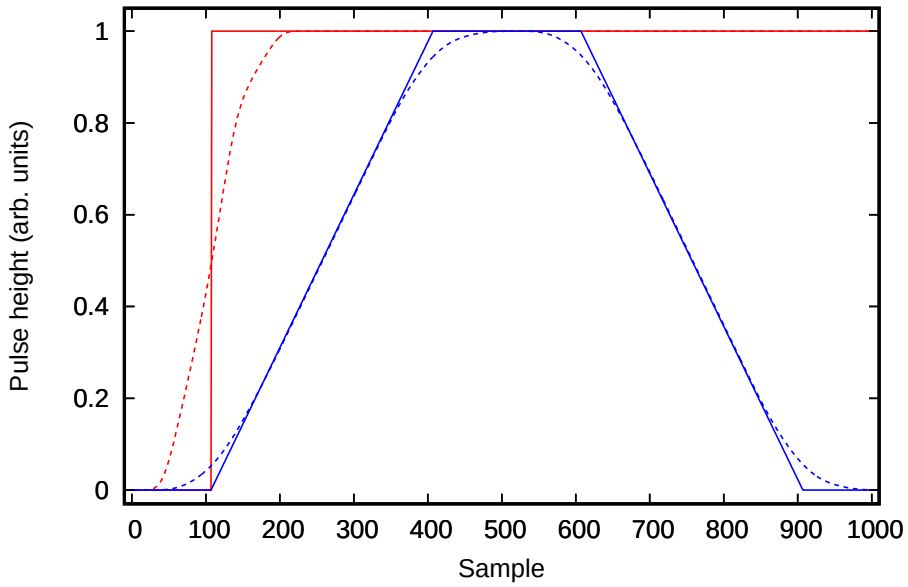

FIGURE 22 A step function (red) and the corresponding trapezoid (blue) with rise time $k = 300$ and flat top duration $m = 200$ samples. The dashed lines show a more realistic pulse with longer rise time. The trapezoid maximum height is not sensitive to the shape of the pulse.

The CAEN DPP-PHA firmware implements a trapezoidal shaper which has a notable difference to the traditional implementation. Additional recursive filter is used to create a trigger signal, improving timing performance, enabling rise-time discrimination and pile-up rejection. The pulses separated by the trigger filter but not by the trapezoidal filter can be rejected. Improved pile-up rejection is a key advantage over analogue electronics. The trigger filter will be more sensitive to high frequency noise than the trapezoidal filter, as it should have much faster response i.e. shorter filtering time constant.

The CAEN trigger filter uses a windowed average, which is simply the sum of n previous samples, and is probably implemented using a recursive formula. The number of samples, n, has to be a power of two between 1 and 32. The exact reason for this limitation is not specified by the manufacturer. Here we denote the averaged input signal v_{avg}. The user can decide whether to use a single or double derivative as the trigger signal, $\mathrm{cr}(n)$ and $\mathrm{cr2}(n)$ respectively. They are defined as

$$\mathrm{cr}(n) = v_{\mathrm{avg}}(n) - v_{\mathrm{avg}}(n-d) \text{ and} \tag{29}$$

$$\mathrm{cr2}(n) = \mathrm{cr}(n) - \mathrm{cr}(n-d). \tag{30}$$

The delay d can be set with one sample accuracy. If the delay is larger than the input signal rise time the response of the cr filter to a typical preamplifier pulse is a unipolar pulse. The cr2-filter provides a bipolar pulse, where the zero crossing acts like a 50% CFD. The averaging is used to improve signal-to-noise ratio, but

the hardware limitation of a maximum of 32 samples averaging may be insufficient for some applications.

The trigger and pulse height filters can operate on a stream of samples after decimation. Two, four or eight successive digitized samples can be averaged. The filters can operate on these averaged samples. By decimating by a factor of two the 100 MS/s digitizer effectively acts as a 50 MS/s digitizer and 32 samples averaging in the trigger filter now corresponds to 640 ns. In most of the measurements in this study a factor of two decimation was used, since it allows lower trigger threshold, enabling the detection of approximately 100 keV hydrogen.

Timing the difference from T2 signal to the GIC anode signal can be used to measure the drift time of electrons to the grid. This measurement relies on the synchronization of the digitizer time stamps. The synchronization is established by the FPGA clocks running phase locked to the common external clock. The T2 timestamp is determined by an external signal triggering the acquisition and the GIC anode timestamp is determined by the timing filter self-triggering. With the settings used in this work the timestamp resolution of the N6724 and N6751 digitizers are 20 ns and 16 ns, respectively. The timestamp jitter is illustrated in Fig. 23. In addition to the jitter the timing filter will contribute to the timing resolution. The drift time is used to measure position of the ionizing particle as explained in Section 4.2. In Fig. 24 the timestamp difference is plotted for all detected oxygen recoils. The high energy edge (surface) is affected by the recoil kinematics, which can be seen to correlate with the drift time.

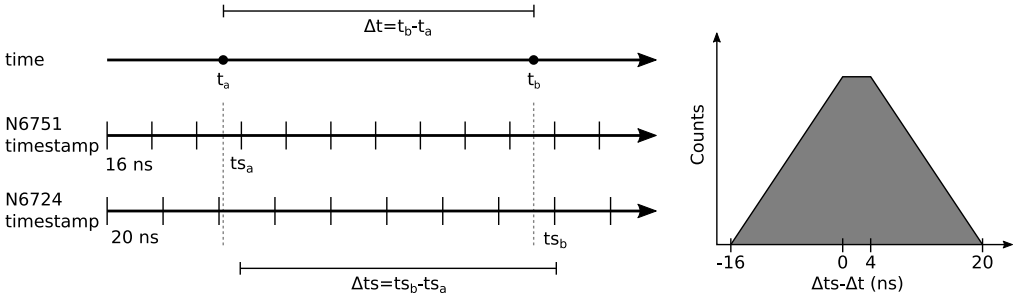

FIGURE 23 Jitter in time difference measurements between N6751 digitizer triggered by a signal occuring at t_a (timestamp ts_a is a multiple of 16 ns) and N6724 digitizer triggered by a signal at t_b (timestamp ts_b is a multiple of 20 ns). The digitizers have a different time stamp resolution, but the timestamps are synchronized. The time difference between timestamps Δts has a maximum uncertainty of 16 ns + 20 ns = 36 ns compared to the true time difference Δt.

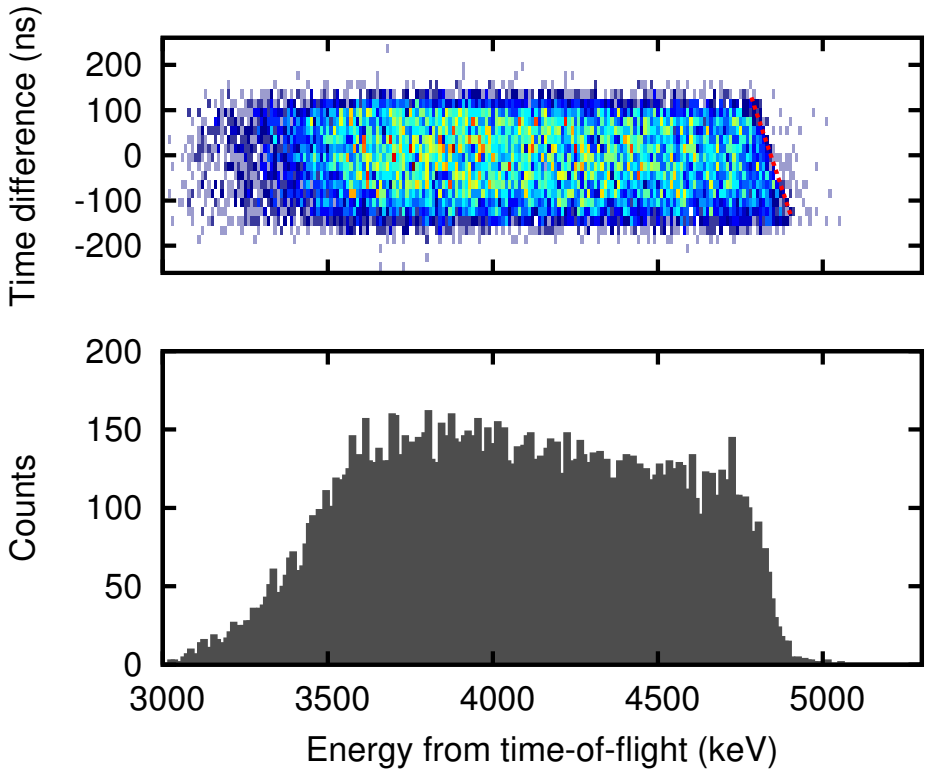

FIGURE 24 T2 – GIC anode timestamp difference and energy spectra of oxygen recoils from a thin film. The dashed red line in the upper figure is the expected energy of surface recoils, Eq. 8, if the timestamp difference is assumed to be linearly proportional to the lateral (scattering plane) position of the recoil at the GIC entrance. The θ in Eq. 8 is also assumed to be given by this position directly, i.e. multiple scattering and beam spot effects are ignored.

6 SIMULATIONS ON GIC RELATED EFFECTS AND BACKGROUND

A time-of-flight system with a gas ionization chamber has not been thoroughly studied before, especially when combined with a digitizing data acquisition. The limitations of position sensitivity and sources of background are of particular interest. More insight on and means to study the operation of the current spectrometers will be valuable in the design of some future instruments, especially those operating at the low energy limit.

The digitizing data acquisition presented in Chapter 5 provides means to study individual events in time-of-flight–energy histograms in detail. Not all effects are identifiable by this method.

In order to study current instrumentation without excessive dedicated measurements, and to design future instrumentation simulation codes were developed to model the ionization chamber and data acquisition related effects. These codes were designed to be used with MCERD simulation code, but they can be used independently.

MCERD [33] is a Monte Carlo simulation code intended to reproduce ERDA spectra including multiple and plural scattering in the sample, scattering in detector foils, detector geometry and beam spot related effects.

6.1 Simulation codes

6.1.1 MCERD

MCERD transports an incident ion through a sample, allowing it to scatter from target nuclei and be slowed down also via electronic stopping given originally by 1996 version of SRIM [63], referred to as ZBL by authors of Ref. [33]. Electronic stopping values from SRIM 2013 [17] were used in this study. The electronic stopping is subject to straggling using the Yang formulae [23]. In each MCERD run the recoil atom of interest is selected and recoils are created from every depth which contain the recoiling atoms with equal probability, irrespective of the concentration or recoil cross sections at the depth. The recoil cross section determined by the energy of the incident ion and the recoiling angle is however used to give a weight to the event. Concentrations can also be factored in the event weights later.

The resulting recoils are then transported out of the sample and through the detectors. The time of passage through timing detectors is tabulated relative to the time the recoiling reaction took place.

For the purposes of this study MCERD was modified to include recoil cascades in the gas ionization chamber. Significant energy transfer to recoils in the detector window is relatively rare event, but when it happens the energy lost in the window by the original incident particle and the subsequent recoils together will reduce the observed anode signal. Recoiling gas atoms can similarly cause a pulse height deficit if a recoil is ejected from the active volume or it hits the electrodes. The low energy threshold for recoil tracking was set to 2 keV. Some tracks of typical recoils from the sample and recoiled gas atoms are plotted in Fig. 25.

The (E, x, y, z) values of the tracked recoils inside the detector are written to a file whenever a new recoil is created, the recoil traverses from the window to the gas volume or at minimum of 10 keV intervals (1 keV at lowest energies). Energy lost to both untracked and tracked collisions are also tabulated.

6.1.2 Ionization signals

The tracks generated by MCERD are converted into ionization tracks by first looking up the W-factor, i.e. average energy required to generate an electron-ion pair. The $W(Z, E)$ values are based on dedicated measurements, where the response of each element has been studied over a broad energy range. The energy of particles after the entrance window has been calculated from the time-of-flight measurement, from which energy loss in the T2 carbon foil and the silicon nitride

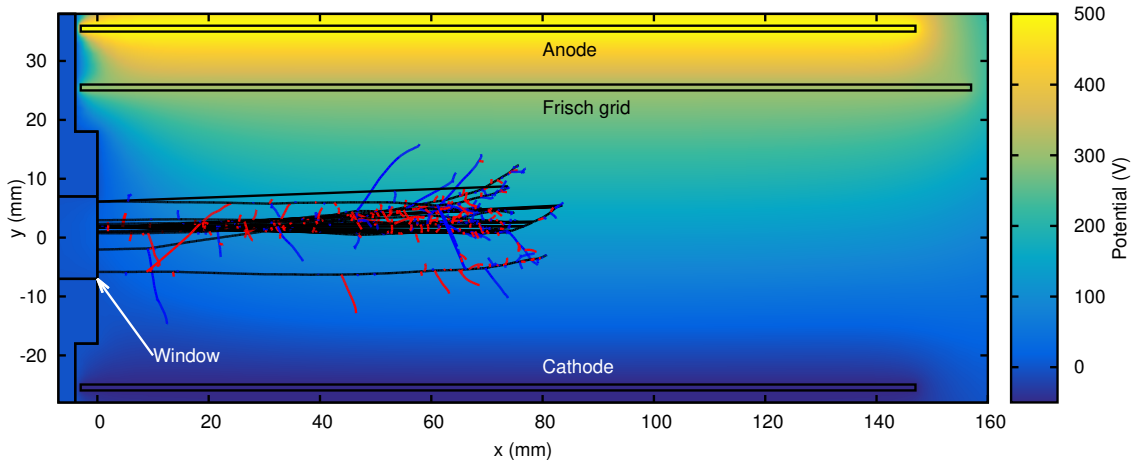

FIGURE 25 Tracks of 5 MeV to 7 MeV titanium recoils from the sample (black) and recoiling gas atoms, hydrogen (red) and carbon (blue) plotted on top of the electric potential in the gas ionization chamber. Figure from PIII, [64].

entrance window has been subtracted. The amount of electrons has been calculated from anode pulse heights, using a calibrated preamplifier and digitizer. The W data for ^{28}Si has been plotted in Fig. 26. The mean energy $W(E)$ is estimated from this data. The results for ^{1}H, ^{4}He, ^{12}C, ^{16}O, ^{28}Si and ^{63}Cu are plotted in Fig. 27. The measurements were also performed for ^{6,7}Li, ^{10,11}B, ^{27}Al, ^{29,30}Si, ^{35,37}Cl, ^{65}Cu, ^{79,81}Br, ^{127}I and ^{197}Au. The differences between isotopes was within experimental uncertainty.

Electrons are created in the gas volume by placing an electron in an appropriate (x, y, z) location so that the ion will have lost W of energy since the last electron was created. The same W of energy per electron is used for the ion and any subsequent recoils in the gas. This way the number of electrons, $N = E/W$, will match the tabulated W-data and will be comparable to measurements. The problem with this approach is that the light low energy gas recoils H and C will ionize quite differently from e.g. Si ion. The simulations will therefore be based on average on correct number of electrons, but the spatial distribution will not be perfectly accurate. Additionally the fluctuations in W have not been measured, so the simulations will not correctly reproduce the inherent fluctuation in the number of electrons produced.

To speed up calculations the number of electrons can be reduced by a factor of ten without issues, as much more than ten electrons worth of noise will be added in a later step of the simulations and the increased granularity in simulated waveforms becomes insignificant.

The code can be used to simulate entire populations of electrons, allowing them to drift in the electric field with optional diffusion. Alternatively the average waveform resulting from an electron starting the drift near a certain (x, y, z) point

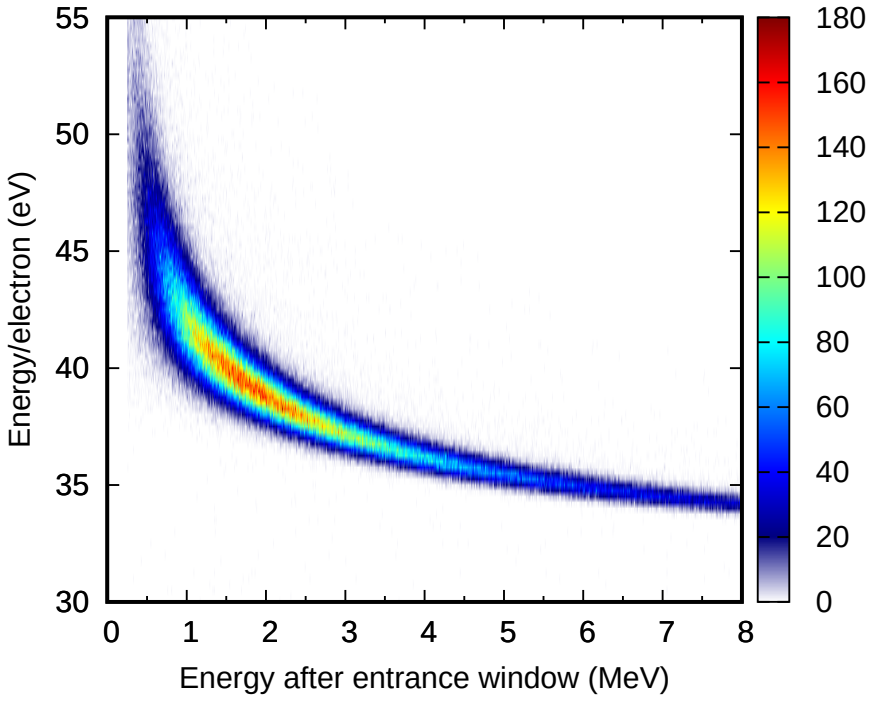

FIGURE 26 The energy of ^{28}Si calculated from time-of-flight is compared to the energy divided by collected charge from anode (electrons). The average energy required to produce an ion pair can be extracted from this experimental data.

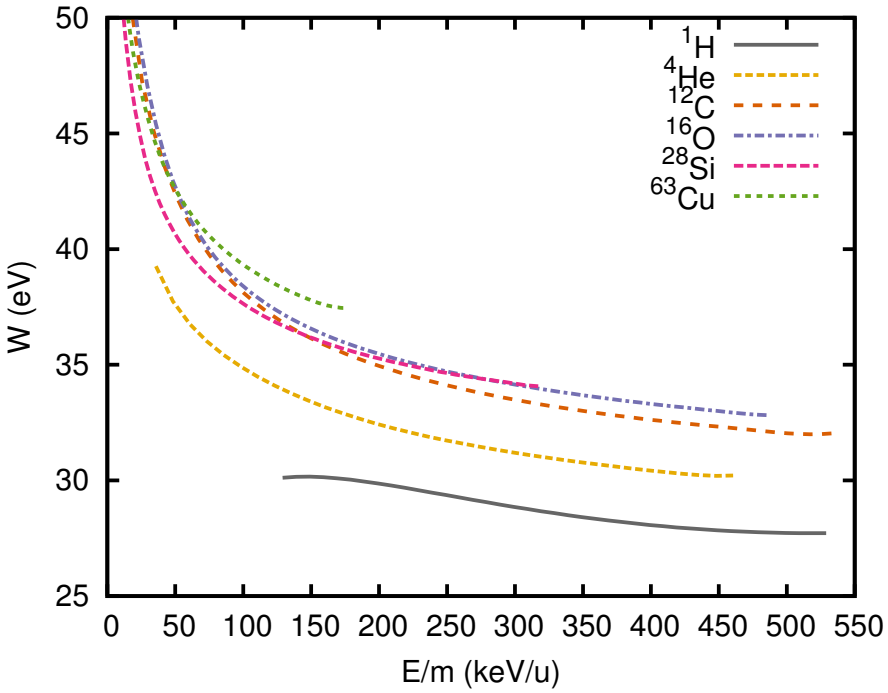

FIGURE 27 Average energy required to produce an ion pair plotted for hydrogen, helium, carbon, oxygen, silicon and copper ions. Figure from PIII, [64].

can be precomputed using Eq. 15 and Eq. 16.

In these simulations a precomputed detector was used. The electric field and effective weighting potentials of the anode and cathode were calculated in 2D using finite element method program FEMM 4.2 [65]. The field between the electrodes was calculated in the xy plane perpendicular to the electrodes in xz plane.

The charge induced on an electrode by an electron, $q(x, y, t)$, was precalculated for each (x, y, t) point with 0.5 mm and 2 ns spacing. The total induced charge pulse can now be calculated rapidly as a sum over n electrons

$$Q(t) = \sum_{i=0}^{n} q(x_i, y_i, t - t_i). \tag{31}$$

Some characteristic charge pulses $q(x, y, t)$ are plotted in Fig. 28.

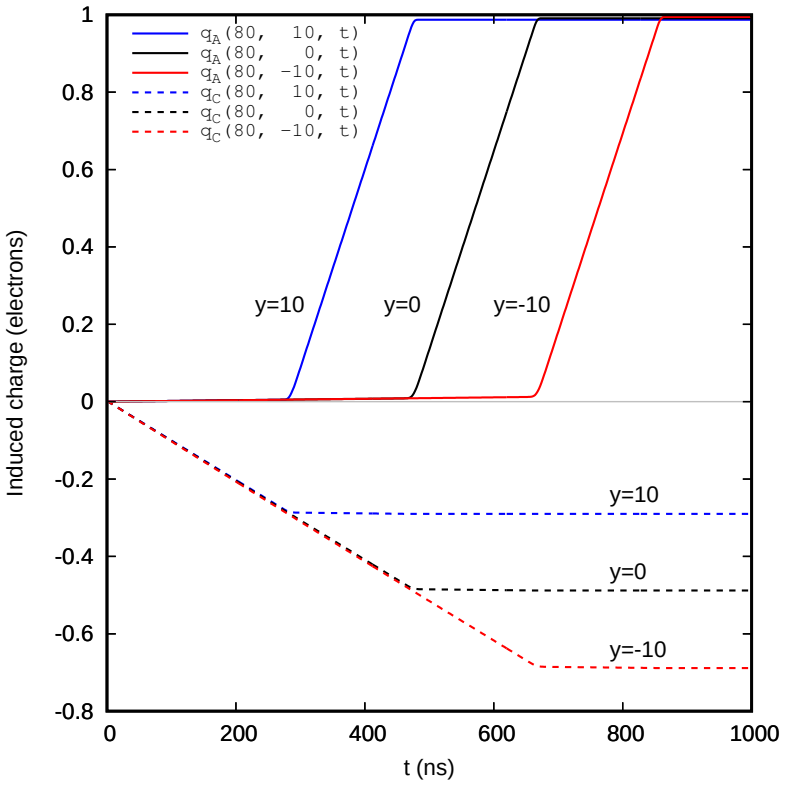

FIGURE 28 Characteristic anode q_A and cathode q_C charge pulses $q(x, y, t)$ computed for an electron placed initially at $(x = 80\,\text{mm}, y, t = 0)$. The blue, black and red pulses correspond to a lateral position y of 10, 0 and -10 millimeters, respectively. The cathode signal amplitude is position dependent while the delay of the rising edge of the anode pulse is due to position dependent drift time to grid.

6.1.3 Data acquisition

Data acquisition related effects were studied by modeling the time-of-flight and energy signal processing. Events are created from MCERD tabulated recoils from the sample and the previously calculated induced charge pulses. Individual events are picked according to the weights given by MCERD in random order.

For the simulated GIC preamplifier signals the Eq. 29 and Eq. 30 defined in section 5.5 are used to model the signal shaping by the digitizer. The electronics noise of the corresponding experimental setup is matched, although with an assumption that the noise is white. Examples of simulated signals and the responses of the filters are plotted in Fig. 29.

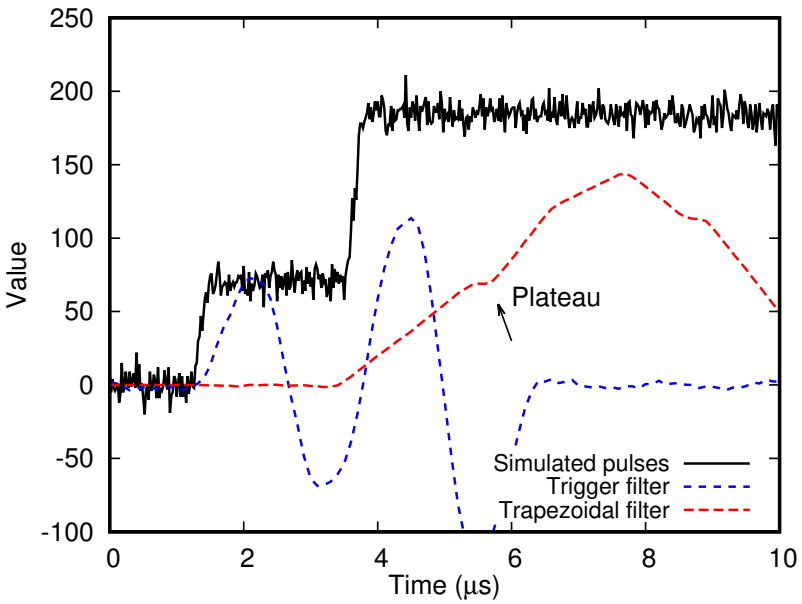

FIGURE 29 Simulated noisy pulses and the responses of the trigger and trapezoidal filter. The rise time of the trapezoidal filter is 2 µs. These pulses can be separated by the trigger filter, but not perfectly by the trapezoidal filter. With these parameters the pulses are marked as pile-up and rejected, as the simulated detector system also would do. Figure from PIII, [64].

Based on the results of the GIC shaping and timing detector hits timestamped list-mode data are created, where the time stamps are subjected to jitter in the same way as in the actual digitizer-based acquisition setup. Same tools can be used to manipulate both the measured and simulated list-mode data, for example to find time-of-flight–energy coincidences.

6.2 Ionization chamber position sensitivity

6.2.1 Linearity and resolution of drift time measurement

Average induced charge pulses on the anode for an electron initially appearing at $t = 0\,\mathrm{s}$ in some (x, y) coordinates are plotted in Fig. 28. As described by Eq. 31 the observed pulse is a superposition of individual electron responses and therefore the observed pulse in a GIC depends not only on the number of electrons created, but also by their spatial distribution. From data presented in Fig. 28 linear position dependence on lateral coordinate would be expected based on both drift time and cathode anode pulse height comparison. However electrons created near the entrance window will exhibit longer drift time to anode and less position sensitivity in the cathode amplitude. The window effects have also influenced the design of gas ionization chambers that achieve position sensitivity by comparing the pulses induced on multiple subdivided electrodes [66].

In Fig. 30 the drift time simulated between T2 and anode pulses is seen to be quite well linear for typical oxygen recoils of approximately 4 MeV. The timing filter functions like a 50% CFD, achieving good timing resolution in spite of small deviations in pulse shape.

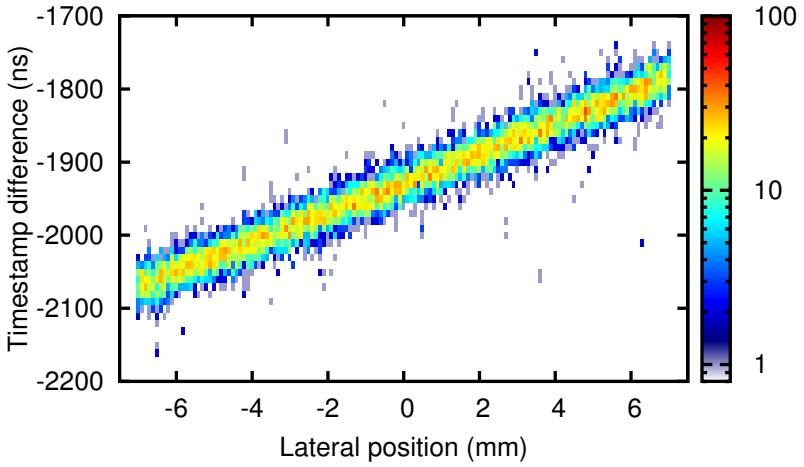

FIGURE 30 Simulated T2 – GIC anode event time stamp difference as a function of the recoil lateral position at the entrance of the GIC. Figure from PIII, [64].

6.2.2 Residual position sensitivity on anode

The inherent position sensitivity may also be a limitation. Some authors speculate on the possibility of grid inefficiency affecting the resolution of their ionization chamber [67]. This effect can, of course, be measured. The issue is however that

this is not the dominant term affecting energy resolution and the contibution may be easier to estimate by simulating.

Generally the grid inefficiency reduces the observed pulse heights on the anode as can be seen in Fig. 31. The significance of this effect to the resolution increases for larger detectors.

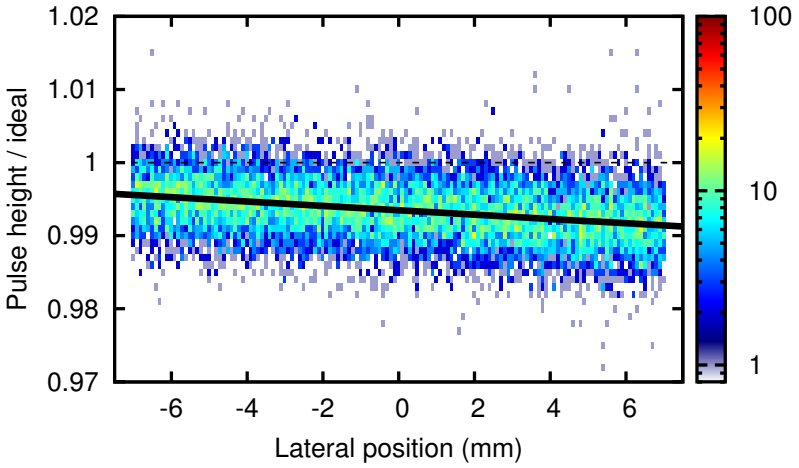

FIGURE 31 Normalized anode pulse height variation due to lateral position, i.e. position at the detector window in the scattering plane. These approximately 4 MeV simulated oxygen recoils show position dependent pulse height deficit associated with grid inefficiency. Figure from PIII, [64].

6.3 Background

Background in time-of-flight–energy spectra is defined as events where the time-of-flight and energy do not correspond to each other. Individual events outside the 2D selections (Fig. 32) used in analysis are clearly background, but on the other hand this background is of little significance since it does not affect the results of the analysis.

There are several contributing factors to the background in ERDA time-of-flight–energy spectra. Some are due to the direct physical limitations, such as large angle scattering and nuclear stopping effects in the detectors. These effects are count-rate independent. Other effects are due to the electronic detector response, signal processing and data acquisition. These effects, such as pile-up and wrong coincidences are mostly count-rate dependent.

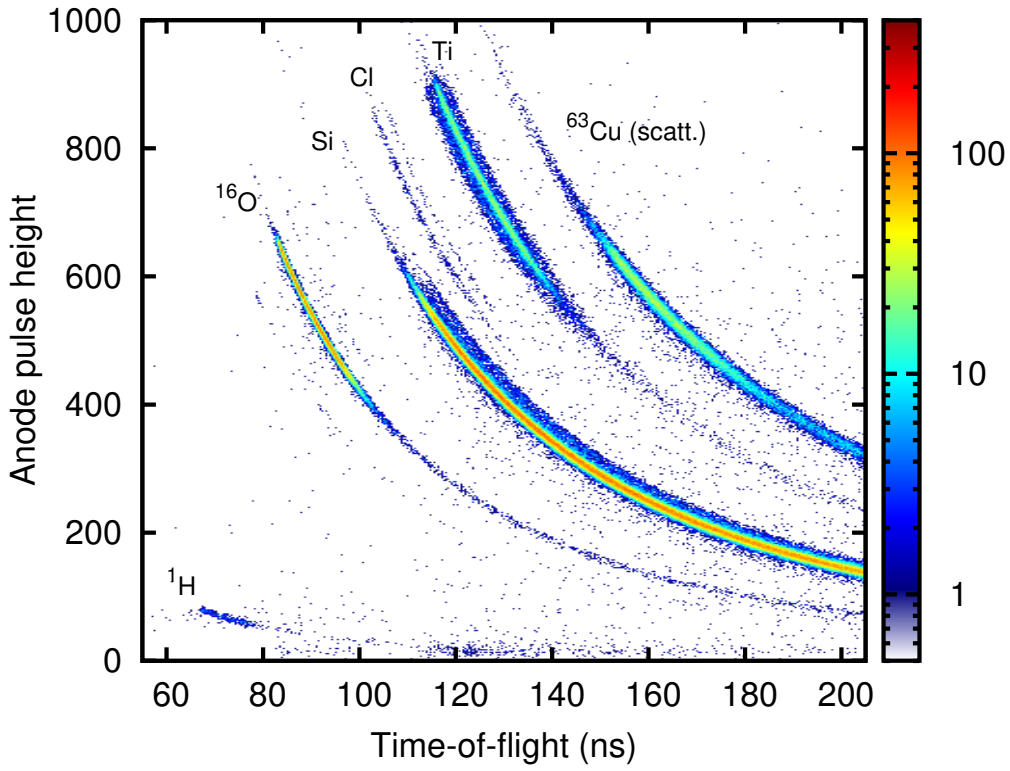

FIGURE 32 Time-of-flight–E histogram of the TiO_2 sample measured with a 13.3 MeV ^{63}Cu beam. Background events can be clearly seen outside the "bananas" corresponding to different elements and isotopes. Figure from PIII, [64].

6.3.1 Count rate independent

Background events are observed even at low count rates. There are some events with apparently correct time-of-flight, but with smaller than anticipated energy. Energy loss between the time-of-flight and energy measurements or pulse height deficit in the energy detector are the possible mechanisms.

Energy loss in the entrance window of the GIC can lead to greater loss of energy than what is typical if there are recoils created in the entrance window. Fig. 33 shows a simulated low count rate measurement, in which the background is mostly due to this contribution.

Large angle scattering in the entrance window or in the detector gas may lead to energy loss and pulse shape deviations if either the scattering or the recoiling particle hits the walls or otherwise exits the active volume of the GIC. Fig. 34 shows measurements and simulations with different pressures. The dramatic reduction of energy resolution in measurements, especially with energetic heavy ions is believed to be associated with either scattering in the gas or too long range of incident particles. The simulations partially reproduce this effect, which is particular to the detector geometry used. The effect becomes clearer at lower pressures in

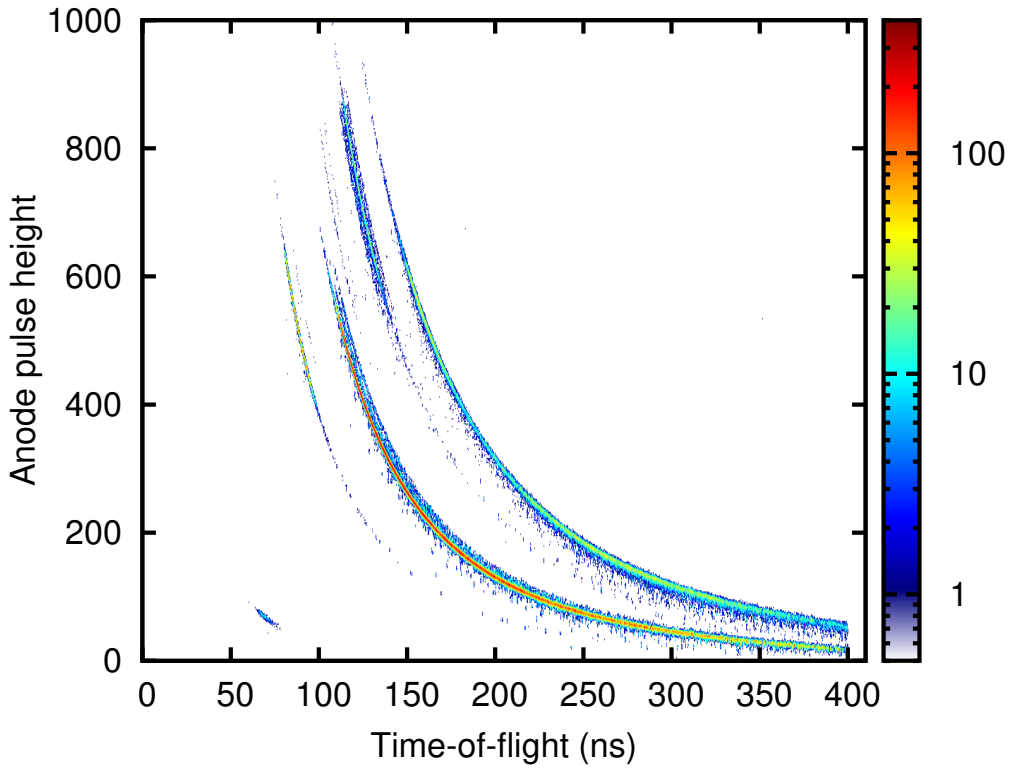

FIGURE 33 Simulated very low count rate time-of-flight–E histogram. Background events correspond to count rate independent mechanisms. Events with correct time-of-flight, but tails in the energy measurement are seen for heavy recoils.

the simulations, suggesting the results are highly sensitive to the stopping data used in the simulations. Even at lower pressures the effect in the simulations is mainly due to long range of incident particles, not due to recoil cascades.

6.3.2 Count rate dependent

With increasing count rate several mechanisms contributing to background become increasingly important. These effects are highly pulse processing and data acquisition dependent, so while these effects are more or less present in every time-of-flight ERDA system, the details and intensity may vary greatly.

Pile-up is the result of the ionization chamber signals of at least two recoils being interpreted as one. Strategy used to reduce pile-up, and the limitations of pile-up rejection, were discussed in section 5.5.

Wrong time-of-flight energy coincidence can happen when two recoils pass through T1 and T2 consecutively. When the first recoil misses the energy detector the energy signal of the second recoil can be confused with the time-of-flight of the

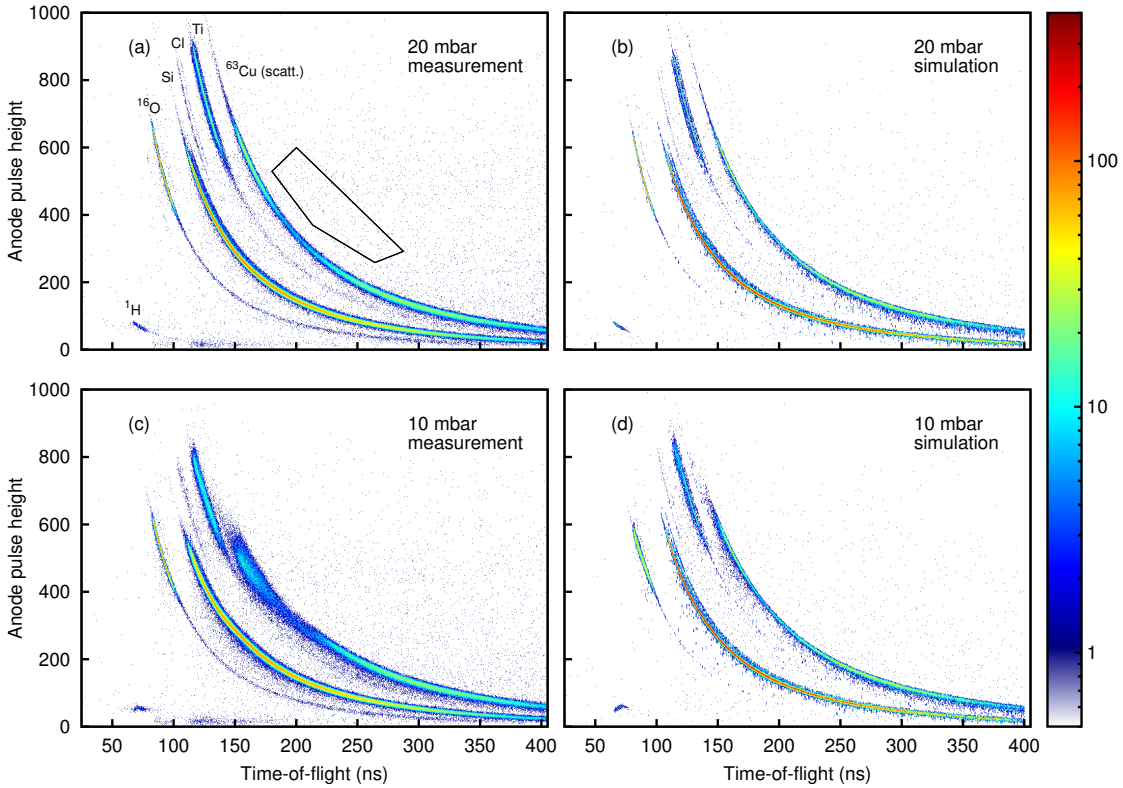

FIGURE 34 Time-of-flight–E histograms of the TiO_2 sample. The histogram (a) was measured and (b) was simulated with 20 mbar GIC pressure, which is sufficient to stop all recoils in the active volume. The histogram (c) was measured and (d) was simulated with 10 mbar pressure. Each of the histograms have 350000 events in total. Figure from PIII, [64].

first recoil, creating uncorrelated background. This type of background depends on the ability to resolve successive T1 and T2 hits withing the timing window. Should both of the recoils hit the energy detector the result is likely some pile-up, which could also be rejected.

Wrong T1 - T2 coincidences are possible when a recoil is overtaken by another recoil after T1, but before T2. The time-of-flight of this event will be shorter than what it was supposed to be for the first recoil, but longer than expected for the second. Again, this effect is also accompanied possibly by pile-up, unless one of the recoils miss the energy detector. In inverted start systems, where time-of-flight is computed as the difference between T2 and delayed T1 hits (T2 acts as a trigger), instead of the direct T1 - T2 difference (T1 acts as a trigger), some low energy background is created by recoils with longer time-of-flight than the timing window. The undetected T1 hit might be provided by another recoil, creating background with random time-of-flight.

The detection efficiencies and solid angles of individual detectors will play a role in the intensity of these contributions above, since many of the sources of back-

ground are multiple detector effects.

A high count rate 2D histogram is plotted in Fig. 35, where the background is generated mostly by the abovementioned mechanisms.

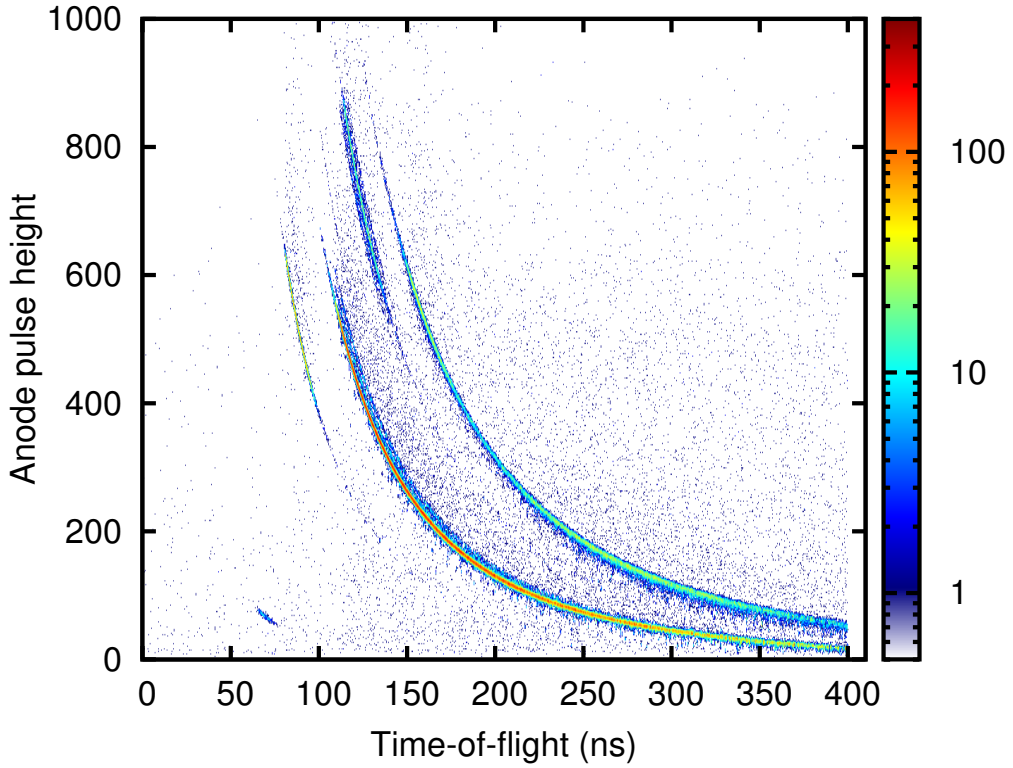

FIGURE 35 Simulated high count rate time-of-flight–E histogram. The number of coincidence counts per second was approximately 13000, which leads to severe pile-up in the GIC and wrong coincidences.

6.4 Low energy large solid angle conceptual spectrometer

The simulation codes and methods presented in previous chapters can be extended to study instruments that are yet to be built. In PIV a large solid angle ($>$ 1 msr) spectrometer based on currently available technology was presented and these codes were used to predict the position resolution and depth resolution in the near-surface region.

6.4.1 Large solid angle concept

The large solid angle concept is based on the idea that a good depth resolution can be achieved using low energy (below 6 MeV) incident beams even if time-of-flight length is reduced. Bringing the timing detectors closer to the sample increases the solid angle. Low energies also allow the use of lower GIC pressure, allowing a larger unsupported entrance window and thereby an increase in the solid angle. A schematic of the proposed geometry is presented in Fig. 36. Also the recoiling cross sections will be higher at lower energies. This makes time-of-flight ERDA of easily damaged samples possible. The use of low energy heavy ions has been proposed and studied also previously [6, 7, 68, 69].

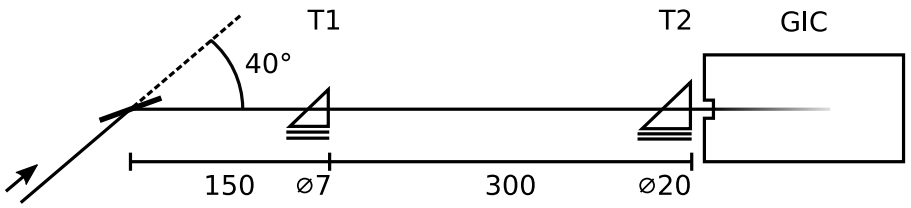

FIGURE 36 Proposed detector geometry for a low energy time-of-flight ERDA spectrometer. Figure from PIV.

The challenge in using low energy very heavy ions is the hydrogen detection, since the recoil energies will be very low. For this reason the detector concept should be used with medium heavy ions such as $^{35/37}$Cl or ^{39}K from a tandem accelerator. Conventional RF ion sources can produce beams of triply charged Ar [70] making the concept usable with existing 2 MV single ended electrostatic accelerators and ^{40}Ar beam. The primary limitations compared to higher energy ERDA are the reduced probing depth and increased multiple scattering [68]. Thin films containing mostly light elements can still be quantitatively depth profiled.

6.4.2 Geometry

Since the large solid angle increases kinematic broadening a simple Monte Carlo code was written to compute the effects of finite beam spot size, sample tilt and varying time-of-flight length on surface recoils created by a monoenergetic beam. The code can be used to answer also how much the kinematics can be compensated using one dimensional position sensitivity. The results are presented in Fig. 37. A simple MC code was preferred over analytical calculations because of the geometrical complexity. Surface approximation was chosen in order to keep the code simple, although recoils originating slightly below the surface do not follow the surface approximation perfectly due to differing path lengths inside

the sample. Depth resolution for recoils originating from deep in the sample is limited by straggling and multiple scattering.

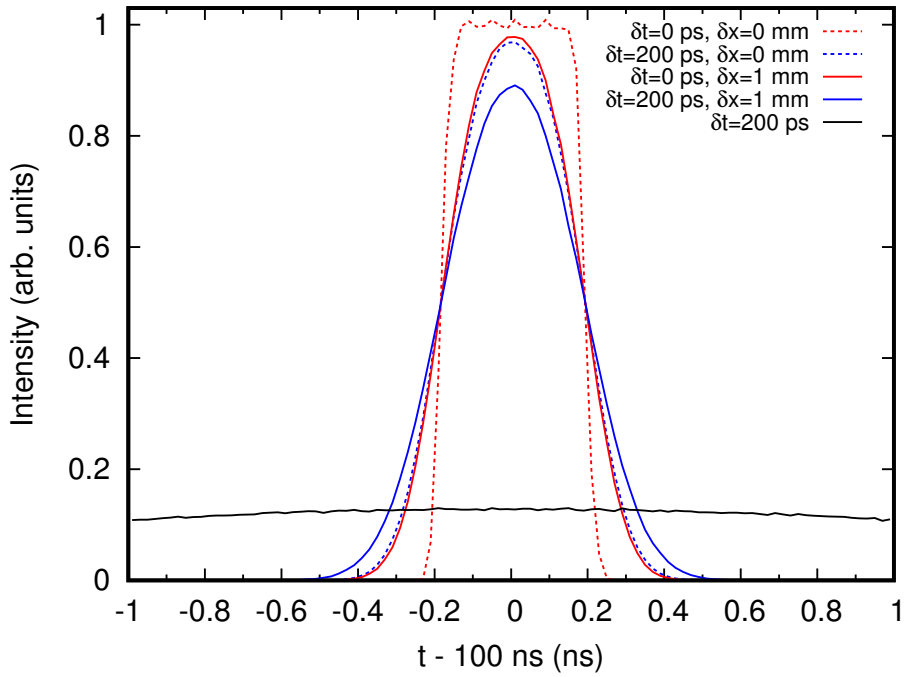

FIGURE 37 Effective timing resolution for ideally 100 ns time-of-flight recoils. With perfect timing and one dimensional position resolution the broadening caused by a finite beam spot remains. The 200 ps timing resolution (blue lines) and 1 mm position resolution (solid red and blue lines) cause some further broadening. However the situation is considerably better than having no position resolution at all (black).

6.4.3 Depth resolution

A measurement of a Li_2CO_3 sample was simulated using the modified MCERD. The proposed detector geometry (Fig. 36) was used. The simulations compute full tracks of recoils in the gas ionization detector, which allows the prediction of position sensitivity accurately.

The simulated list mode data was fed to Potku [32] analysis program, which can take advantage of position sensitive data in analysis. The depth profiles are plotted in Fig. 38. The depth resolution near the surface is better than 5 nm for such a sample, which is comparable to current spectrometers.

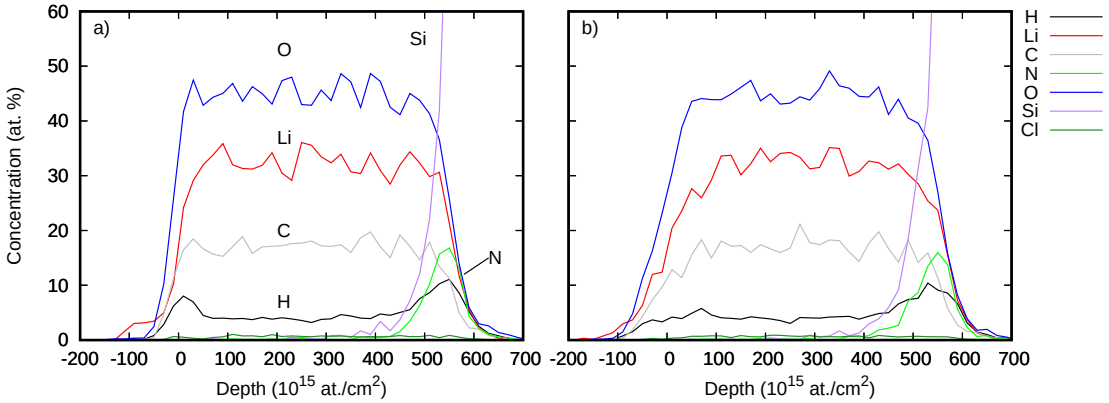

FIGURE 38 Depth profiles with simulated 5.1 MeV ^{39}K beam of a 57 nm thick Li_2CO_3 sample on silicon. Some H was simulated to be present at the surface and H and N at the interface. In (a) one dimensional position sensitivity was used, while no position information was used in (b). The depth resolution at the surface in (a) is comparable with existing time-of-flight ERDA spectrometers. Figure from PIV.

7 DISCUSSION AND CONCLUSIONS

Time-of-flight ERDA is experiencing a renaissance as ion beam analysis methods are facing tough competition from more affordable and convenient analytical techniques. ToF-ERDA is very well suited for high-throughput analysis, since the experimental parameters do not have to be tailored specifically to suit the particular sample, there is no need for reference measurements and the elements can be unambiguously identified. Simultaneous detection of all elements, including hydrogen, present in a sample is nigh impossible with other methods.

Digitizing data acquisition has already replaced the traditional shaping amplifiers in many applications. In IBA steps are taken towards faster and higher resolution measurements while keeping the cost of the equipment reasonable. Affordable and well scalable digitizers are a part of this equation.

The use of thin films of only few or tens of nanometers for a variety of applications ranging from microelectronics to biomedical devices is increasingly important. The elemental characterization for process development and quality control of such films is often beneficial or necessary. Ion beam analysis provides the means for quantitative light element depth profiling, including analysis of materials vulnerable to ion beam induced damage if large solid angle detector systems are developed.

Gas ionization chambers used as energy detectors provide improved mass resolution and enable the operation at lower energies, which makes it possible to use smaller accelerators. The detector combined with digitizing data acquisition makes low energy ERDA with position sensitive detectors accessible for the IBA community while providing a depth resolution that can only be exceeded by magnetic spectrometers.

This thesis introduces a position sensitive high resolution gas ionization chamber

energy detector for time-of-flight ERDA, where the position sensitivity is based on the measurement of drift time. The drift time analysis works from the lowest detectable energies and from hydrogen to heavier recoils using the same time-to-angle calibration.

A fully digitizing low cost data acquisition, which can also be tailored to suit applications other than ToF-ERDA was developed. The time-of-flight pulse processing is done entirely in software, allowing rapid development and easy systematic studies of timing and detection efficiency related parameters.

Additionally computer simulation codes and methodology to study the detectors and data acquisition related effects were developed. Both scattering in the detector entrance windows and count-rate related background mechanisms were modeled. Simulations of full 2D time-of-flight–energy histograms with background were performed for the first time.

REFERENCES

[1] R. Groleau, S. Gujrathi, and J. Martin. Time-of-flight system for profiling recoiled light elements. *Nucl. Instrum. Methods* 218 (1983) 11.

[2] J. Thomas, M. Fallavier, D. Ramdane, N. Chevarier, and A. Chevarier. High resolution depth profiling of light elements in high atomic mass materials. *Nucl. Instrum. Methods* 218 (1983) 125.

[3] J. L'Ecuyer, C. Brassard, C. Cardinal, J. Chabbal, L. Deschênes, J. P. Labrie, B. Terreault, J. G. Martel, and R. St.-Jacques. An accurate and sensitive method for the determination of the depth distribution of light elements in heavy materials. *J. Appl. Phys.* 47 (1976) 381.

[4] J. L'Ecuyer, C. Brassard, C. Cardinal, and B. Terreault. The use of ^{6}Li and ^{35}Cl ion beams in surface analysis. *Nucl. Instrum. Methods* 149 (1978) 271.

[5] G. Dollinger, C. Frey, A. Bergmaier, and T. Faestermann. Elastic recoil detection with single atomic layer depth resolution. *Nucl. Instrum. Meth. B* 136 (1998) 603.

[6] C. Kottler, M. Döbeli, F. Glaus, and M. Suter. A spectrometer for low energy heavy ion ERDA. *Nucl. Instrum. Meth. B* 248 (2006) 155.

[7] S. Giangrandi, T. Sajavaara, B. Brijs, K. Arstila, A. Vantomme, and W. Vandervorst. Low-energy heavy-ion TOF-ERDA setup for quantitative depth profiling of thin films. *Nucl. Instrum. Meth. B* 266 (2008) 5144.

[8] Z. Siketić, I. Bogdanović Radović, and M. Jakšić. Development of a time-of-flight spectrometer at the Ruder Bošković Institute in Zagreb. *Nucl. Instrum. Meth. B* 266 (2008) 1328.

[9] M. Laitinen, M. Rossi, J. Julin, and T. Sajavaara. Time-of-flight – Energy spectrometer for elemental depth profiling – Jyväskylä design. *Nucl. Instrum. Meth. B* 337 (2014) 55.

[10] M. Msimanga, D. Wamwangi, C. Comrie, C. Pineda-Vargas, M. Nkosi, and T. Hlatshwayo. The new Heavy Ion ERDA set up at iThemba LABS Gauteng: Multilayer thin film depth profiling using direct calculation and Monte Carlo simulation codes. *Nucl. Instrum. Meth. B* 296 (2013) 54.

[11] P. Sigmund. *Particle Penetration and Radiation Effects*. Springer, 2006.

[12] E. Rutherford. The scattering of α and β particles by matter and the structure of the atom. *Philos. Mag.* 6th ser. 21 (1911) 669.

[13] J. B. Marion and F. C. Young. *Nuclear Reaction Analysis: Graphs and Tables*. North-Holland Publishing Company, 1968.

[14] J. S. Lilley. *Nuclear Physics: Principles and Applications*. John Wiley & Sons, 2001.

[15] J. L'Ecuyer, J. Davies, and N. Matsunami. How accurate are absolute Rutherford backscattering yields. *Nucl. Instrum. Methods* 160 (1979) 337.

[16] H. H. Andersen, F. Besenbacher, P. Loftager, and W. Möller. Large-angle scattering of light ions in the weakly screened Rutherford region. *Phys. Rev. A* 21 (1980) 1891.

[17] J. F. Ziegler, M. D. Ziegler, and J. Biersack. SRIM – The stopping and range of ions in matter (2010). *Nucl. Instrum. Meth. B* 268 (2010) 1818.

[18] E. Rauhala. Energy loss. In: *Handbook of Modern Ion Beam Materials Analysis*. Ed. by J. R. Tesmer and M. Nastasi. 1995. Chap. 2.

[19] W. H. Bragg and R. Kleeman. On the α particles of radium, and their loss of range in passing through various atoms and molecules. *Philos. Mag.* 6th ser. 10 (1905) 318.

[20] J. R. Sabin and J. Oddershede. Theoretical stopping cross sections of C-H, C-C and C=C bonds for swift protons. *Nucl. Instrum. Meth. B* 27 (1987) 280.

[21] N. Barradas, A. Bergmaier, K. Mizohata, M. Msimanga, J. Räisänen, T. Sajavaara, and A. Simon. Determination of molecular stopping cross section of ^{12}C, ^{16}O, ^{28}Si, ^{35}Cl, ^{58}Ni, ^{79}Br, and ^{127}I in silicon nitride. *Nucl. Instrum. Meth. B* 360 (2015) 90.

[22] W. K. Chu. Calculation of energy straggling for protons and helium ions. *Phys. Rev. A* 13 (1976) 2057.

[23] Q. Yang, D. O'Connor, and Z. Wang. Empirical formulae for energy loss straggling of ions in matter. *Nucl. Instrum. Meth. B* 61 (1991) 149.

[24] *ICRU Report 31: Average Energy Required to Produce An Ion Pair*. Washington, D.C. USA: International Commission on Radiation Units and Measurements, 1979.

[25] B. B. Rossi and H. H. Staub. *Ionization Chambers and Counters*. McGraw-Hill Book Company, 1949.

[26] J. M. Valentine and S. C. Curran. Average energy expenditure per ion pair in gases and gas mixtures. *Rep. Prog. Phys.* 21 (1958) 1.

[27] M. Chemtob, B. Lavigne, J. Chary, V. D. Nguyen, N. Parmentier, J. P. Noel, and C. Fiche. Some experimental results on W values for heavy particles. *Phys. Med. Biol.* 22 (1977) 208.

[28] M. S. Miller and J. W. Boring. Total inelastic energy loss by heavy ions stopped in a gas. *Phys. Rev. A* 9 (1974) 2421.

[29] N. P. Barradas. Rutherford backscattering analysis of thin films and superlattices with roughness. *J. Phys. D Appl. Phys* 34 (2001) 2109.

[30] M. Mayer. SIMNRA, a simulation program for the analysis of NRA, RBS and ERDA. *AIP Conf. Proc.* 475 (1999) 541.

[31] F. Schiettekatte, M. Chicoine, S. Gujrathi, P. Wei, and K. Oxorn. Allegria: a new interface to the ERD program. *Nucl. Instrum. Meth. B* 219-220 (2004) 125.

[32] K. Arstila, J. Julin, M. Laitinen, J. Aalto, T. Konu, S. Kärkkäinen, S. Rahkonen, M. Raunio, J. Itkonen, J.-P. Santanen, T. Tuovinen, and T. Sajavaara. Potku – New analysis software for heavy ion elastic recoil detection analysis. *Nucl. Instrum. Meth. B* 331 (2014) 34.

[33] K. Arstila, T. Sajavaara, and J. Keinonen. Monte Carlo simulation of multiple and plural scattering in elastic recoil detection. *Nucl. Instrum. Meth. B* 174 (2001) 163.

[34] F. Schiettekatte. Fast Monte Carlo for ion beam analysis simulations. *Nucl. Instrum. Meth. B* 266 (2008) 1880.

[35] W. Shockley. Currents to conductors induced by a moving point charge. *J. Appl. Phys* 9 (1938) 635.

[36] S. Ramo. Currents induced by electron motion. *P. IRE* 27 (1939) 584.

[37] Z. He. Review of the Shockley–Ramo theorem and its application in semiconductor gamma-ray detectors. *Nucl. Instrum. Meth. A* 463 (2001) 250.

[38] D. Green. *The Physics of Particle Detectors*. Cambridge University Press, 2000.

[39] L. G. Christophorou, G. S. Hurst, and A. Hadjiantoniou. Interaction of thermal electrons with polarizable and polar molecules. *J. Chem. Phys* 44 (1966) 3506.

[40] G. Schultz and J. Gresser. A study of transport coefficients of electrons in some gases used in proportional and drift chambers. *Nucl. Instrum. Methods* 151 (1978) 413.

[41] U. Fano. Ionization yield of radiations. II. The fluctuations of the number of ions. *Phys. Rev.* 72 (1947) 26.

[42] K. Kleinknecht. *Detectors for particle radiation*. 2nd ed. Cambridge University Press, 1998.

[43] G. Alkhazov, A. Komar, and A. Vorob'ev. Ionization fluctuations and resolution of ionization chambers and semiconductor detectors. *Nucl. Instrum. Methods* 48 (1967) 1.

[44] F. Sauli. *Principles of operation of multiwire proportional and drift chambers*. CERN, 1977.

[45] O. Frisch. *Isotope analysis of uranium samples by means of their α-ray groups.* British Atomic Energy Project Report BR-49. Unpublished. 1944.

[46] O. Bunemann, T. Cranshaw, and J. A. Harvey. Design of grid ionization chambers. *Can J. Res.* 27a (1949) 191.

[47] R. Bevilacqua, A. Göök, F.-J. Hambsch, N. Jovančević, and M. Vidali. A procedure for the characterization of electron transmission through Frisch grids. *Nucl. Instrum. Meth. A* 770 (2015) 64.

[48] A. Göök, F.-J. Hambsch, A. Oberstedt, and S. Oberstedt. Application of the Shockley–Ramo theorem on the grid inefficiency of Frisch grid ionization chambers. *Nucl. Instrum. Meth. A* 664 (2012) 289.

[49] A. Al-Adili, F.-J. Hambsch, R. Bencardino, S. Oberstedt, and S. Pomp. Ambiguities in the grid-inefficiency correction for Frisch-grid ionization chambers. *Nucl. Instrum. Meth. A* 673 (2012) 116.

[50] W. Assmann. Ionization chambers for materials analysis with heavy ion beams. *Nucl. Instrum. Meth. B* 64 (1992) 267.

[51] J. Julin, M. Laitinen, and T. Sajavaara. Time-of-flight ERD with a 200 mm^2 Si_3N_4 window gas ionization chamber energy detector. *Nucl. Instrum. Meth. B* 332 (2014) 271.

[52] M. Döbeli, C. Kottler, M. Stocker, S. Weinmann, H.-A. Synal, M. Grajcar, and M. Suter. Gas ionization chambers with silicon nitride windows for the detection and identification of low energy ions. *Nucl. Instrum. Meth. B* 219 (2004) 415.

[53] G. F. Knoll. *Radiation Detection and Measurement*. 4th ed. John Wiley & Sons, 2010.

[54] *IEEE Standard for Digitizing Waveform Recorders*. IEEE Std 1057-2007. 2008. URL: http://ieeexplore.ieee.org/servlet/opac?punumber=5981349.

[55] J. Julin and T. Sajavaara. Digitizing data acquisition and time-of-flight pulse processing for ToF-ERDA. *Nucl. Instrum. Meth. B* 366 (2016) 179.

[56] T. J. Paulus. Timing electronics and fast timing methods with scintillation detectors. *IEEE T. Nucl. Sci.* 32 (1985) 1242.

[57] C. E. Shannon. Communication in the presence of noise. *P. IRE* 37 (1949) 10.

[58] C. E. Duchon. Lanczos filtering in one and two dimensions. *J. Appl. Meteorol.* 18 (1979) 1016.

[59] R. L. Chase. Pulse timing system for use with gamma rays on Ge (Li) detectors. *Rev. Sci. Instrum.* 39.9 (1968) 1318.

[60] Z. H. Cho and R. L. Chase. Improved amplitude and rise time compensated timing with Ge detectors. *IEEE T. Nucl. Sci.* NS19.1 (1972) 451.

[61] V. Radeka. Optimum signal-processing for pulse-amplitude spectrometry in the presence of high-rate effects and noise. *IEEE T. Nucl. Sci.* 15 (1968) 455.

[62] V. T. Jordanov and G. F. Knoll. Digital synthesis of pulse shapes in real time for high resolution radiation spectroscopy. *Nucl. Instrum. Meth. B* 345 (1994) 337.

[63] J. F. Ziegler, J. P. Biersack, and U. Littmark. *The Stopping and Range of Ions in Matter*. Pergamon, 1985.

[64] J. Julin, K. Arstila, and T. Sajavaara. Simulations of time-of-flight ERDA spectrometer performance. *Rev. Sci. Instrum.* 87 (2016) 083309.

[65] D. C. Meeker. *Finite Element Method Magnetics (FEMM) version 4.2*. http://www.femm.info/.

[66] H. Timmers, T. Ophel, and R. Elliman. Simplifying position-sensitive gas-ionization detectors for heavy ion elastic recoil detection. *Nucl. Instrum. Meth. B* 161-163 (2000) 19.

[67] A. Müller, M. Döbeli, M. Suter, and H.-A. Synal. Performance of the ETH gas ionization chamber at low energy. *Nucl. Instrum. Meth. B* 287 (2012) 94.

[68] M. Döbeli, C. Kottler, F. Glaus, and M. Suter. ERDA at the low energy limit. *Nucl. Instrum. Meth. B* 241 (2005) 428.

[69] S. Giangrandi, K. Arstila, B. Brijs, T. Sajavaara, A. Vantomme, and W. Vandervorst. Depth resolution optimization for low-energy ERDA. *Nucl. Instrum. Meth. B* 261 (2007) 512.

[70] E. J. Knystautas. Extending the Energy Range of a 7 MV Van de Graaff Using Triply-Charged Beams: Applications to Neon and Argon Ions. *IEEE T. Nucl. Sci.* 26 (1979) 1470.

ORIGINAL PAPERS

PI

TIME-OF-FLIGHT ERD WITH A 200 mm^2 Si_3N_4 WINDOW GAS IONIZATION CHAMBER ENERGY DETECTOR

by

Jaakko Julin, Mikko Laitinen, Timo Sajavaara

Nuclear Instruments and Methods in Physics Research Section B: Beam Interactions with Materials and Atoms 332 (2014) 271–274

Nuclear Instruments and Methods in Physics Research B 332 (2014) 271–274

Contents lists available at ScienceDirect

Nuclear Instruments and Methods in Physics Research B

journal homepage: www.elsevier.com/locate/nimb

Time-of-flight ERD with a 200 mm^2 Si_3N_4 window gas ionization chamber energy detector

Jaakko Julin *, Mikko Laitinen, Timo Sajavaara

Department of Physics, University of Jyväskylä, P.O. Box 35, Jyväskylä FI-40014, Finland

ARTICLE INFO

Article history:
Available online 12 March 2014

Keywords:
Elastic recoil detection
Gas ionization chamber
Silicon nitride window

ABSTRACT

Low energy heavy ion elastic recoil detection work has been carried out in Jyväskylä since 2009 using home made timing detectors, a silicon energy detector and a timestamping data acquisition setup forming a time-of-flight–energy telescope. In order to improve the mass resolution of the setup a new energy detector was designed to replace the silicon solid state detector, which suffered from radiation damage and had poor resolution for heavy recoils.

In this paper the construction and operation of an isobutane filled gas ionization chamber with a 14 × 14 mm^2 100 nm thick silicon nitride window are described. In addition to greatly improved energy resolution for heavy ions, the detector is also able to detect hydrogen recoils simultaneously in the energy range of 100–1000 keV. Additionally the detector has position sensitivity by means of timing measurement, which can be performed without compromising the performance of the detector in any other way. The achieved position sensitivity improves the depth resolution near the surface.

1. Introduction

Time-of-flight elastic recoil detection (ToF-ERD) is an ion beam analysis method which is very well suited for light element detection and depth profiling thin film samples. Typically ToF-ERD is performed with energetic heavy ion beams, around 1 MeV/amu, which is suitable for relatively thick films but requires the use of a large accelerator. Depth resolution for <100 nm films can be improved by using a 100–300 keV/amu beam, e.g. 8.5 MeV ^{35}Cl available from tandem accelerators with <2 MV terminal voltage. The disadvantage of the lower energy is the reduced mass resolution, which in a time-of-flight–energy (ToF–E) telescope is set by both the time-of-flight resolution and energy resolution.

In heavy ion ERD both solid state detectors (SSD) and gas ionization chamber (GIC) detectors have been used for recoil ion energy measurement. SSDs have been the choice for most ERD setups, mainly because of their availability as commercial products and ease of use. The resolution of the typically used ion-implanted silicon detectors for heavy ions is, however, quite poor due to straggling in the dead layer, electron–hole recombination and radiation damage [1].

A major problem of the low energy heavy ion detection using a gas ionization chamber (GIC) is the entrance window, which separates the gas from the vacuum and can easily deteriorate the energy resolution of the detector. There has been pioneering use of self-supporting thin silicon nitride windows in gas ionization chambers at ETH Zürich by Döbeli et al. [2] and specifically applied in ERD by Kottler et al. [3]. Gas ionization detectors are not susceptible to radiation damage, but they have been considered to be inconvenient to operate due to perceived difficulty in gas handling and mechanically fragile entrance windows.

In order to have reasonable solid angle for a typical ToF-ERD telescope one would prefer a window area exceeding 100 mm^2, which has previously been possible only by using patterned windows. Silicon nitride windows are created by depositing low-stress silicon nitride on a silicon substrate, typically between 200 and 400 μm thick. The substrate is wet etched selectively, leaving silicon supports. Due to the anisotropy of silicon wafer etching the window holes have a trapezoidal cross-section. Especially with a mosaic of small windows this results in open area of much less than 100% and ambiguous collimation at the window borders.

The energy detector in ToF-ERD telescope has to meet several criteria, such as radiation hardness and good resolution for heavy ions at a count rate of a few kHz. However, as typically the purpose of the energy detector is to achieve mass separation along with the time-of-flight measurement, there are no strict requirements for linear or accurate energy calibration unlike in the case where only a gas ionization detector is used [4] to perform ERD.

* Corresponding author. Tel.: +358 407576906.
E-mail address: jaakko.julin@jyu.fi (J. Julin).

http://dx.doi.org/10.1016/j.nimb.2014.02.076
0168-583X/

In ERD-geometry the depth resolution is severely limited for a large solid angle detector by the kinematic spreading. For this reason one should consider having at least one position sensitive detector to correct for the kinematics in the scattering plane. In ToF-ERD with multi-channel plate (MCP) electrostatic timing detectors it is possible to make the timing detectors position sensitive by using a position sensitive anode [5]. One simple way for the kinematic correction is to use a position sensitive energy detector, such as a silicon strip detector [6]. With ionization chambers a variety of techniques can be employed to achieve position sensitivity, some of which are reviewed by Assmann [7].

In this paper the construction of a new planar electrode gas ionization chamber is described. The detector is shown to meet the criteria on hydrogen detection and position sensitivity.

2. Experimental

The ToF–E telescope installed to a 15° beam line of a 1.7 MV 5SDH-2 Pelletron has two timing detectors, which are based on the Busch [5] design along with the energy detector. The telescope is installed to a 41.3° angle relative to beam with a time-of-flight distance of 623 mm between the detectors. The first detector is located 319 mm and the energy detector 957 mm from the sample. The ToF–E setup is presented previously with the old energy detector in [8].

The detector telescope had previously a 450 mm^2 silicon detector, but the 18 mm circular aperture of the second timing detector limits the solid angle. The new GIC energy detector has been designed to have a window size up to 20×20 mm^2. The 100 nm thick silicon nitride window currently installed is collimated to 14×14 mm^2. Giving the geometry of the telescope and SRIM calculated straggling and range for the hydrogen recoils the electrodes were designed to be 50 mm wide, the same as grid to cathode distance. The grid, anode and cathode are mounted vertically. The length of the electrodes is 150 mm and the entrance window protrudes 3 mm inside the gas volume. These dimensions were based on SRIM simulations where the goal was to stop hydrogen recoils with the larger window and 25 mbar of isobutane.

The detector is a gridded ionization chamber, where the Frisch grid is made of gold plated 100 μm tungsten wire with 1 mm wire pitch. The anode is biased to a positive voltage, typically +500 V, while the cathode is grounded. The grid is held at an intermediate potential of typically +300 V. The anode–grid distance is 10 mm, giving an electric field of 200 V/cm in this volume while the electric field between the grid and the cathode is 60 V/cm. Higher electric field between the grid and the anode improves the efficiency of charge collection through the grid above the 90% optical transmission [9].

The anode can be used to measure position independent ionization, while the cathode signal could be used to measure position sensitive ionization. With the low energy used here, the signal from the cathode is too weak to be detected for some of the recoils, especially those ionizing the gas near the cathode. Increasing the grid–cathode distance would imply a larger portion of the ionization is induced to the cathode, but this would increase the charge collection time and therefore hinder operation at high count rate. Another method of determining the position is to split the anode in a sawtooth pattern, but then the complete anode signal must be summed from two channels, increasing the electronics noise.

The time difference between the second timing detector pulse, and the anode pulse can be used to measure the ionization track position between the grid and the cathode without additional amplifiers or signal splitting. The signal from the anode starts to form only after the first electrons pass through the grid. For ionization occurring near the cathode, the drift time to the grid can be several 100 ns, depending on the electric field strength and pressure. Most of the events arrive within 500 ns coincidence window between the second timing gate and the energy detector.

Both the time-of-flight and energy signals were acquired using waveform digitizers, a 2 GS/s 10-bit digitizer (CAEN N6751) for the time-of-flight signals and 100 MS/s 14-bit digitizer (CAEN N6724) for the GIC signals. The timing measurement is based on triggering to the second timing gate and energy pulses and timestamping between two digitizers, which were synchronized by an external 50 MHz oscillator. The timing resolution is dominated by the timestamp jitter, which is estimated to be 28 ns.

3. Results and discussion

The new energy detector has been in operation in ToF-ERD setup for more than 6 months and during this period hundreds of measurements have been performed. Initially the response of the chamber was expected to change if the gas would become contaminated over time, but for simplicity no gas circulation was realized in the vacuum design shown in Fig. 1. In practice the detector has been used for weeks with the same gas without a significant change in pressure or in energy resolution.

The energy detector is used in coincidence with the time-of-flight measurement, which means that the coincidence window and energy resolution affect the background and sensitivity of the measurement. The wider the coincidence window the more background is introduced, especially at high count rate due to false coincidences. When using a SSD the coincidence window can be as short as few tens of nanoseconds compared to the 500 ns of the GIC. However, the improved mass resolution with the new detector means less false coincidence or other background events fall under the two dimensional ToF–E mass selections.

The improved mass resolution allows the separation of adjacent elements even up to cobalt, which can be separated from Fe and Cu. In Fig. 2 the ToF–E histogram of a cobalt oxide thin film on stainless steel measured using 11.9 MeV ^{63}Cu beam is presented. Isotope separation is clearly evident in the case of measuring the chlorine impurity content from 50 to 100 nm thick AlN films deposited using Atomic Layer Deposition (ALD) with 8.5 MeV ^{35}Cl beam. In Fig. 3 a ToF–E histogram where separation of ^{37}Cl from the scattered ^{35}Cl beam is presented. The ^{37}Cl can be used to quantify the 1.6 at.% chlorine impurity in the sample, although the lower natural abundance of ^{37}Cl will increase the statistical uncertainty. The sample was not expected to contain any chlorine

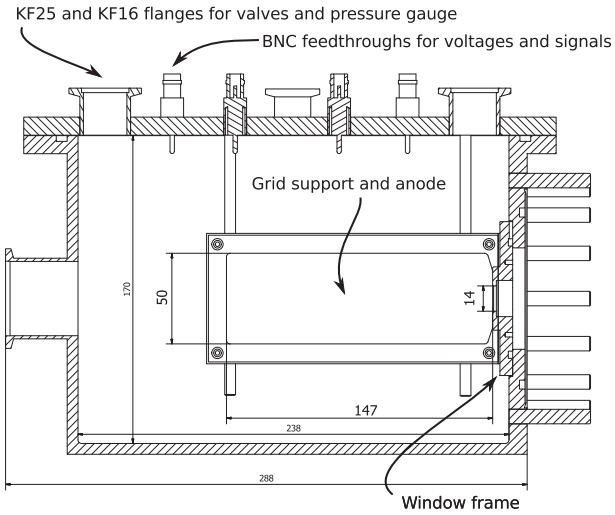

Fig. 1. Cross section of the chamber of the gas ionization detector. The particles enter from the right.

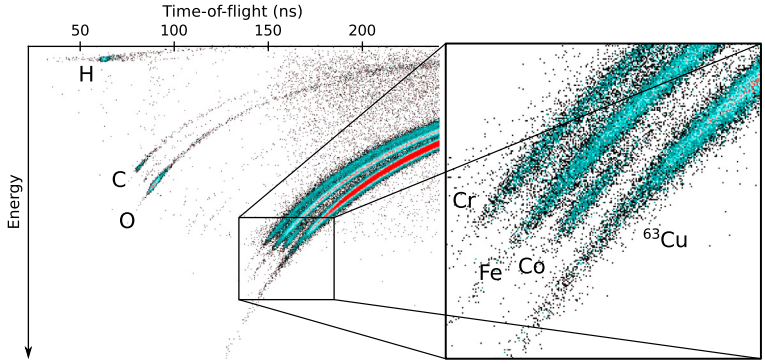

Fig. 2. ToF–E histogram of thin Co_3O_4 film on steel measured with 11.9 MeV ^{63}Cu beam. The scattered incident beam can be resolved from Co and Fe of the substrate.

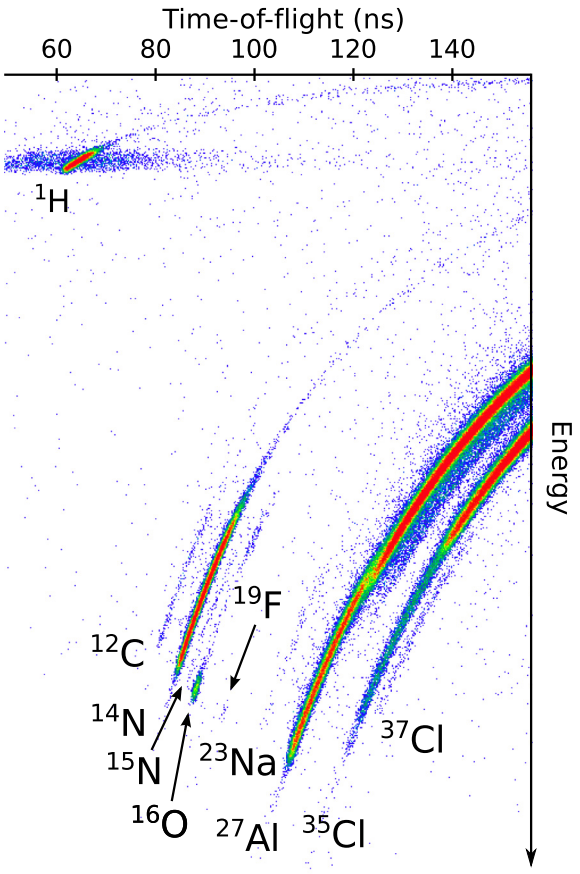

Fig. 3. ToF–E histogram of 80 nm film of AlN on Si measured with 8.5 MeV ^{35}Cl. The ^{37}Cl originating from a chlorine impurity in the sample is clearly resolved from the scattered beam.

and had these samples been measured before the detector upgrade the trace content of chlorine might have gone unnoticed using the typical ^{35}Cl beam.

Mechanical vibrations caused by mechanical and turbomolecular pumps and other equipment have been determined to be the dominant source of <1 kHz noise in the detector signals. Microphonics and demodulated EM pickup have also earlier been reported to have a major contribution to the electronics noise [10]. High frequency EM pickup especially from switching power supplies carried by power connections and bias voltage cables overlaps the signal band. The approximately 300 ns rise time of GIC signals implies that noise near 1 MHz frequency may limit the use of the signal for timing purposes.

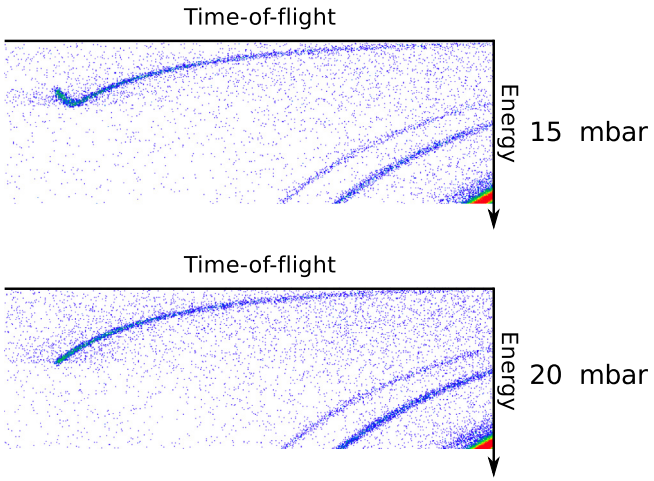

Fig. 4. Portion of a ToF–E histogram showing the full energy detection of hydrogen at 20 mbar, and the same measurement at 15 mbar. With the 8.5 MeV incident ^{35}Cl beam the hydrogen recoils from surface have 530 keV of energy. Detection of hydrogen is possible at both pressures, but 20 mbar gives better rejection of background. Most of the background is due to the measurement being long (60 min), the hydrogen concentration is approximately 1 at.%.

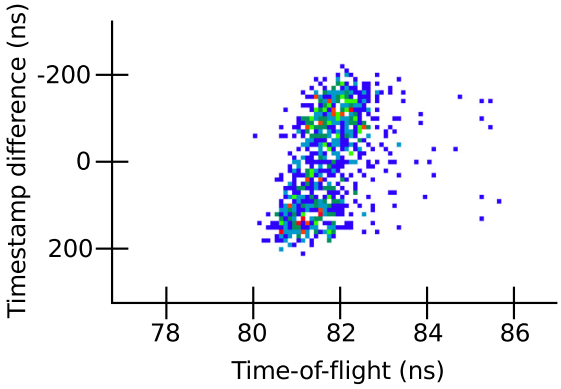

Fig. 5. 2D histogram of time-of-flight and time-of-flight–energy event timestamp difference of ^{16}O recoils from a 10 nm Al_2O_3 thin film. The timestamp difference is relative to the center of the coincidence window. The timestamp difference can be used as a measurement of the recoil angle. The time-of-flight of the recoils correlates with the timestamp difference, since the recoils to a smaller angle receive more energy and therefore have a shorter time-of-flight.

A gas ionization chamber can only collect the full ionization and make a proportional measurement of the energy of the incident particle if the particle is stopped in the active volume. In the

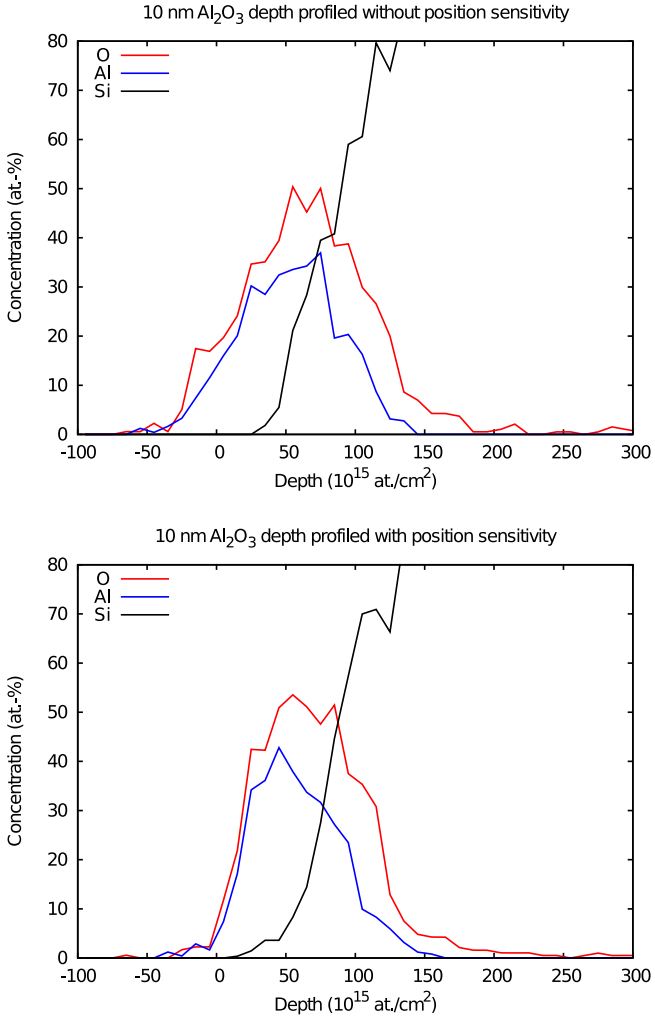

Fig. 6. Depth profiles of 10 nm Al_2O_3 film on Si analysed using the same data and depth profiling code, both with and without (above) position sensitivity. There are 966 counts from recoiled oxygen and 812 counts of aluminium in the measurement, which explains the large statistical fluctuation.

specific case of ToF-ERD this is not an absolute requirement, as long as the species can still be identified. For lighter beams at these energies the hydrogen recoils from the sample surface will always have the longest range in the gas. The range is however quite near the range of other light elements, making the use of a separate SSD at the end of the detector for hydrogen detection both inconvenient and unnecessary.

Full ionization of 600 keV hydrogen recoils with the 14×14 mm^2 window can be measured with 20 mbar of pressure, while lowest detectable energy for hydrogen is well below 100 keV. Fig. 4 shows how hydrogen detection is possible even with lower pressure. In this case only a portion of the energy of the recoils is measured, but since there is no overlap in the 2D histogram species identification is possible.

In Fig. 5 the TOF and E timestamp difference and the time-of-flight of oxygen recoils is presented as a 2D histogram. The linear dependence of the timestamp difference to the position is evident when looking at the front edge of the time-of-flight coordinate. This position sensitivity in depth profiling can directly be used for example with a slab-analysis code [11], which calculates the depth profile iteratively without a priori information of the composition. The initial depth profile is assumed to be uniform with equal amount of each element that is being computed. The code starts with this initial elemental depth profile and then by applying stopping force and known kinematics calculates the depth from which each observed recoil originates. Weighing these recoils by the cross sections the code forms a new estimate for the depth profile. Typically the final depth profile converges in three to four iterations.

In these codes multiple scattering is neglected, so the position measurement is directly used in the calculation of the recoil angle and effective depth of recoil. The improvement in resolution by having a position sensitive detector using this approach is significant near the few top nanometres of the sample. In Fig. 6 the depth profile of a 10 nm Al_2O_3 ALD film has been extracted from the same data, either using the position coordinate or fixing it to give a constant recoil angle. The improvement in the depth resolution due to kinematic correction is clear, and this approach pushes the resolution of the technique towards 1 nm in standard measurements, without the need of extreme sample tilting.

4. Conclusions

The gas ionization chamber built provides simultaneously good energy resolution for heavy recoils and detection of low energy hydrogen recoils. The resolution combined with a large solid angle makes the ToF-ERD setup versatile tool for thin film research.

Position sensitivity by timing of the anode pulses allows kinematic correction especially if digitizing data acquisition is used with very little added complexity. Similar timing resolution is also possible using a timestamped list-mode data acquisition and conventional ADCs. The position sensitivity is achieved with no cost to the energy resolution.

Acknowledgements

This work was supported by the Finnish Funding Agency for Technology and Innovation Tekes EU regional funds project HIUDAKE and Academy of Finland Center of Excellence in Nuclear and Accelerator Based Physics (Ref. 251353).

References

[1] G.F. Knoll, Radiation Detection and Measurement, Wiley, 2010.
[2] M. Döbeli, C. Kottler, M. Stocker, S. Weinmann, H.-A. Synal, M. Grajcar, M. Suter, Nucl. Instr. Meth. Phys. Res., B 219–220 (2004) 415.
[3] C. Kottler, M. Döbeli, F. Glaus, M. Suter, Nucl. Instr. Meth. Phys. Res., B 248 (2006) 155.
[4] T.D.M. Weijers, H. Timmers, R.G. Elliman, Nucl. Instr. Meth. Phys. Res., B 190 (2002) 397.
[5] F. Busch, W. Pfeffer, B. Kohlmeyer, D. Schüll, F. Pühlhoffer, Nucl. Instr. Meth. 171 (1980) 71.
[6] W. Bohne, J. Röhrich, G. Röschert, Nucl. Instr. Meth. Phys. Res., B 139 (1998) 219.
[7] W. Assmann, Nucl. Instr. Meth. Phys. Res., B 64 (1992) 267.
[8] M. Laitinen, T. Sajavaara, M. Rossi, J. Julin, R.L. Puurunen, T. Suni, T. Ishida, H. Fujita, K. Arstila, B. Brijs, H.J. Whitlow, Nucl. Instr. Meth. Phys. Res., B 269 (2011) 3021.
[9] O. Bunemann, T.E. Cranshaw, J.A. Harvey, Can. J. Res. 27 (1949) 191.
[10] A. Göpfert, F.-J. Hambsch, H. Bax, Nucl. Instr. Meth. Phys. Res., A 441 (2000) 438.
[11] K. Arstila, Personal Commun.

PII

DIGITIZING DATA ACQUISITION AND TIME-OF-FLIGHT PULSE PROCESSING FOR TOF-ERDA

by

Jaakko Julin, Timo Sajavaara

Nuclear Instruments and Methods in Physics Research Section B: Beam Interactions with Materials and Atoms 366 (2016) 179–183

Nuclear Instruments and Methods in Physics Research B 366 (2016) 179–183

Contents lists available at ScienceDirect

Nuclear Instruments and Methods in Physics Research B

journal homepage: www.elsevier.com/locate/nimb

Digitizing data acquisition and time-of-flight pulse processing for ToF-ERDA

Jaakko Julin *, Timo Sajavaara

University of Jyvaskyla, Department of Physics, P.O. Box 35, FI-40014 University of Jyvaskyla, Finland

ARTICLE INFO

Article history:
Received 17 September 2015
Accepted 27 October 2015
Available online 14 November 2015

Keywords:
Ion beam analysis
Digitizer
ToF-ERDA
Time-of-flight
Data acquisition

ABSTRACT

A versatile system to capture and analyze signals from multi channel plate (MCP) based time-of-flight detectors and ionization based energy detectors such as silicon diodes and gas ionization chambers (GIC) is introduced. The system is based on commercial digitizers and custom software. It forms a part of a ToF-ERDA spectrometer, which has to be able to detect recoil atoms of many different species and energies. Compared to the currently used analogue electronics the digitizing system provides comparable time-of-flight resolution and improved hydrogen detection efficiency, while allowing the operation of the spectrometer be studied and optimized after the measurement. The hardware, data acquisition software and digital pulse processing algorithms to suit this application are described in detail.

1. Introduction

The data acquisition in ion beam analysis (IBA) techniques such as Rutherford backscattering spectrometry (RBS) and elastic recoil detection analysis (ERDA) almost always relies on analogue signal processing and multi channel analyzer (MCA). This is often sufficient, since the resolution needs and count rate capabilities can in most cases be met by standard nuclear instrumentation module (NIM) based electronics.

Digital pulse shaping is a well-established field and for example trapezoidal shaping [1] is a useful technique to extract high resolution pulse height information even at high count rates, originally developed for gamma ray spectroscopy. Commercial silicon drift detector (SDD) with integrated trapezoidal pulse shaper is often used in high count rate X-ray detection also in the world of IBA. In an RBS setup a digitizer with a trapezoidal shaper implemented using a field programmable gate array (FPGA) is a clear replacement for the traditional shaping amplifier MCA combination.

A unique challenge among ion beam analysis techniques is ToF-ERDA, where the time-of-flight measurement from two multi-channel plate (MCP) pulses is usually based on a discriminator such as a CFD, followed by a time-to-amplitude converter (TAC) or a time-to-digital converter (TDC). Coincidences between the time-of-flight and energy detectors are either found using timestamps [2] or a hardware coincidence box. By using list-mode data acquisition beam-induced changes to the sample can be detected. The count rate of timing detectors is ultimately limited by the recharging of the MCPs [3]. The count rate is kept usually much lower than that, typically less than 20,000 counts per second (cps), in order to reduce background due to multiple particles in the same TDC window. The width of a TDC timing window needs to be roughly 200–500 ns, depending on the incident beam, to detect low energy heavy recoils.

Gas ionization chambers (GIC) with thin entrance windows are used in increasing numbers in ToF-ERDA spectrometers as the energy detector [4,5]. In order to exploit the capabilities of even a simple planar electrode GIC, signals should be captured also from other electrodes than the anode, and advanced pulse shaping methods used to analyze those signals. Build up of charge in the gas and pile-up limit the count rate of the detector to typically 1000 (cps).

The abovementioned count rates do not present a challenge to a digitizing system, even when full traces are captured from the MCP detectors and an energy detector. The data rate is typically some megabytes to tens of megabytes per second and therefore it is possible to do the signal processing on a standard PC, which makes it easy to modify the processing to suit the needs of the particular setup with only software modifications. After the experimental setup has been set and MCP traces have been captured, it is possible to fine-tune the timing analysis offline. Digitizing the detector signals is also valuable for the development of the detectors, as the signals can be studied in detail after a measurement.

* Corresponding author.
E-mail address: jaakko.julin@jyu.fi (J. Julin).

http://dx.doi.org/10.1016/j.nimb.2015.10.066
0168-583X/

Digital timing for positron emission tomography and nuclear physics experiments using multiple scintillation detectors is already established [6,7]. Digitizers have also been used successfully in extracting high-resolution timing information from silicon detectors [8]. The large number of channels in some of these experiments necessitates pulse processing in hardware, either on an FPGA or an application specific integrated circuit (ASIC). In contrast software based real-time analysis has been applied in positron lifetime spectrometers [9]. The task of measuring time intervals with 200 ps resolution and kHz count rates is similar to ToF-ERDA. Especially signals from MCP-PMTs are comparable in shape to the MCP signals studied in this paper, but the variance in pulse amplitudes is typically smaller in photo detectors than in carbon foil based timing detectors used in ERDA. The instrumentation described in this paper has also been used to study scintillator detectors by reading out signals from both traditional photomultiplier tubes (PMT) and silicon photomultipliers (SiPM), the results are unpublished.

In IBA where the number of acquisition channels is small, usually between one to four, a commercial digitizer with proprietary FPGA firmware is a cost effective choice, the hardware itself is inexpensive and there is no need to invest time on digitizer hardware development or FPGA programming. The digitizing ToF-ERDA system developed in Jyväskylä is described in this paper, including discussion on the limitations of this approach to data acquisition.

2. Experimental

The experimental setup consists of the ToF-ERDA spectrometer installed at the +15 degree beamline at the JYFL 1.7 MV Pelletron accelerator. The ToF-ERDA spectrometer consists of two carbon foil timing detectors [10] T1 and T2 for the start and stop signals, respectively, and a gas ionization chamber [5].

The digitizing data acquisition comprises two digitizers, a CAEN S.p.A. N6751 2/4 channel 2/1 GSample/s 10-bit digitizer, which digitizes pulses with 1 Vp-p scale and adjustable ±0.5 V DC offset and a CAEN N6724 4 channel 100 MSample/s 14-bit digitizer, 2.25 Vp-p input scale. The input impedance in both digitizers is 50 ohm. The setup is shown schematically in Fig. 1. The N6751 is used to digitize fast MCP signals in two-channel mode at 2 GS/s and N6724 with the CAEN DPP-PHA is used to digitize GIC and Si detector signals after they have been amplified by a charge sensitive preamplifier (Amptek CoolFET). The DPP-PHA firmware runs in real time both a trigger and a trapezoidal shapers. This makes it possible to capture energy signals using list-mode at high count rates and more importantly for each channel to self trigger, minimizing the dead time.

The faster digitizer uses the standard firmware provided by the manufacturer, which implements only a leading edge trigger and returns full traces of all active channels on trigger. With this firmware the digitizer is effectively a digital storage oscilloscope. The digitizers are synced using an external clock generator (AD9548) and a daisy-chained start signal with the GPO/GPI connectors on the digitizers. This allows events to be correlated within the 20 ns (N6751) and 16 ns (N6724) timestamp jitter.

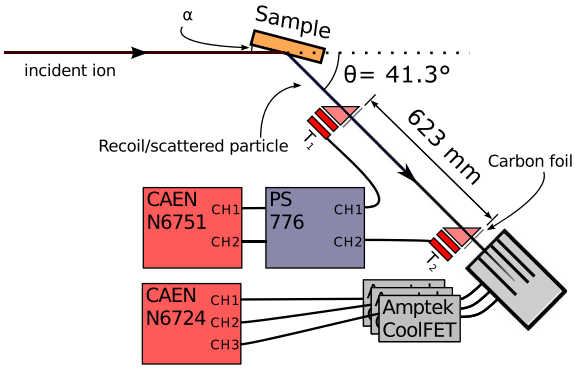

Fig. 1. ERD geometry and signal paths.

In a time-of-flight measurement the trace length defines the width of the timing window. One advantage of the digitizers is the possibility to return samples also before the trigger, as the digitized signal is continuously saved to a buffer. The triggering time-of-flight gate in ToF-ERDA can therefore be the T2 without the use of delay boxes, and the advantage of smaller background count rate and on average higher pulse heights of the T2 can be exploited. In this approach there are no triggering criteria on T1, compared to digitizing the signals from the gates independently. When the trace has been captured, the digitizer continues saving the ADC samples to another buffer and ignores any triggers until this buffer is filled and a full trace can be returned on the next trigger. Therefore the trace length also defines the dead time. By allowing the digitizer to capture variable-length events the dead time could be eliminated entirely, but the reconstruction of events would be complicated.

The digitizers are connected by a CAEN optical link to a two channel PCI-Express card (CAEN A3818). Up to eight digitizers can be connected in a daisy chain to one channel with a maximum of 80 MByte/s data rate. The card is installed to a desktop computer with a quad core processor running Linux operating system.

Since the trigger logic of the N6751 operates at 125 MHz the local trigger can only be used for pulses exceeding the threshold for 8 sampling periods. This limitation exists in the firmware provided by the digitizer manufacturer, since using parallelization techniques it is possible to trigger to a leading edge in just one sample [11]. In the ToF-ERDA application short MCP pulses barely above the noise level are observed from hydrogen recoils, and not all of these trigger the local trigger. Alternatively an external trigger can be used, for example from a CFD, in which case the detection efficiency can be as good as with an analogue setup. In this study the MCP signals are amplified by a 300 MHz amplifier (Phillips Scientific 776), and then digitized. The amplification (10×) must be this large for the T1 signals, as hydrogen signals below 10 mV are observed even after the amplification. For T2 the signals are attenuated by a factor of two using resistors after the amplifier, since the signals are stronger due to a thicker carbon foil [12], which emits on average more electrons. The root-mean-square (RMS) noise measured from the digitized signal from T1 is 0.7 least significant bits (LSB), approximately the same in millivolts, and 0.8 LSB from the T2, these figures include both the contribution of the quantization and detector noise. Adjusting the voltage over the MCP plates allows the gain of the MCP to be fine-tuned to match the digitizer dynamic range. Fig. 2 shows typical pulses from the timing detectors as captured by the digitizer.

3. Data acquisition

3.1. Software

The data acquisition software is homemade Linux software equipped with a graphical user interface (GUI) built using the Qt5 framework [13]. Digitizer and pulse analysis specific code does not use any Qt5 code, but is instead implemented using C++ standard library, Boost C++ libraries [14], GNU scientific library [15], CAEN digitizer library, and POSIX threads. This makes it possible to reuse the code if a non-GUI version of the software is preferred.

The software is designed to run processing tasks in parallel as much as possible, since modern PCs are equipped with multi-core processors. Each digitizer connection is handled in a separate

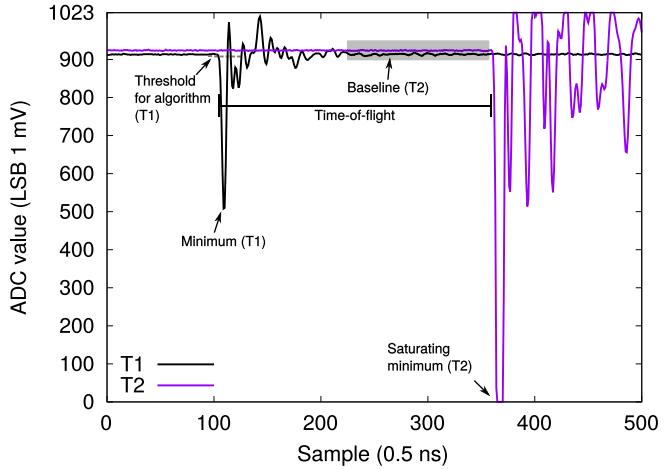

Fig. 2. Typical T1 and T2 pulses from a single particle are plotted as digitized. Note the saturating T2 pulse.

thread, and any output file saved from the data queues is handled by a data saving thread. Signal processing can be done by a user-supplied number of analyzer threads. In a two-digitizer scenario there are at least six threads running during the data acquisition.

The data read by a digitizer thread is pushed immediately to an acquisition event FIFO queue, implemented using C++ std::queue containers. The threads poll for new data as soon as the previously read events are passed to the acquisition queue. The producer–consumer problem in the queues is handled using condition variables. The raw events can be dumped to a file in a custom ASCII format, binary format or as gzip compressed binary by a saver thread. The purpose of a single saver thread is to store all data in a single file and keep coincident events as close as possible to each other. The offline analysis of raw data is simplified compared to saving events to separate files for every digitizer.

After the events have been saved they are passed on to another queue. The events from the queue are read by the analyzer threads, which run the events through any number of preconfigured analysis algorithms. The implemented algorithms are described in more detail in Section 3.2. The analyzer threads are all identical, as on the start of the acquisition these threads are launched with clones of the analyzers configured in the user interface. The different analyzers implement a common C++ class for interfacing. Each of the analyzers provide a concise numeric value, and all the values are gathered to a single file in the same fashion as the raw events. Finally the list events are passed to a coincidence processor. The data flow is shown schematically in Fig. 3. In practice it is not always necessary nor convenient to store the full traces, so the software has been designed to be fast enough to do all signal processing on-line. Storing full traces may also limit the achieved count rate, if the mass storage is not fast enough.

Due to the large number of queues storing potentially a large number of events, there must be a careful balance between the

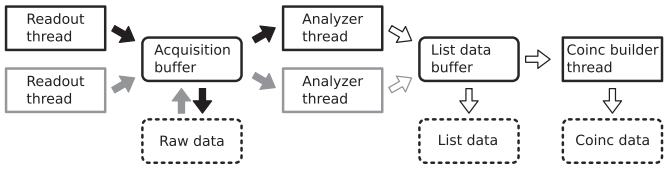

Fig. 3. A simplified block diagram of the software processing data flow. Any number of readout threads can be combined with any number of pulse analysis threads. Raw data, list-mode data and coincidence list-data are saved to files by separate threads.

memory use and data loss. The size of the queues can be changed at run-time, but a maximum number of events in each queue has to be set, so the memory use does not increase unexpectedly. In addition to the acquisition program, small helper programs were also written which allow events to be extracted from the raw data and reanalyzed.

3.2. Signal processing for MCP pulses

The timing algorithm that was found to work well for the MCP pulses is based on a digital implementation of the analogue CFD method. The figure of merit for a timing algorithm is not only the timing resolution, but also a stable threshold for small pulses that determines the hydrogen detection efficiency. An external trigger based on the T2 signal is used to capture the data, therefore the T2 detection efficiency is limited by the trigger. The algorithm uses a simple level threshold and a variable window averaging before the pulse exceeds the threshold to determine the rough location of a pulse and the baseline before it, see Fig. 2. Only the samples near this trigger point are then considered for detailed timing analysis.

Sub-sample resolution requires interpolation at some stage. In order to preserve the high-frequency signal an interpolation method producing a continuous reconstructed signal, preserving the original samples exactly, and only being sensitive to nearest few samples was preferred. According to sampling theorem a perfect reconstruction for band-limited signals exists, and this reconstruction could be used to interpolate the original samples using a formula given by Shannon [16]. In this case the saturation of the ADC can severely limit the applicability of this method, and the computational cost of this ideal sinc filter is too high. A more practical windowed sinc filter called a Lanczos filter [17] was implemented and tested using five weights. As a downside the Lanczos filter shows some oscillatory behavior on step changes. Piecewise polynomials, splines, were implemented with both 1st order (linear) and 3rd order (cubic) polynomials. Both the Lanczos filter and cubic splines also produce a reconstructed signal with continuous derivative. The results in this paper are achieved with the use of cubic spline interpolation, unless otherwise noted.

After the baseline has been subtracted the algorithm sums the original pulse $V(t)$ with an inverted, attenuated (attenuation factor f) and time delayed (delay t_d) version of itself. This computed waveform is plotted in Fig. 4. The algorithm seeks the zero crossing $V(t) - f \cdot V(t - t_d) = 0$ first approaching this point stepwise and

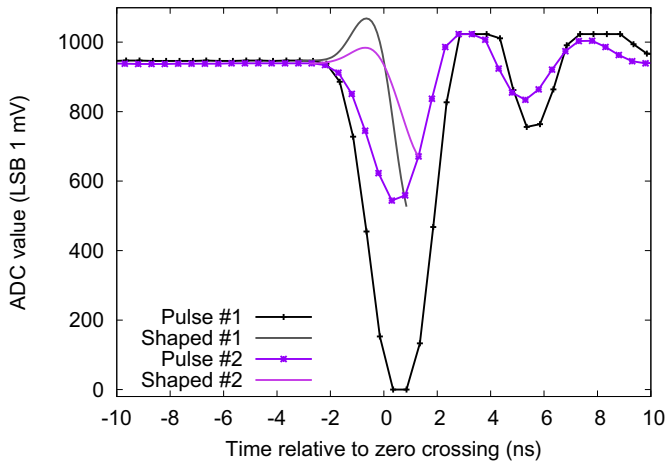

Fig. 4. Two T2 pulses processed with the amplitude and risetime compensated (ARC) timing algorithm using parameters $t_d = 1.5$, $f = 0.5$. The DC-level has been restored to the shaped pulse for the plot.

finally using Newton's method with a fixed number of iterations. The algorithm is very robust and anyone used to analogue CFD modules will find it relatively easy to tune. The algorithm can optionally compensate for the input signal saturation by extrapolating the leading edge linearly from the last two samples before the clipping occurs. Using a value for the delay t_d that is shorter than the pulse rise time to saturation will yield the best resolution, as then the algorithm works in the amplitude and risetime (ARC) compensated mode [18,19] However delay time below or near one sampling period might cause the timing to quantize to the sampling periods. For this reason pulse rise time from noise floor to saturation should always be at least two, preferably three sampling periods, depending on the f and choice of interpolation method. Even for analogue implementation the jitter increases for short t_d, while longer values introduce amplitude related walk [18].

The optimum f and t_d parameters for the ToF-ERDA setup were found by scattering 5.1 MeV ^{4}He ions from an evaporated 1 nm thick gold film on silicon. The resolution with our analogue pulse processing setup has been studied using similar method [10], since the resulting time-of-flight spectrum has a narrow peak. The He-particles at that energy produce both small pulses, resembling those of H recoils, but also stronger pulses like heavier recoils. The He particles at this energy can be detected by the GIC, but due to their long range they are not entirely stopped within the gas volume, and as such the GIC acts as a delta E detector. A silicon detector at the end of the active volume of the GIC has still enough resolving power to separate He scattered from the gold and silicon. This Si detector gating is important, since we can reduce the effect of the halos [12] from the lower energy He events overlapping in the time spectrum. The time-of-flight histogram is presented in Fig. 5. The same procedure but without the gating was performed also by scattering 6.8 MeV ^{12}C ions from the same film.

To study the effect of the MCP gain on timing resolution the measurements were repeated with different MCP voltages. During offline analysis only the pertinent events, i.e. only the few thousand events resulting from scattering from the thin film instead of hundreds of thousands events in total, were re-analyzed with varying parameter permutations. The energy loss in the gold film is negligible for the scattered He ions, but not for the C ions. Additionally the inhomogeneity of the gold film thickness might result in non-Gaussian ToF-distribution.

A Gaussian distribution was fitted to the peak automatically using Fityk [20]. In Fig. 6 the FWHM of the He resolution is plotted with varying T1 timing parameters. In Fig. 7 the C resolution is plotted with varying T2 timing parameters. The results confirm that the best resolution is found only when t_d is short enough to avoid issues with the ADC saturation (clipping). The pulses that have no zero crossing are discarded in these resolution plots. The efficiency of the algorithm must therefore be also investigated, since for any sensible values the threshold should limit the efficiency. Thus hydrogen detection efficiency must be calibrated every time the timing parameters are changed, but as long as the acquisition triggering conditions or the measurement setup are not changed the efficiency curve can be extracted from previously measured data. The hydrogen detection efficiency curves are plotted in Fig. 8. The final choice of threshold, t_d and f involves some compromise between efficiency, resolution and the stability of these two. It should be noted that sub-sampling rate resolution and high efficiency are achievable with most sane combinations. The resolution for all studied cases is well below the kinematic broadening for the recoils. This makes the tuning of the resolution only meaningful in practice if position sensitive detectors are used.

By discarding every other sample, effectively achieving 1 GS/s sampling rate, a sub-sample resolution was not achieved. With scattered helium, a time-of-flight resolution of 185 ps was achieved with 2 GS/s sampling rate using the full 10-bit samples. Degrading the vertical resolution by artificially zeroing the least 1, 2 or 3 bits the resolution degraded significantly, 196 ps, 217 ps and 314 ps respectively for the same data set. The minor difference between 10 and 9 bits vertical information can be explained by the presence of noise in the signals.

3.3. Signal processing for GIC pulses

CAEN DPP-PHA trapezoidal shaper is used online for the GIC/Si detector signals, but no direct software equivalent for this shaper is available. A trapezoidal shaper was therefore also implemented in software, in order to study the shaper parameters and GIC resolution offline.

The electronic noise contribution to the anode signal was measured with a precision pulse generator (BNC PB-5) connected to the test input of the anode preamplifier (Amptek CoolFET) during testing before GIC installation. The noise contribution for helium was determined to be 26 keV with an established calibration.

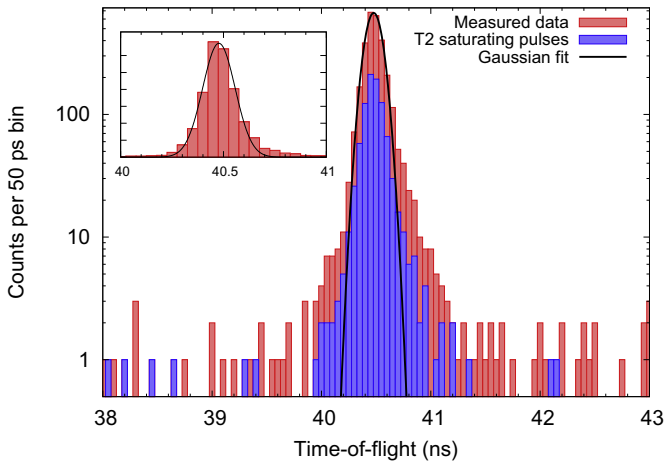

Fig. 5. Time-of-flight histogram of 5.1 MeV ^{4}He particles scattered from 1 nm thin Au film. The blue subset is from events producing ADC saturating pulses on T2. The FWHM of the fit is 185 ps. (For interpretation of the references to colour in this figure legend, the reader is referred to the web version of this article.)

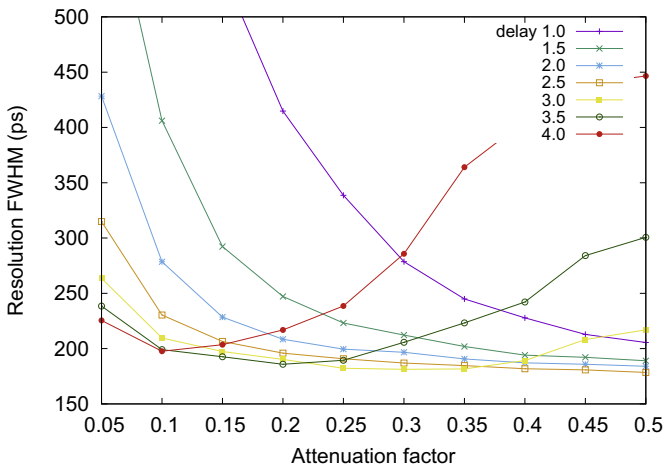

Fig. 6. Time-of-flight resolution for He, with varying T1 timing parameters f and t_d. The delay parameter t_d is expressed in sampling periods (0.5 ns). T2 parameters were kept constant.

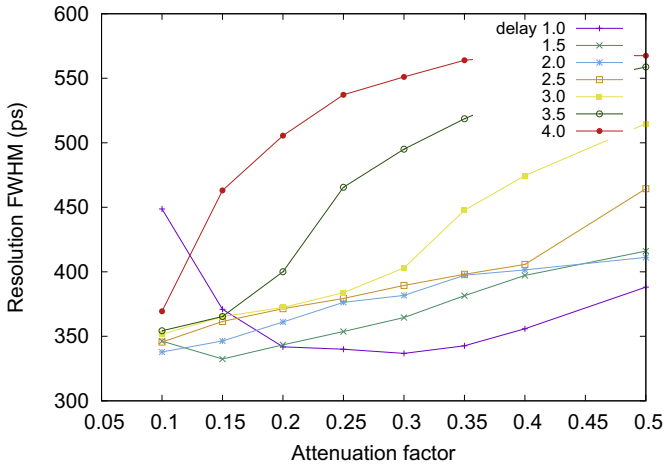

Fig. 7. Time-of-flight resolution for C, with varying T2 timing parameters. The T2 MCP voltage was −1700 V. The resolution is limited by the experimental conditions.

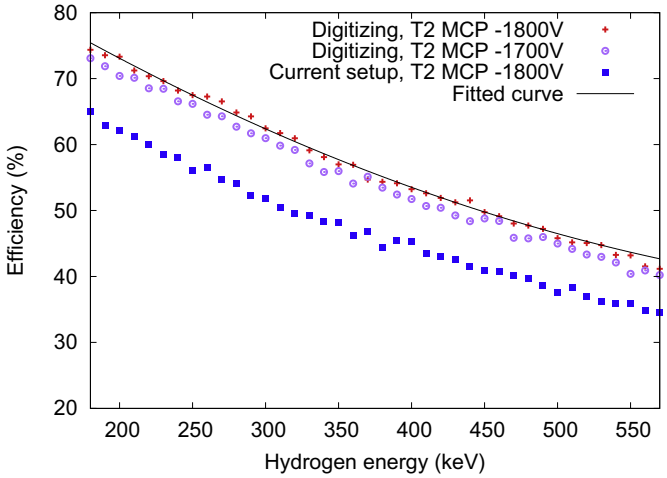

Fig. 8. Hydrogen detection efficiency for the current analogue setup and the digitizing setup with two T2 MCP voltages. The difference between the efficiency of the two setups is explained by different T1 detection efficiency. T2 efficiency is limited by the analogue CFD module, which produces the external trigger.

The digitized signal amplitude was increased by a factor of four by addition of a timing filter amplifier (TFA) to the front-end electronics. The signals from the GIC have plenty of low frequency noise associated with microphonic pickup, so the TFA was set to differentiate the signal with 100 μs time constant, acting as a high-pass filter. Without the differentiation the dynamic range of the digitizer would have not been sufficient. The shape of the pulses except for the tail remained virtually unaffected by the TFA, since the integration stage was turned off. The resolution improved noticeably for the smallest hydrogen and helium pulses, but the exact cause of this improvement is unclear. Both the low effective number of bits (ENOB) and integral nonlinearity (INL) of the digitizer were suspected, but could not be definitively attributed to be the source of poor performance. The measurements in this paper were performed without the TFA in the signal chain.

4. Conclusions

Since the MCP pulses are sampled at only 2 GS/s and many of the pulses are clipped even with 10 bits of vertical resolution, too fast pulses can create problems. At least two samples must be captured on the rising edge to be able to do sub sample period timing using the ARC method with the highest resolution.

Optimum timing parameters were found by studying a narrow peak with different particle species. Three different interpolation methods were tested using the best possible parameters for ARC timing and only minor differences in resolution were observed.

The system can achieve timing resolution comparable to an analogue setup. In our setup the T2 MCP gain was reduced to improve the timing resolution at the cost of slightly reduced hydrogen detection efficiency. The hydrogen detection efficiency is still noticeably higher than with our analogue setup.

Due to the versatility of the digitizing setup and its cost effectiveness it is expected that many analogue setups in ToF-ERDA will eventually be replaced by a digitizer based solution. The software-based signal processing presented here reduces the time spent on the tuning of the setup. Many of the hardware limitations and problems encountered with commercial digitizers are mitigated as the hardware and firmware continue to develop.

Acknowledgements

This work was supported by the Finnish Funding Agency for Technology and Innovation Tekes through EU regional funds project HIUDAKE and Academy of Finland Center of Excellence in Nuclear and Accelerator Based Physics (Ref. 251353).

References

[1] V.T. Jordanov, G.F. Knoll, Digital synthesis of pulse shapes in real time for high resolution radiation spectroscopy, Nucl. Instr. Meth. A 345 (1994) 337.
[2] M. Rossi, P. Rahkila, H. Kettunen, M. Laitinen, A simple timestamping data acquisition system for ToF-ERDA, Nucl. Instr. Meth. B 347 (2015) 39.
[3] A. Tremsin, J. Pearson, G. Fraser, W. Feller, P. White, Microchannel plate operation at high count rates: new results, Nucl. Instr. Meth. A 379 (1996) 139.
[4] C. Kottler, M. Döbeli, F. Glaus, M. Suter, A spectrometer for low energy heavy ion ERDA, Nucl. Instr. Meth. B 248 (2006) 155.
[5] J. Julin, M. Laitinen, T. Sajavaara, Time-of-flight ERD with a 200 mm^2 Si_3N_4 window gas ionization chamber energy detector, Nucl. Instr. Meth. B 332 (2014) 271.
[6] P. Guerra, J.E. Ortuno, G. Kontaxakis, M.J. Ledesma-Carbayo, J.J. Vaquero, M. Desco, A. Santos, Real-time digital timing in positron emission tomography, IEEE T. Nucl. Sci. 55 (2008) 2531.
[7] A. Fallu-Labruyere, H. Tan, W. Hennig, W. Warburton, Time resolution studies using digital constant fraction discrimination, Nucl. Instr. Meth. A 579 (2007) 247.
[8] L. Bardelli, G. Poggi, M. Bini, G. Pasquali, N. Taccetti, Time measurements by means of digital sampling techniques: a study case of 100 ps FWHM time resolution with a 100 MSample/s, 12 bit digitizer, Nucl. Instr. Meth. A 521 (2004) 480.
[9] J. Nissilä, K. Rytsölä, R. Aavikko, A. Laakso, K. Saarinen, P. Hautojärvi, Performance analysis of a digital positron lifetime spectrometer, Nucl. Instr. Meth. A 538 (2005) 778.
[10] M. Laitinen, M. Rossi, J. Julin, T. Sajavaara, Time-of-flight – energy spectrometer for elemental depth profiling – Jyväskylä design, Nucl. Instr. Meth. B 337 (2014) 55.
[11] A.M. Fernandes, R.C. Pereira, J. Sousa, A. Neto, P. Carvalho, A.J.N. Batista, B.B. Carvalho, C.A.F. Varandas, M. Tardocchi, G. Gorini, J.-E. Contributors, Parallel processing method for high-speed real time digital pulse processing for gamma-ray spectroscopy, Fusion Eng. Des. 85 (2010) 308.
[12] M. Laitinen, M. Rossi, J. Julin, T. Sajavaara, Secondary electron flight times and tracks in the carbon foil time pick-up detector, Nucl. Instr. Meth. B 336 (2014) 55.
[13] Qt application framework, http://www.qt.io/.
[14] Boost C++ libraries, http://www.boost.org/.
[15] GSL - GNU Scientific Library, http://www.gnu.org/software/gsl/.
[16] C.E. Shannon, Communication in the presence of noise, Proc. IRE 37 (1949) 10.
[17] C.E. Duchon, Lanczos filtering in one and two dimensions, J. Appl. Meteorol. 18 (1979) 1016–1022.
[18] R.L. Chase, Pulse timing system for use with gamma rays on Ge (Li) detectors, Rev. Sci. Instr. 39 (1968) 1318.
[19] Z.H. Cho, R.L. Chase, Improved amplitude and rise time compensated timing with Ge detectors, IEEE Trans. Nucl. Sci. 19 (1972) 451.
[20] M. Wojdyr, Fityk: a general-purpose peak fitting program, J. Appl. Crystallogr. 43 (2010) 1126.

PIII

SIMULATIONS ON TIME-OF-FLIGHT ERDA SPECTROMETER PERFORMANCE

by

Jaakko Julin, Kai Arstila, Timo Sajavaara

Review of Scientific Instruments 87 (2016) 083309

REVIEW OF SCIENTIFIC INSTRUMENTS **87**, 083309 (2016)

Simulations on time-of-flight ERDA spectrometer performance

Jaakko Julin,[a] Kai Arstila, and Timo Sajavaara
Department of Physics, University of Jyväskylä, P.O. Box 35, FI-40014 Jyväskylä, Finland

(Received 11 May 2016; accepted 12 August 2016; published online 30 August 2016)

The performance of a time-of-flight spectrometer consisting of two timing detectors and an ionization chamber energy detector has been studied using Monte Carlo simulations for the recoil creation and ion transport in the sample and detectors. The ionization chamber pulses have been calculated using Shockley-Ramo theorem and the pulse processing of a digitizing data acquisition setup has been modeled. Complete time-of-flight–energy histograms were simulated under realistic experimental conditions. The simulations were used to study instrumentation related effects in coincidence timing and position sensitivity, such as background in time-of-flight–energy histograms. Corresponding measurements were made and simulated results are compared with data collected using the digitizing setup. *Published by AIP Publishing.* [http://dx.doi.org/10.1063/1.4961577]

I. INTRODUCTION

In time-of-flight elastic recoil detection analysis (TOF-ERDA) atoms recoiling from samples are detected using timing detectors and an energy detector, typically either a silicon detector or a gas ionization chamber (GIC). The purpose of the energy detector is to enable mass separation of the recoils. Many of the spectrometers built in the past 15 years utilize heavy ion beams with energy around 10 MeV[1–4] and are used in the light element analysis of 10 nm–300 nm thick films. Quite often the factors limiting the sensitivity are counting statistics and sample damage during the ion bombardment[5,6] rather than background, which has therefore remained largely unstudied. Time-of-flight ERDA has a low background, which is a result of the nature of coincidence measurements.

Gas ionization chambers are used in ToF-ERDA[2,7,8] due to their insensitivity to radiation damage and better resolution for heavy recoils compared to solid state detectors. The increasing use of GICs in this application has raised questions on their count rate and low energy performance, as well as position sensitivity.

Planar electrode gridded gas ionization chambers are inherently position sensitive in the direction perpendicular to the electrodes. The anode signal should be insensitive to position, giving a signal proportional to total electron charge while the cathode signal is proportional to both the total ionization and position. Position sensitivity can be achieved by comparing cathode and anode pulse heights, or by measuring the drift time of electrons to the Frisch grid.[9,10] Additionally, splitting one of the electrodes into sawtooth segments can be used to achieve position sensitivity in the perpendicular direction.[10,11]

The Frisch grid shielding inefficiency and its influence to detector resolution have been studied previously.[12] The inefficiency is influenced by the aberrations of the electric field near the entrance window, making the contribution of the inefficiency to the anode signal recoil range dependent. These window effects also influence position resolution.

Using digitizers it is possible to capture different signals from a GIC and effects related to electron transport in the gas and the Frisch grid are open to study. See Fig. 1 for an example of cathode, grid, and anode pulses captured from a GIC.

A Monte Carlo (MC) simulation code MCERD[13] has been developed to reproduce experimental ERDA energy spectra. Effects including the beam spot size, multiple and plural scattering, and scattering in the detector foils are taken into account. The use of this MC method for analysis has been validated.[14]

Here the MC simulation is further expanded to be useful in the study of a time-of-flight–energy telescope. The simulation codes developed in this study are aimed at studying the effects of the system as a whole, with the intent of simulating entire time-of-flight–energy histograms rather than some ions with fixed energy and recoiling angle from the target. The simulations enable the study of background due to count rate related issues such as false coincidences and pile-up in addition to effects related to energy detector response, e.g., position dependence and large angle scattering inside the gas ionization chamber.

Systematic studies related to detection limits of trace elements are difficult via direct measurements, since samples are damaged by ion bombardment and underlying effects may not be straightforward to quantify. Some of the background events are indistinguishable from proper events and therefore to get an estimate on their contribution simulations are necessary. Certain wrong coincidences can be detected and simulations can be used to reproduce these, providing additional evidence on the underlying background generating mechanisms.

II. SIMULATION SOFTWARE

A. MCERD

The existing ion transport and detector description in the code make it possible to simulate either ideal energy

[a]Electronic mail: jaakko.julin@jyu.fi

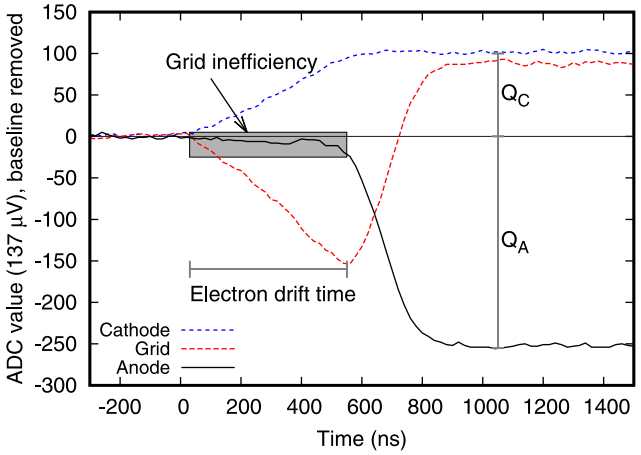

FIG. 1. Anode, Frisch grid, and cathode pulses as digitized by a CAEN N6724 digitizer from a parallel plate GIC. The grid shielding inefficiency and electron drift time to anode and collected charges can be extracted from these pulses.

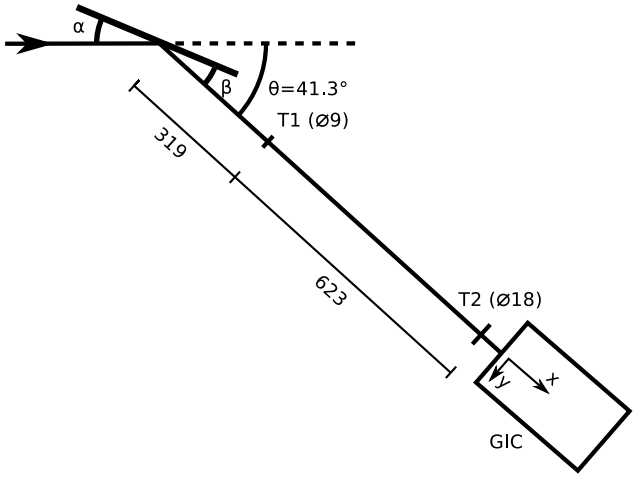

FIG. 2. The time-of-flight–energy spectrometer geometry used in the simulations. The xy-coordinates used in the gas ionization chamber simulations are marked inside the GIC. Mirror geometry ($\alpha = \beta \approx 20°$) was used. All dimensions are in mm. The diameter given for T1 and T2 corresponds to the last aperture of the detectors and the GIC entrance window is a 14 mm × 14 mm square.

detectors or time-of-flight detectors. For the purposes of this study, it was enough to describe the time-of-flight detector as foils followed by the entrance window and the gas volume of the ionization chamber. As the ions enter the ionization chamber, their energy, energy lost to collisions, position, and time are tabulated. These data are used in the following stage to simulate the energy detector response.

One major modification to MCERD was the inclusion of recoil cascades, as previously the simulation tracked only one recoiled atom from the sample at a time. In the modified code, sufficiently energetic recoils create more secondary recoils in the energy detector gas volume or in the entrance window. These secondary recoils are tracked and their movement is tabulated the same way as for the original recoil from the sample.

Additionally the program was made to output events that do not hit the ionization chamber, but pass through the first timing detector (T1) or the second timing detector (T2). This is possible if the solid angles of the detectors are different or due to large angle scattering in the carbon foils of the timing detectors. The SRIM 2013 code[15] was used as a source of electronic stopping data for various ions.

The geometry of simulated detectors and the beam spot are made to match the ToF-ERDA setup in Jyväskylä.[4] The flight distance is 623 mm and the detector angle is 41.3°. The beam spot size in the simulations was 2 mm by 3 mm, which creates a 6 mm by 3 mm beam spot projected on to the sample when the angle between the beam and sample normal is approximately 20°. See Fig. 2 for the geometry used in the simulations.

B. GIC response

The gas ionization chamber response is modeled using Shockley-Ramo theorem, which is commonly used to model a variety of radiation detectors which are based on moving charges.[16] The GIC simulation is intended to be simple and fast enough to simulate a large number of pulses in order to simulate entire measurements with hundreds of thousands of events each generating thousands or tens of thousands of electrons in the gas. The specific detector modeled here is described in Ref. 7.

The electric field and effective weighting potentials have been calculated in 2D using finite element method program FEMM 4.2.[17] The field between the electrodes was calculated in the xy plane perpendicular to the electrodes in xz plane. The electric potential $V(x, y)$ of the chamber is shown in Fig. 3. The calculated potentials and fields are sampled at 0.1 mm intervals in x and y directions, except near the Frisch grid, where the interval is 5 μm. The simulations use the tabulated data with bilinear interpolation.

Electrons are created along the path of the tracks of the ions, given by the MCERD calculated tracks. The production of electrons in the gas is based on the average energy loss per ion-pair produced, i.e., W values. There is no adequate theory or sufficient experimental data to approximate W, which has been shown to be mass, nuclear charge, and energy dependent for heavy ions.[18–20] The differences are explained by energy and ion dependence on the ratio of cross sections for ionization and excitation and transfer of kinetic energy into kinetic energy of gas molecules.[18]

For the purposes of this simulation, the response of several ions in isobutane was measured using beams scattered from a gold target. Time-of-flight measurement was used to determine the energy before the ionization chamber. The energy lost in the carbon foils and the entrance window was subtracted using SRIM 2013 stopping values. The average energy required to produce an ion pair was calculated from these measurements over a broad energy range. The results for ^{1}H, ^{4}He, ^{12}C, ^{16}O, ^{28}Si, and ^{63}Cu are plotted in Fig. 4. The measurements were also performed for ^{6,7}Li, ^{10,11}B, ^{27}Al, ^{29,30}Si, ^{35,37}Cl, ^{65}Cu, ^{79,81}Br, ^{127}I, and ^{197}Au. Differences between isotopes were within experimental error at similar velocities.

The preamplifier and pulse processing chain were calibrated by injecting a known charge $Q = CV$ into the input

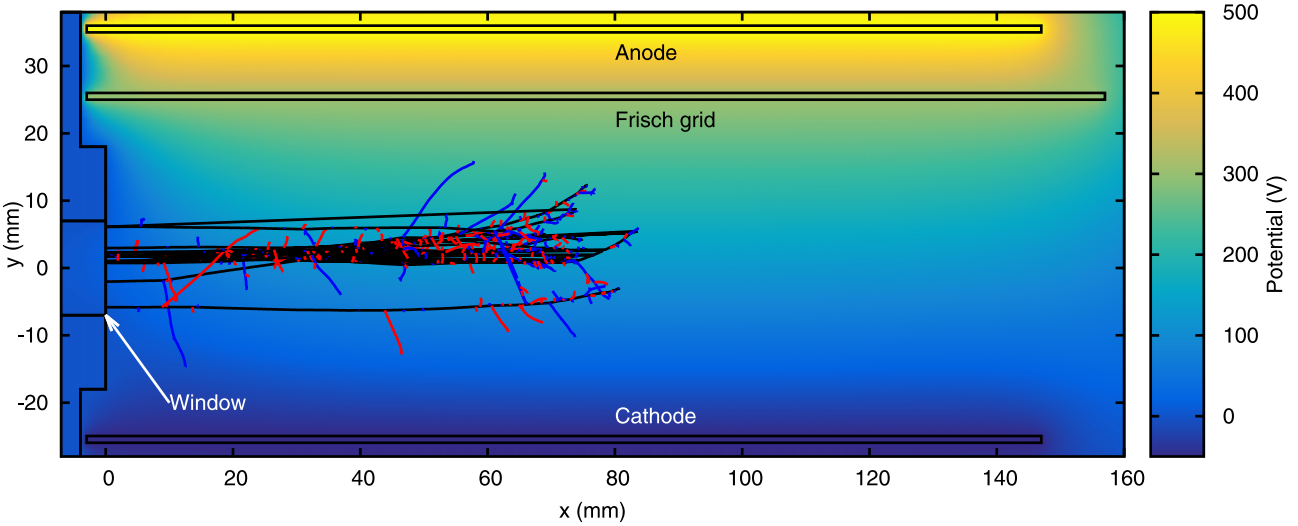

FIG. 3. Electric potential in the gas ionization chamber. The cathode, grid, and anode voltages are −50 V, 300 V, and 500 V, respectively. The primary recoils from the sample, 5 MeV–7 MeV titanium, are plotted in black. Tracks of recoiling hydrogen and carbon atoms of the detector gas are plotted in red and blue, respectively. The entrance window is located at $x = 0$ mm.

of the preamplifier with the help of a pulser and a 0.5 pF capacitor. The pulses were then processed using a digitizer. Using the obtained calibration factor, it is possible to calculate how much charge is collected by the anode. The goal was to obtain a relative calibration for all ions; therefore, the uncertainties associated with the test capacitor and pulser calibration are not considered. There are uncertainties associated with the treatment of stopping in the entrance window, time-of-flight to energy calibration, and fitting and smoothing of the data.

The response of isotopes or elements which are not measured can be estimated by interpolating the measured responses. The calibrations were extrapolated down to zero deposited energy. When the ion track is converted into an ionization track, the same W is assumed for not only the incident particle but also the subsequent recoils in cascades. This way the W will be the same in simulations and measurements, but fluctuations in the total ionization due to the recoils are not accounted for.

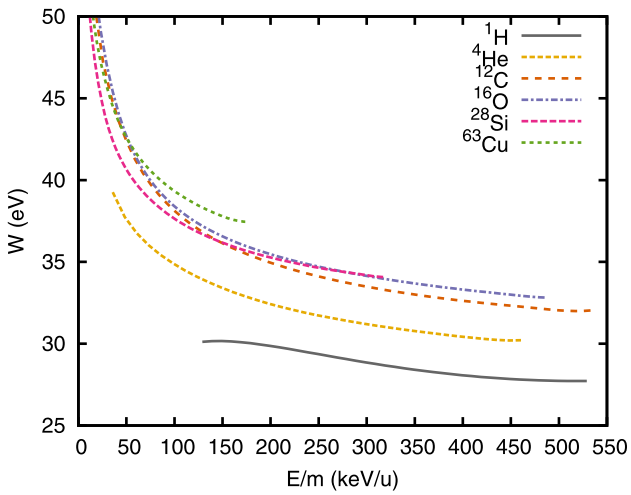

FIG. 4. Average energy required to produce an electron-ion pair for various ions in isobutane calculated from collected anode charge and energy determined from time-of-flight measurement are plotted. The results are presented for hydrogen, helium, carbon, oxygen, silicon, and copper ions. The results may be significantly affected by systematic uncertainties described in the text.

The number of electrons can be subjected to a fluctuation to account for Fano noise. The Fano factor[21] like W is not strictly constant for different heavy ions and different energies, but these data are not available in the literature and have not been measured by the authors either.

Slow tail caused by drifting ionized gas molecules is ignored, as the pulse of interest is determined primarily by the much faster moving electrons and the ion tail would be filtered out by pulse shaping. The anode is additionally shielded by the Frisch grid from the ion signal.

Electron transport in the gas is assumed to be collisional drifting motion along the electric field lines,

$$\frac{d\vec{x}}{dt} = -v_d(|E|)\hat{E}, \tag{1}$$

where E is the electric field and v_d is the drift velocity.

The drift velocity is given by Ref. 22. A simple diffusion model was implemented, where both transverse and longitudinal dispersion are given by

$$\sigma_x = \sqrt{\frac{2\epsilon_k}{eE}x}, \tag{2}$$

where x is the drift distance, ϵ_k is the characteristic energy at certain electric field, and e is the elementary charge. The values used here were also given by Ref. 22. The dispersion in each time step was close to numerical error. The simulations in this article were run without the dispersion model, since the contribution was negligible compared to variations in the initial distribution of electrons.

It should be noted that the electron transport used here does not account for any effects near the scale given by the mean free path of the electrons. This approximation holds elsewhere in the studied system except near the Frisch grid. The code does not allow electrons to be captured by the wires

of the Frisch grid. For more accurate models, the reader is referred to more advanced simulations, such as Garfield,[23] which can take into account many contributions ignored here, such as delta electrons, ion tail, and full 3D effects.

Without the dispersion and initial kinetic energy each electron is transported deterministically and the induced charge on any electrode can be determined from the (x, y) coordinates directly. The characteristic pulse $f(x, y, t)$ was precalculated for each (x, y, t) point with 0.5 mm and 2 ns spacing. The pulse can now be calculated rapidly as a sum over n electrons

$$V(t) = \sum_{i=0}^{n} f(x_i, y_i, t - t_i), \tag{3}$$

where (x_i, y_i, t_i) is the position where the electron was born.

C. Telescope simulation

This simulation models the detectors, data acquisition, and pulse processing of a digitizing setup.[24] The MCP signals from T1 and T2 timing detectors are digitized after amplification by a CAEN N6751 digitizer. The GIC anode and cathode signals are amplified with Amptek CoolFET preamplifiers and digitized using a CAEN N6724 digitizer. The pulse processing of the GIC signals is handled by the CAEN DPP-PHA processing on the FPGA, while time-of-flight signals are processed using software running on the computer reading out the digitizers.

1. Event generation

The events created by MCERD have a weight assigned to them, which is calculated from the distribution of the element in the sample and the cross section of the reaction. The telescope simulation builds a list of random events, in which the probability of event occurring is proportional to its weight. One MCERD-generated event can therefore appear in the output once or more or not at all. Calculating more events using MCERD will reduce the weight of an individual event in the telescope simulation. The time between events obeys Poisson statistics. The simulated count rate can be easily varied and so-called dark counts, i.e., events not originating from a recoil, can be injected into the stream of events with some predetermined count rate.

Individual events in the telescope simulation correspond to hits in the detectors. A list of hits in all detectors with picosecond time resolution is created. Energy detector hits have a unique identifier, which is used to couple the calculated electron pulse to the list of hits.

2. GIC pulse shaping

The ionization chamber pulses are simulated as described in Section II B.

Up to five ideal overlapping electron charge pulses are summed and converted into waveforms resembling digitized data by applying the gain of the preamplifier (0.64 μV/electron) and the digitizer gain (137 μV/LSB). The samples of the waveform have a 20 ns interval, which corresponds to the waveforms acquired from the N6724 digitizer when it is used in a mode where two consecutive samples captured at 100 MS/s sampling rate are averaged. Noise is added to the waveform to simulate the electronics noise, which was assumed to be white, although the actual measured noise spectrum is somewhat different. In particular, the real detector suffers from low frequency noise associated with vibrations and some intermittent higher frequency noise from external interference. The electronics noise of the studied system was measured with a pulser and white noise was added to simulated data so that after similar shaping the peak width is identical.

The preamplifier output rise time with typical detector capacitance 1 pF–100 pF is less than 20 ns, which is short compared to the 300 ns–500 ns current pulse from the ionization chamber and is also comparable to the 10 ns sampling interval used in the digitizing setup. The fall time RC constant is 500 μs, which is long enough to make any ballistic deficit minuscule. Preamplifier response is assumed to be ideal for these reasons.

The telescope simulation reproduces the operation of the trigger filter and pulse height filter of the CAEN digitizer. The trapezoidal pulse height filter used in the simulations is described by a recursive formula[25]

$$s(n) = s(n-1) + v(n) - v(n-k) - v(n-l) + v(n-l-k), \tag{4}$$

where $v(n)$ is the nth input sample and k is the rise time of the trapezoid and $l = k + m$, where m is the flat top duration of the filter. The time constants are expressed as a number of samples. The filter is similar to the trapezoidal filter used in the CAEN DPP-PHA firmware. In addition to the trapezoidal filter, a RC-CR^2-like trigger filter used by the firmware has been modeled. The trigger filter has a window average, here 32 samples or 640 ns and a double derivation using a delay, here 1 μs, long enough to account for the rise time of the input signal and the slower rise due to averaging. The signals from a GIC are noticeably slower than those of a silicon detector and have worse signal to noise ratio, making the averaging a necessity. With these parameters the trigger filter can capture the full pulse amplitude from real detector signals and trigger even 100 keV pulses. See Fig. 5 for examples of simulated pulses processed with the filters.

If two consecutive pulses can be separated by the trigger filter but not by the trapezoidal filter, either the latter pulse or both pulses can be rejected by the pile-up inspector. A properly adjusted trapezoidal filter is therefore immune to pile-up except for pulses within the trigger filter delay parameter (1 μs). There is also a rise time discriminator implemented on the CAEN firmware, which rejects triggers with too long time between the threshold and zero crossing. However noisy signals and varying rise times may prevent the efficient operation of the discriminator. Pile-up which affects the timing may also be rejected in a coincidence measurement by the coincidence criteria. In the simulations and measurements shown in this article, the rise time discriminator was turned off.

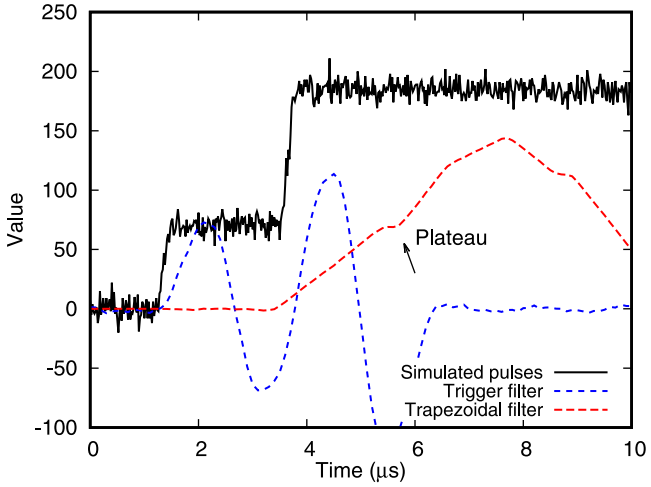

FIG. 5. Simulated pulses processed with the trigger filter and the trapezoidal filter with a rise time of 2 μs. Since the trapezoidal pulse height filter starts to plateau, the pulse height of the first event could have been determined correctly by the pulse height filter if the second event arrived any later. These pulses are however separated by the trigger filter and can be rejected by the pile-up inspector. This behavior is similar in simulations and in CAEN digitizer pulse height processing.

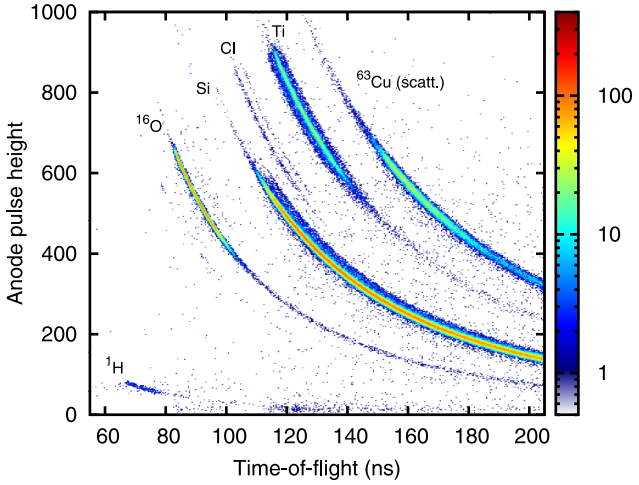

FIG. 6. Measured ToF–E histogram of the 80 nm thick TiO_2 sample with a 13.3 MeV $^{63}Cu^{7+}$ beam.

3. Timestamped list-mode data

The list of hits is sorted and the time-of-flight is determined by looking for the first T1 hit within the timing window before a T2 hit, as this is the same way the experimental apparatus determines the time-of-flight. Time-of-flight resolution was matched between simulations and measurements by applying gaussian noise to the list data. The output of this simulation is list-mode data, where timestamps are also subjected to similar jitter as the FPGA processing does with the digitizers.

4. List-mode coincidence

The timestamped list-mode data are processed with the same tools that are used in actual measurements. The coincidences between energy and time-of-flight are found by triggering a search from every energy event and accepting the first time-of-flight event within a specified time window.

III. EXPERIMENTAL

The experimental apparatus is described in Refs. 4, 7, and 24. The spectrometer is installed to a 41.3° angle relative to the beam and has a time-of-flight distance of 623 mm. The timing resolution is approximately 180 ps. The measured spectra were obtained using a 13.3 MeV $^{63}Cu^{7+}$ beam and mirror geometry. The sample was an 80 nm thick atomic layer deposited TiO_2 film on silicon substrate with some hydrogen and chlorine impurities in the film.

A. Verification of simulations

The simulations should match the observed behavior of the experimental apparatus so general observations can be made. As a reference, the TiO_2 sample was measured with an energy detector count rate of 1100 cps. The first 350 000 coincidence counts are shown in 2D histogram in Fig. 6.

In the measurements, the anode pulse shape suggested a much greater grid shielding inefficiency than predicted by the simulations. This effect has also been observed by others[12] and is attributed to capacitive coupling between the grid and the anode. By replacing the preamplifier connected to the grid electrode with a lower impedance path to ground, the coupling was greatly reduced, see Fig. 7. The simulations still seem to underestimate the shielding inefficiency, but this is most likely due to assumption of a flawless Frisch grid. The nonuniform spacing of the wires and wire sag could increase the inefficiency.

The rounding near the full amplitude of the anode pulse in Fig. 7 can be attributed to a long collection time of electrons originating near the window. The drift velocity is lower and the drift path to anode is longer for these electrons than those

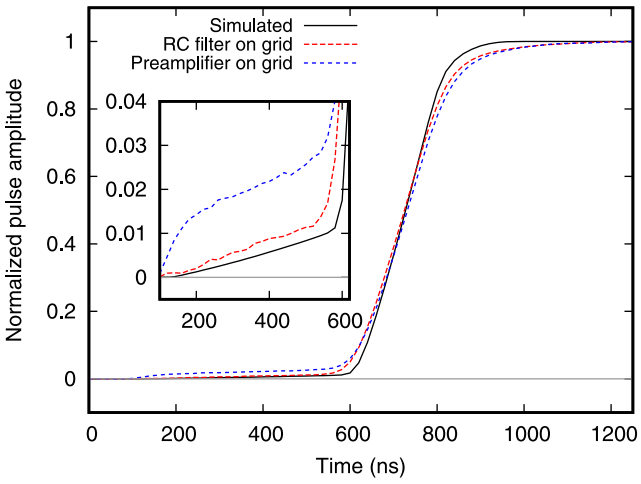

FIG. 7. Frisch grid shielding inefficiency and the influence of grid coupling. The simulated detector underestimates both the grid shielding inefficiency (inset) and the slow saturation of the collected charge. Measured and simulated pulses of oxygen recoils were normalized and averaged. The recoils were selected so that they have similar timestamp difference, i.e., same position in recoil plane.

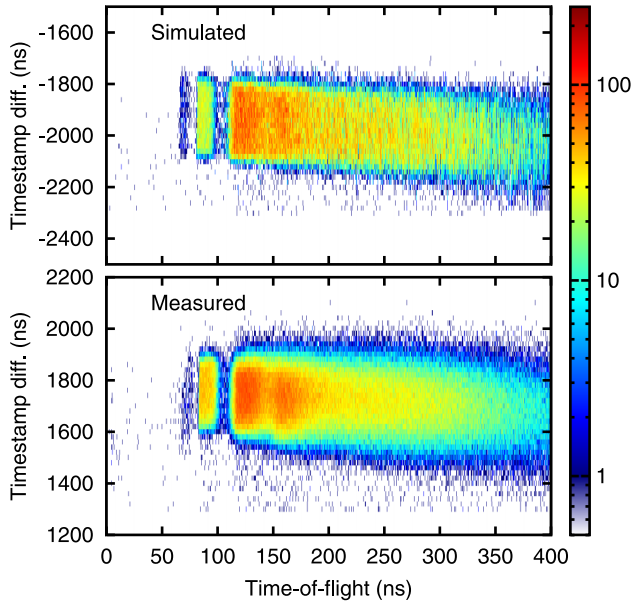

FIG. 8. Simulated and measured anode—T2 timestamp difference as a function of the time-of-flight. The width (vertical axis) of these curves is the difference in drift time between recoils entering the detector near either side of the entrance window.

produced deeper inside the detector, since the electric field near the window is low and not perpendicular to the electrodes.

The electric field near the window could differ from simulations, due to uncertainty in electrode alignment and charging of the silicon nitride window. The rise time of simulated pulses is generally somewhat shorter.

The time-of-flight–energy event timestamp difference is plotted as a function of the time-of-flight in Fig. 8. The recoils will need some ns to tens of ns to travel from T2 to the GIC and be stopped. The electrons created in the gas drift for a few hundred ns. The timestamp difference between T2 and GIC therefore varies primarily based on the drift time.

IV. RESULTS

A. GIC position sensitivity

The Frisch grid shielding inefficiency is one source of pulse height deficit, i.e., the improper shielding will result in position dependent reduction in observed anode pulse height, see Fig. 9. The residual anode pulse position sensitivity is affected by signal shaping. With the flat top duration of the trapezoid set longer than the drift time (>1 μs), the inefficiency is integrated completely. Lower flat top and rise time values will reduce the effect.

The measurement of position via drift time analysis was also studied using the simulations. Experimentally it was found[7] that the drift time as determined by timestamp differences was accurate enough for kinematic correction. The simulations show that the drift time is quite well linear for typical recoils from the sample and the position resolution is better than cathode–anode pulse height comparison. The reason for the linearity in the presence of window aberrations is due to the trigger filter of the digitizer, which uses a 50% constant fraction for timing. The window aberrations influence

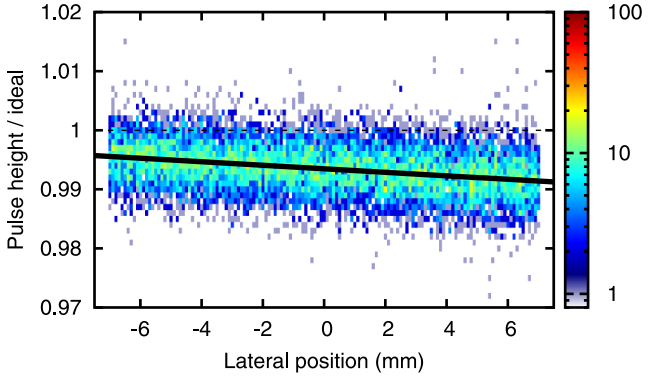

FIG. 9. Normalized anode pulse height vs lateral position, i.e., position at the detector window in the scattering plane (y), for approximately 4 MeV simulated oxygen recoils. There is a minor position dependent pulse height deficit associated with grid inefficiency.

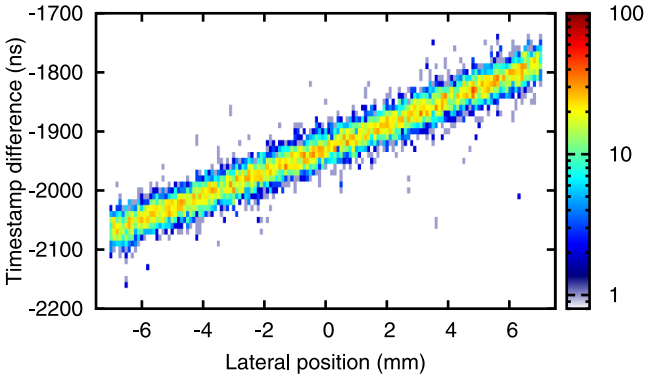

FIG. 10. Simulated anode—T2 timestamp difference as a function of lateral position of oxygen recoils at the entrance to the GIC (y). The drift time of electrons to the anode can be used to measure the recoil position.

only the latter part of the pulse, making the 50% value virtually immune to window effects.

In Fig. 10 the simulated timestamp difference of oxygen recoils has been plotted as a function of the lateral position at the GIC window. The position resolution is better than 2 mm given a timing resolution of 30 ns. Uncertainties in calibration can increase this further.

B. Mechanisms of background

Background is defined in this article to be any event where the energy (ionization signal) does not match the time-of-flight. Any event outside the 2D "bananas" is therefore clearly background, but this does not directly contribute to the results of any ERD analysis, since only the events inside the bananas are of relevance. However there can be background events also in these regions of interest, which becomes evident when trace concentrations are studied.

Different mechanisms producing background have been studied, some of these effects are related to the spectrometer as a whole, and others are single detector effects.

1. *Wrong time-of-flight–energy coincidence*

Wrong time-of-flight–energy coincidence background happens when two particles arrive consecutively in T1 and

in T2 and the first particle does not hit the energy detector. In this type of background, there is practically no correlation between energy and time-of-flight. Wide coincidence window makes this type of background important at high count rates. This is further exacerbated if there is a difference in solid angles between time-of-flight detectors and the energy detector.

Rejecting this type of background relies on the ability to resolve T1 and T2 hits within the time-of-flight window, which is possible with some TDCs and digitizers assuming minimal ringing in MCP signals. In the system simulated here, such rejection was not used.

2. Wrong T1-T2 coincidence

Wrong T1 and T2 coincidence happens when a recoil is overtaken by another after T1, but before T2. This results in the time-of-flight being shorter than what it was supposed to be for the first particle and longer than expected for the second. The energy signal might lead to pileup, unless one of the recoils does not hit the energy detector. This source of background is therefore quite similar to the previously discussed one.

Some low energy background is also created by recoils which have a time-of-flight longer than the timing window. In an inverted start system like the one here, a T1 hit might not be detected. If a T1 hit is provided by another particle, some random time-of-flight background is generated.

3. Pile-up

Two consecutive recoils can create a signal in the ionization chamber, which is falsely interpreted as a single hit.

In a 2D time-of-flight–energy histogram, the pile-up background mostly affects the region of heavy masses, especially if there are a lot of events from the substrate, such as silicon, or from scattered beam. Some of this background overlaps with wrong coincidence background as it is probable that events pile-up with events from substrate.

4. Scattering in GIC window or gas

Some background events are observed at low energies, but with apparently correct time-of-flight. The simulations show a similar behaviour. The energy loss in the simulations occurs when an atom of the entrance window is recoiled with some significant energy transfer. The energy lost by the first particle and one or more subsequent recoils in the window reduces the pulse height. Similar mechanism is possible in silicon detectors where the dead layer acts similarly to the window of the GIC.

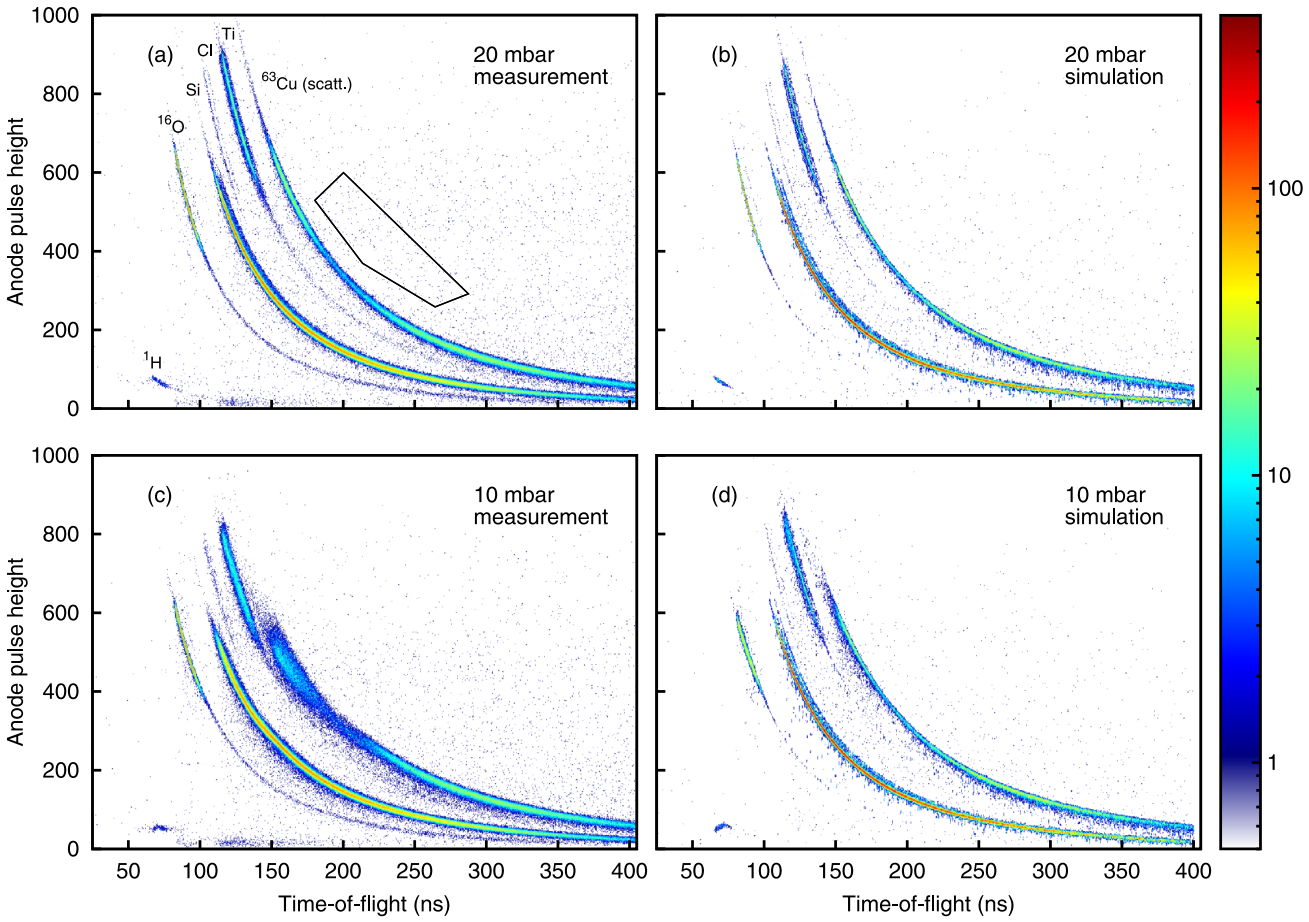

FIG. 11. Time-of-flight–E histograms of the TiO_2 sample. The histogram (a) was measured and (b) was simulated with 20 mbar GIC pressure, which is sufficient to stop all recoils in the active volume. The histogram (c) was measured and (d) was simulated with 10 mbar pressure. Each of the histograms has 350 000 events in total. The area inside the polygon in (a) corresponds to the "Heavy" region in Fig. 12.

Scattering in the detector gas contributes to background in $\Delta E - E$ detectors, as then the recoil causes an increase in signal at the ΔE portion.[5,26] For detectors with a single anode this effect is not observed. Large angle scattering in the gas can be reflected in the pulse shapes, but a major change in the pulse height requires either the recoil from the sample or the recoiled gas atom to hit an electrode or be ejected from the active volume. None of the measured digitized pulses could be unambiguously identified having a differing shape due to scattering in the gas.

When the pressure in the real GIC was reduced to below 10 mbar, a dramatic degradation in mass resolution was observed, see Fig. 11(c). The reproduction of this in simulations requires accurate stopping and straggling data. In Fig. 11(d) pressure of 10 mbar was simulated. The degradation of resolution is observed for recoils with the longest range. Even in this somewhat extreme case the degradation is mainly due to ions having a range longer than the anode length, not due to recoiling gas atoms.

The recoiling hydrogen atoms of the detector gas with a long enough range to hit the electrodes carry only a small amount of the total energy. The choice to use a constant W in spite of recoil cascades will slightly underestimate the recoiling hydrogen gas atom effect in the simulations.

5. Halos

The halo around light masses, most notably hydrogen, has been explained by MCP related effects.[4] The halo extends by only a few nanoseconds to either longer or shorter times-of-flight and is uncorrelated with the energy measurement; therefore, the halos rarely overlap with neighboring masses.

C. Background intensity

Assuming different count rates the relative intensities of different sources of background can be quantified in different regions of interest. In Fig. 11(b) a 2D ToF–E histogram is plotted with 10 000 cps T1 count rate. The number of events in different 2D regions, as the count rate was varied, is plotted in Fig. 12. The ^{1}H and ^{35}Cl regions are defined by a tight polygon around the masses of interest. The region labeled as "Heavy" covers an ideally empty part of the 2D histogram, where recoils heavier than Cu would be expected. The region is marked in Fig. 11. A linear increase of counts in the area of heavy masses can be observed. Both the wrong coincidences and pile-up are expected to increase linearly with increasing count rate. The chlorine "Cl" region covers both ^{35}Cl and ^{37}Cl, even though they can be separated in practice. If unnecessarily large polygon selections are made like in this case or elements with multiple unseparable isotopes are analyzed, it can be seen that the number of events inside the region at high count rates is exaggerated.

The increase of long time-of-flight wrong coincidences causes some short time-of-flight events to be rejected, which in turn reduces the number of observed counts in the hydrogen region, even though there is a small but increasing number of background events also in the same region.

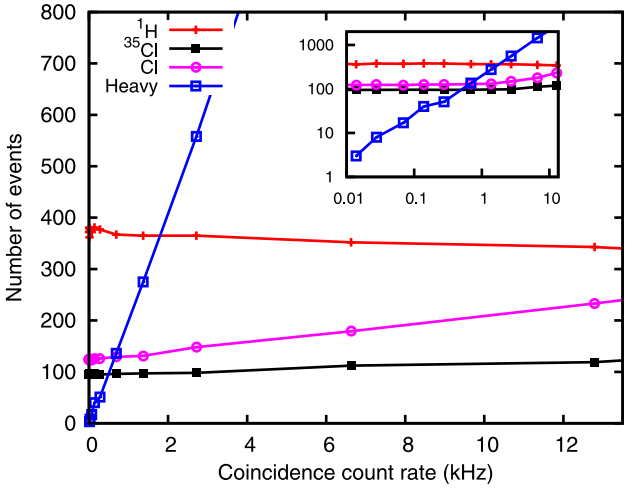

FIG. 12. Total number of events inside 2D regions with different count rates in the simulation. The regions are explained in the text. The same events were created with the same relative time differences between events. The variation in number of events is therefore purely due to count rate dependent mechanisms. The inset shows the same data on a different scale.

The measured histogram Fig. 11(a) shows much more background compared to the simulated one, Fig. 11(b). The difference is suspected to be partially due to low energy sputtered atoms, which cause a notable increase in T1 count rate in measurements.

V. CONCLUSIONS

A gas ionization chamber as the energy detector in a time-of-flight ERDA has unarguably improved the mass resolution of the spectrometer, justifying most of the limitations it possibly has.

These simulations provide valuable details on problems and limitations in the design and means to study them before detectors are built. The simulations provide further incentive to have as thin entrance window as possible, not merely because of the electronic energy loss and straggling in it, but also due to energy transfer to recoils within the window. Rise time of the anode pulses could be improved by increasing the electric field in the near-window region and can be achieved by biasing the window. This would likely improve the position resolution and shorter rise time would also reduce pile-up and wrong coincidences.

The simulations provided means to verify the position sensitivity of an existing GIC design and supported the results of previous experimental studies. The various mechanisms with which background is generated in time-of-flight–energy spectra were studied. Care should be taken with both data acquisition and ionization chamber design if count rates exceeding 1 kHz are to be used in low background measurements.

The gas ionization simulations could be improved by solving the electrostatic problems in three dimensions and implementing models which take into account the random motion of electrons in the gas. The fundamental knowledge of average ionization yields and variation in those for heavy ions of different energies in the detector gases would improve

the predictability of mass resolution of time-of-flight–energy spectrometers.

ACKNOWLEDGMENTS

This work was supported by the Finnish Funding Agency for Technology and Innovation Tekes through EU regional funds project HIUDAKE and Academy of Finland Center of Excellence in Nuclear and Accelerator Based Physics (Reference No. 251353).

[1]A. Razpet, P. Pelicon, Z. Rupnik, and M. Budnar, Nucl. Instrum. Methods Phys. Res., Sect. B **201**, 535 (2003).
[2]C. Kottler, M. Döbeli, F. Glaus, and M. Suter, Nucl. Instrum. Methods Phys. Res., Sect. B **248**, 155 (2006).
[3]S. Giangrandi, T. Sajavaara, B. Brijs, K. Arstila, A. Vantomme, and W. Vandervorst, Nucl. Instrum. Methods Phys. Res., Sect. B **266**, 5144 (2008).
[4]M. Laitinen, M. Rossi, J. Julin, and T. Sajavaara, Nucl. Instrum. Methods Phys. Res., Sect. B **337**, 55 (2014).
[5]G. Dollinger, M. Boulouednine, A. Bergmaier, T. Faestermann, and C. M. Frey, Nucl. Instrum. Methods Phys. Res., Sect. B **118**, 291 (1996).
[6]S. R. Walker, J. A. Davies, J. S. Forster, S. G. Wallace, and A. C. Kockelkoren, Nucl. Instrum. Meth. B **136-138**, 707 (1998).
[7]J. Julin, M. Laitinen, and T. Sajavaara, Nucl. Instrum. Methods Phys. Res., Sect. B **332**, 271 (2014).
[8]Z. Siketić, N. Skukan, and I. Bogdanović Radović, Rev. Sci. Instrum. **86**, 083301 (2015).
[9]W. Assmann, Nucl. Instrum. Methods Phys. Res., Sect. B **64**, 267 (1992).
[10]A. Bergmaier, G. Dollinger, and C. M. Frey, Nucl. Instrum. Methods Phys. Res., Sect. B **136-138**, 638 (1998).
[11]H. Timmers, T. R. Ophel, and R. G. Elliman, Nucl. Instrum. Methods Phys. Res., Sect. B **156**, 236 (1999).
[12]A. Göök, F.-J. Hambsch, A. Oberstedt, and S. Oberstedt, Nucl. Instrum. Methods Phys. Res., Sect. A **664**, 289 (2012).
[13]K. Arstila, T. Sajavaara, and J. Keinonen, Nucl. Instrum. Methods Phys. Res., Sect. B **174**, 163 (2001).
[14]N. Barradas, K. Arstila, G. Battistig, M. Bianconi, N. Dytlewski, C. Jeynes, E. Kótai, G. Lulli, M. Mayer, E. Rauhala, E. Szilágyi, and M. Thompson, Nucl. Instrum. Methods Phys. Res., Sect. B **262**, 281 (2007).
[15]J. F. Ziegler, M. D. Ziegler, and J. Biersack, Nucl. Instrum. Methods Phys. Res., Sect. B **268**, 1818 (2010).
[16]Z. He, Nucl. Instrum. Methods Phys. Res., Sect. A **463**, 250 (2001).
[17]D. C. Meeker, Finite Element Method Magnetics, 2016, http://www.femm.info/.
[18]ICRU, "Average energy required to produce an ion pair," ICRU Report 31 (ICRU, Washington, DC, USA, 1979).
[19]J. M. Valentine and S. C. Curran, Rep. Prog. Phys. **21**, 1 (1958).
[20]M. Chemtob, B. Lavigne, J. Chary, V. D. Nguyen, N. Parmentier, J. P. Noel, and C. Fiche, Phys. Med. Biol. **22**, 208 (1977).
[21]U. Fano, Phys. Rev. **70**, 44 (1946).
[22]G. Schultz and J. Gresser, Nucl. Instrum. Methods **151**, 413 (1978).
[23]R. Veenhof, Nucl. Instrum. Methods Phys. Res., Sect. A **419**, 726 (1998).
[24]J. Julin and T. Sajavaara, Nucl. Instrum. Methods Phys. Res., Sect. B **366**, 179 (2016).
[25]V. T. Jordanov and G. F. Knoll, Nucl. Instrum. Methods Phys. Res., Sect. B **345**, 337 (1994).
[26]A. N. James, K. A. Connell, and R. A. Cunningham, Nucl. Instrum. Methods Phys. Res., Sect. B **53**, 349 (1991).

PIV

CONCEPTUAL STUDY OF A HEAVY-ION-ERDA SPECTROMETER FOR ENERGIES BELOW 6 MEV

by

Jaakko Julin, Timo Sajavaara

Submitted to Nuclear Instruments and Methods in Physics Research Section B: Beam Interactions with Materials and Atoms

Conceptual study of a heavy-ion-ERDA spectrometer for energies below 6 MeV

Jaakko Julin*, Timo Sajavaara

University of Jyväskylä, Department of Physics, P.O. Box 35, FI-40014 University of Jyväskylä, Finland

Abstract

Elastic recoil detection analysis (ERDA) is a well established technique and it offers unique capabilities in thin film analysis. Simultaneous detection and depth profiling of all elements, including hydrogen, is possible only with time-of-flight ERDA. The chief limitations of time-of-flight ERDA are the beam induced sample damage and the requirement of a relatively large accelerator.

In this paper we propose a detector setup, which could be used with 3 MeV to 6 MeV medium heavy beams from either a single ended accelerator (^{40}Ar) or from a tandem accelerator (^{39}K). The detector setup consists of two timing detectors and a gas ionization chamber energy detector. Compared to use of very heavy low energy ions the hydrogen recoils with this beam have sufficient energy to be detected with current gas ionization chamber energy detector. To reduce the beam induced damage the proposed detector setup covers a solid angle larger than 1 msr, roughly an order of magnitude improvement over most time-of-flight ERDA setups. The setup could be used together with a small accelerator to be used for light element analysis of approximately 50 nm films.

The concept is tested with ^{39}K beam from a 1.7 MeV Pelletron tandem accelerator with the Jyväskylä ToF-ERDA setup. In addition to the measurements effects related to low energies and increase in the solid angle are simulated with Monte Carlo methods.

Keywords: ERDA, time-of-flight

1. Introduction

Time-of-flight ERDA has been used since 1976 [1] for light element analysis. Typical heavy ion with energies of approximately 1 MeV u^{-1} also allow medium heavy ions to be analyzed with time-of-flight techniques or ionization chambers [2]. The accelerator required for these beams are out of reach of many ion beam analysis (IBA) labs.

Low energy ERDA has been proposed and studied by others [3–6]. These systems are used with 2 MV or smaller tandem accelerators. The main limitations of these instruments compared to a higher energy system are reduced probing depth and mass resolution. When low energy very heavy ions such as ^{127}I or ^{197}Au are used the quantification of hydrogen is difficult because of the low recoiling energy.

Large solid angle $\Delta E - E$ gas ionization telescopes do not offer the mass resolution required for low energy measurements, so it seems the time-of-flight–energy spectrometer is the only practical choice. Moreover this avoids complicated calibrations of the spectrometer, as only the time-of-flight calibration and detection efficiency for hydrogen and some of the lightest elements must be accounted for.

We propose a compact large solid angle spectrometer design, backed up by Monte Carlo simulations and experiments with existing detectors. The design is intended to be used with incident beams with masses between 35 and 40, (e.g. ^{35}Cl, ^{39}K or ^{40}Ar) with energies around 5 MeV.

The design uses previously reported [7, 8] detector constructions, which are used successfully in routine analysis. The requirements for the accelerator system are lessened, enabling many labs access to a high resolution light element analysis tool.

Hydrogen detection and quantification is possible in the very low energy range of 70 keV to 300 keV. The larger solid angle than with previous designs is intended to mitigate the increase in sample damage due to use of lighter ions, while the position sensitive energy detector reduces kinematic broadening.

2. Proposed spectrometer design

The proposal relies on achieving sufficient mass resolving power, the ability to detect hydrogen and a depth resolution similar to existing ToF-ERDA. The solid angle of the proposal is then maximized. The significance of timing resolution on depth resolution is reduced at lower energies, therefore the distance between the timing detectors can be reduced, increasing the solid angle. A time-of-flight resolution of 200 ps is typical with spectrometers with a time-of-flight length of 50 cm to 100 cm. These typically use beams with 10 MeV or more energy. The design presented here should be able to offer similar depth resolution with lower energy beams. Even after accounting for grids reducing the geometric transmission in the timing detectors the solid angle should be much greater than 1 msr if the distance between the timing detectors is reduced to 30 cm.

*Corresponding author
Email address: jaakko.julin@jyu.fi (Jaakko Julin)

2.1. Accelerator requirements

The required beam can be provided by a variety of accelerators with different ion source designs. A single ended 3 MV accelerator can provide much more than 1 pnA of $^{40}Ar^{2+}$ to meet the upper range of energies considered in this study with the necessary flux even with conventional RF ion sources. Sufficient beam currents of $^{40}Ar^{3+}$ should also be possible with minor modifications [9], so that existing 2 MV accelerator systems are also usable. A miniaturized accelerator system could be built around a single ended system with 500 kV to 1000 kV terminal voltage if such a system is equipped with an ion source capable of producing higher charge state ions, such as Penning or electron cyclotron resonance (ECR) ion source.

A 1 MV tandem normally used with proton and He beams can in principle be used to produce 5 MeV to 6 MeV $^{39}K^{4+/5+}$, however the characteristics of such a system for heavy ion focusing etc. remain untested. Additionally the accelerator system should be equipped with a heavy ion source, such as a caesium sputtering ion source.

2.2. Geometry

In this design the time-of-flight length is 300 mm, much shorter than in any current published designs. The solid angle increases dramatically if the first timing detector is placed only 150 mm from the sample, allowing the energy detector to be placed approximately 500 mm from the sample. See Fig. 1.

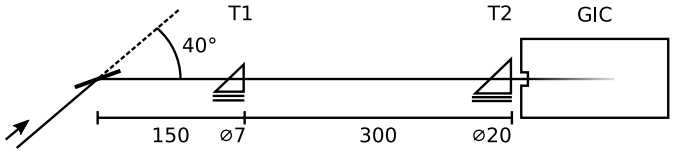

Fig. 1. Schematic of the proposed detector setup. The timing detectors T1 and T2 are placed close to each other and the sample, maximizing the detector solid angle.

The choice of the detector angle (θ) is a compromise between sensitivity, and mass and depth resolutions. Sensitivity improves at large angles, due to increasing cross sections. Mass resolution improves with recoil energy, which is increases at low angles. Depth resolution improves with longer effective ion and recoil path lengths at glancing angles. The sample inhomogeneity and multiple scattering also play a role in the choice of ideal geometry.

Most ERDA-telescopes are placed at an angle of 30° to 45° in respect to the beam direction. Quite often a fixed angle is preferred since the angle must be known well. Here an angle of 40° has been chosen so that the simulated and calculated results could be compared with the measurements performed with the existing spectrometer installed at 41.3° angle.

2.3. Timing detectors

The proposed timing detector design is based on the design by Busch et al [10], since these offer excellent timing resolution and simplicity of construction. The only drawback is the large number of various grids, which reduce the solid angle and increase the probability of background events.

T1 foil should be as thin as possible, but still offer adequate hydrogen detection efficiency. As thin as 0.5 $\mu g\,cm^{-2}$ diamond-like carbon (DLC) foils have been used for the start detector [4, 11]. The secondary electron yield can be enhanced by coating the foil with LiF [11] or Al_2O_3 [7]. Between 70 keV to 300 keV energies the detection efficiency with an Al_2O_3 coated 2 $\mu g\,cm^{-2}$ foil should be larger than 50%, depending on the MCP gain and electronics. The scattering of heavy recoils by the T1 carbon foil may limit the quantification of heavier recoils, this is discussed in Sect. 4.3.

T2 size is ultimately limited by the practical difficulties in mounting very large thin foils. Based on previous experience 5 $\mu g\,cm^{-2}$ carbon foil can be mounted on a frame with a 20 mm hole if supporting wires are used.

2.4. Gas ionization chamber

The gas ionization chamber should be designed to stop all recoils in the active volume. This means that either the length of the electrodes or the pressure of a GIC designed for higher energies can be reduced. The current Jyväskylä design [8] with an electrode length of 150 mm would be directly usable with a pressure of 10 mbar to 15 mbar.

At this pressure up to 400 mm^2 square entrance window is possible without supports, if 100 nm thick silicon nitride window is used. Alternatively patterned windows can be used, enabling the use of thinner silicon nitride. A thin entrance window will improve the mass resolution of the spectrometer and also reduce background [12].

3. Experimental studies

Experiments to study the feasibility of low energy ERDA were performed with the 1.7 MV Pelletron 5SDH-2 in Jyväskylä Accelerator Laboratory.

In the time-of-flight spectrometer [7, 8] the time-of-flight length is 623 mm and the solid angle is limited by a 200 mm^2 energy detector window approximately 100 cm from the sample. The T1 detector has a 3 $\mu g\,cm^{-2}$ carbon foil.

3.1. Mass and depth resolution

All light elements H, Li, C, N and O and their isotopes can be separated with ease even with 4 MeV beam, see Fig. 2. Even the small Cl impurity in the Li_2CO_3 sample can be detected, although the quantification is affected by background from scattered ^{39}K. Depth profiles from measurement with 5.1 MeV beam of the same sample are presented in Fig. 3.

3.2. Hydrogen detection and analysis

Hydrogen down to 80 keV can be detected with existing ionization chambers, but the energy calibration will not be perfectly linear. Also the resolution of the GIC will limit the resolution of the hydrogen efficiency calibration. Since the detection efficiency near the hydrogen stopping maximum is strongly energy dependent [13], the uncertainties associated with the energy resolution and calibration will be large.

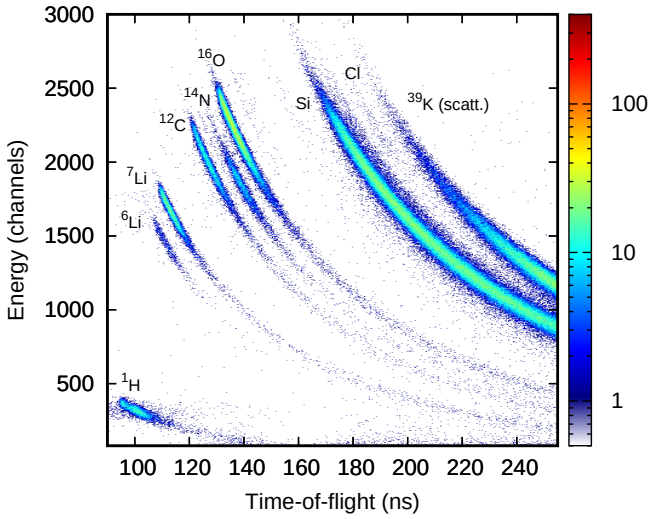

Fig. 2. 57 nm thick Li_2CO_3 film on Si measured with 4 MeV ^{39}K beam. The mass resolution is limited by the energy resolution of the GIC.

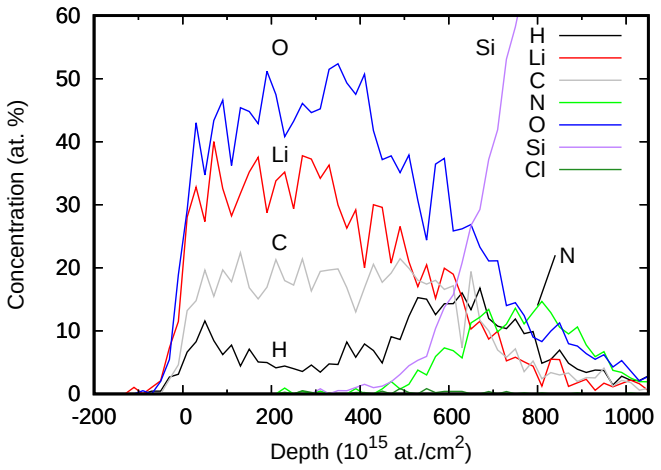

Fig. 3. 57 nm thick Li_2CO_3 film on Si measured with 5.1 MeV ^{39}K beam and 10° tilt between the beam and the sample surface. The depth resolution is affected by the roughness of the sample.

The efficiency calibration of the spectrometer involves measuring the fraction of recoils detected by all the detectors to recoils detected by the energy detector [13], which is assumed to have a 100% efficiency above a certain threshold energy. For this purpose the energy calibration of the GIC must be monotonous, i.e. similar pulse heights may not be created by recoils with two different energies.

If another detector, such as a silicon detector, is placed after the GIC it is possible to calibrate the detection efficiency of the time-of-flight detectors over a broad energy range if the GIC detector gas is removed. The solid angle of such a silicon detector would not match the GIC solid angle, so deviations due to pinholes at the edges of timing detector carbon foils etc. may cause deviations in the calibration. Such differences would however be evident in the common energy range where either the silicon detector and the GIC can be used to determine the detection efficiency.

Certified hydrogen reference material with 13.9% hydrogen in silicon, deposited using chemical vapor deposition (CVD) [14] was measured with beams of ^{39}K with various energies. The hydrogen concentration was determined using Potku [15] using cross section corrections by Andersen et al. [16]. The results are plotted in Fig. 4. The hydrogen concentration from the same depth interval can be seen to increase when measured using lower incident energy. The results may vary due to inaccuracies in the stopping forces in silicon for H and Si recoils. Other reasons for this are discussed in Sec. 4.3.

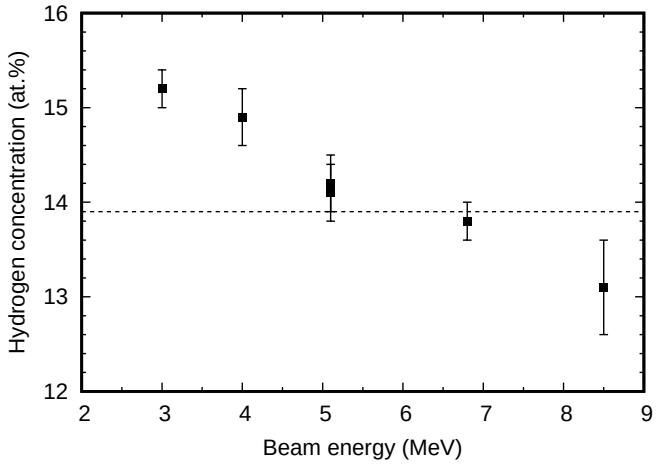

Fig. 4. Hydrogen concentration of the reference sample [14] measured with beams of ^{39}K with different energies. The error bars indicate the statistical uncertainty. The dashed line represents the nominal H concentration of the sample (13.9 at.%). The 5.1 MeV point has been measured twice, both as the first and the last measurement in order to monitor possible changes in the sample by the ion beam bombardment.

4. Simulations

4.1. Geometrical effects

Path length differences due to detector geometry $\frac{\Delta L}{L}$ affects velocity resolution of the spectrometer. If T1 and T2 foils are assumed to be parallel and $L = 300$ mm the largest deviation assuming a point-like beam spot is neglible, $\frac{\delta L}{L} \approx 1.00025$. This figure does not include scattering from the carbon foils. The perfect correction for different path lengths requires two 2D position sensitive detectors, and in practice also very careful alignment of the detectors.

More importantly large solid angle geometry causes kinematic broadening due to scattering angle variations. This contribution can be reduced with a position sensitive detector. When we consider a monoenergetic beam to recoil surface atoms with a nominal centerline time-of-flight of 100 ns the actual time-of-flight distribution as a function of T2 lateral position is plotted in Fig. 5. This distribution includes variations due to different recoiling angles (θ, ϕ), and time-of-flight length differences. The beam was assumed to be collimated to a 1 mm (horizontal) by 2 mm (vertical) rectangle, which projected on to a sample placed 20° relative to the beam creates a spot of 3 mm by 2 mm on the sample.

The 1D position x at T2 can be used as a measure of the true recoil angle θ around the centerline ideal recoil angle $\theta_{\text{center}} = 40°$ with simple geometry:

$$\theta = \theta_{\text{center}} + \arctan\left(\frac{x}{d_{\text{T2}}}\right), \quad (1)$$

where d_{T2} is the distance of the T2 detector from the sample.

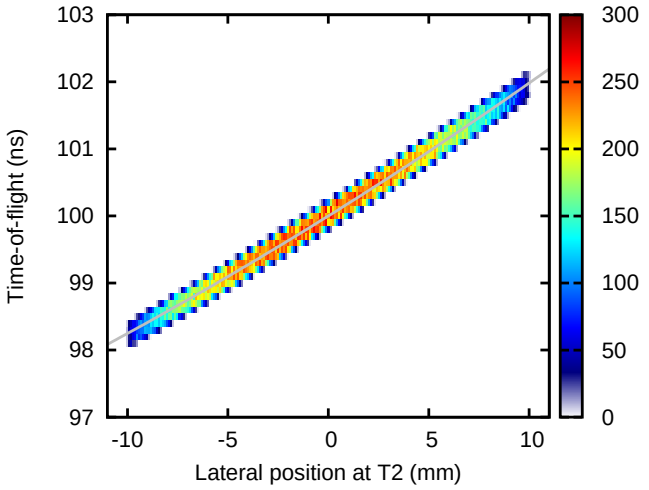

Fig. 5. Calculated time-of-flight of surface recoils created by a monoenergetic incident beam as a function of the lateral (scattering plane) coordinate of the second timing detector (T2). The spectrometer centerline time-of-flight corresponds to 100 ns. The kinematic broadening can be compensated well with one dimensional position sensitivity, i.e. the measured lateral position x is assumed to affect the recoiling angle directly, see Eq. 1. The plotted line is the expected time-of-flight given one dimensional corrections.

These geometrical effects scale linearly with time-of-flight. For recoils originating beneath the surface of the sample the geometry affects in a more complicated manner due to path length differences in the sample. The fundamental limit to depth resolution will eventually be energy straggling. The effective timing resolution (standard deviation) at surface with the specified spot size and geometry can be predicted using formula

$$\delta t = \sqrt{\left(\frac{200\,\text{ps}}{2.35}\right)^2 + (0.00136 \cdot t)^2}, \quad (2)$$

for a time-of-flight t, assuming the position sensitivity is 1 mm at T2. While the kinematic broadening after corrections is non-negligible for the time-of-flight range of interest (30 ns to 150 ns), the total effective resolution is comparable to or better than in many setups where position sensitive detectors are not used.

4.2. Depth resolution

In order to get an understanding of the significance of multiple scattering, kinematic broadening and how well it could be compensated in practice simulated were made using a modified version of MCERD [12, 17].

This simulated data was fed to an analysis program Potku [15] to extract the depth profiles shown in Fig. 6, which correspond to the depth profiles used in the simulations, but with many effects contributing to the depth resolution. The sample was tilted 10° in respect to the incoming beam. A 5.1 MeV ^{39}K beam with a dose of 10^{11} particles (16 pnC) was used in the simulations, corresponding to approximately 28 000 oxygen counts. If the energy detector count rate is kept below 2 kHz this measurement is possible in 10 minutes with a beam current below 30 ppA.

4.3. Scattering

Low energy heavy ions have issues with multiple scattering in the sample and large angle scattering in the detector foils [6]. Scattering in the T1 carbon foil leads to reduction in detection efficiency, since some recoils miss the T2 or energy detector. The distance between the timing detectors increases this effect. The apparent enhancement of H concentration at lower energies seen in Fig. 4 is partially due to this, since the silicon is more likely to scatter in the T1 carbon foil than hydrogen. In order to quantify this effect MCERD simulations were performed. The scattering from carbon foils did not enhance the H concentration results more than 0.2 percentage points when 4 MeV or higher energies were used, with the proposed 2 μg cm^{-1} T1 foil the effect will be even smaller.

5. Discussion and conclusions

The presented setup can be used to give a complete elemental depth profiles of thin film samples containing mostly light elements. Light elements including H, C, N, and O can be unambiguously identified.

The high solid angle combined with high cross sections provides means to study sensitive materials. Quantitative depth profiling of approximately 50 nm thick films is possible, although at lowest energies some corrections might be necessary. Quantification of heavy elements is not recommended, because of the multiple scattering and scattering in the detector foils.

The low energy and low beam current requirements combined with a compact design open possibilities to use this spectrometer design as a part of a low-cost time-of-flight ERDA setup.

6. Acknowledgments

This work was supported by Academy of Finland Center of Excellence in Nuclear and Accelerator Based Physics (Ref. 251353). The authors would like to thank Amund Ruud and Ola Nilsen from the University of Oslo for providing the Li_2CO_3 sample.

References

[1] J. L'Ecuyer, C. Brassard, C. Cardinal, J. Chabbal, L. Deschênes, J. P. Labrie, B. Terreault, J. G. Martel, R. St.-Jacques, An accurate and sensitive method for the determination of the depth distribution of light elements in heavy materials, J. Appl. Phys. 47 (1976) 381.
URL http://dx.doi.org/10.1063/1.322288

[2] W. Assmann, Ionization chambers for materials analysis with heavy ion beams, Nucl. Instrum. Meth. B 64 (1992) 267.
URL http://dx.doi.org/10.1016/0168-583X(92)95478-A

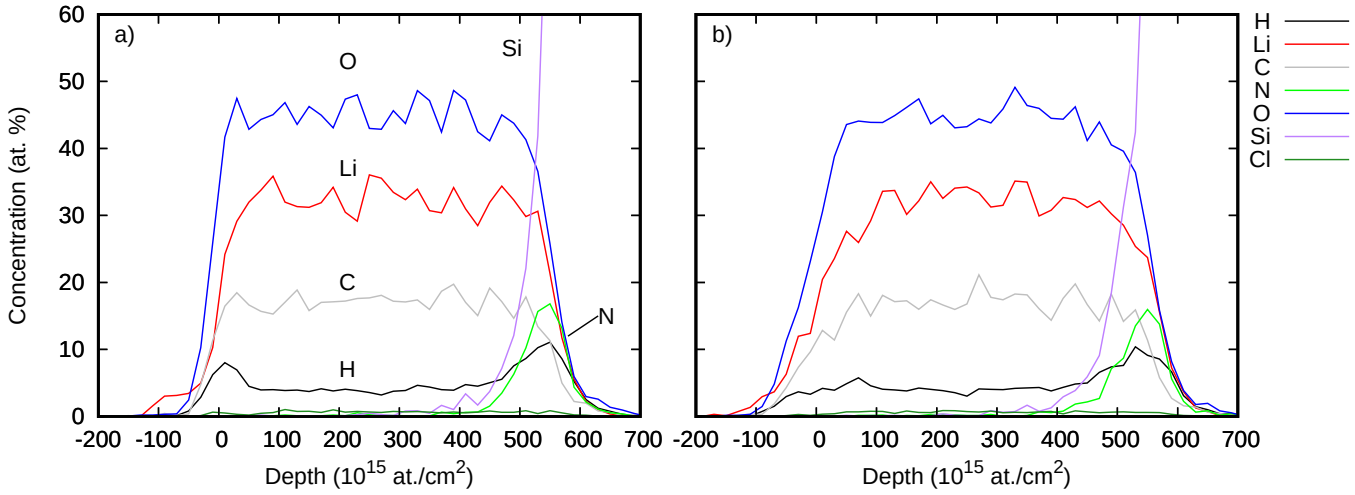

Fig. 6. Depth profiles from simulated data with 5.1 MeV ^{39}K beam. MCERD and gas ionization chamber simulations were used to model the proposed setup. One dimensional position sensitivity was used in the analysis in (a), while no position sensitivity was used in (b). The Li_2CO_3 sample was assumed to be smooth and homogeneous and contain some H at the surface and H and N at the interface, similarly to depth profiles in Fig. 3. With the position sensitivity the depth resolution near the surface is comparable to the existing setup.

[3] M. Döbeli, C. Kottler, F. Glaus, M. Suter, ERDA at the low energy limit, Nucl. Instrum. Meth. B 241 (2005) 428.
URL http://dx.doi.org/10.1016/j.nimb.2005.07.090

[4] C. Kottler, M. Döbeli, F. Glaus, M. Suter, A spectrometer for low energy heavy ion ERDA, Nucl. Instrum. Meth. B 248 (2006) 155.
URL http://dx.doi.org/10.1016/j.nimb.2006.02.013

[5] S. Giangrandi, K. Arstila, B. Brijs, T. Sajavaara, A. Vantomme, W. Vandervorst, Depth resolution optimization for low-energy ERDA, Nucl. Instrum. Meth. B 261 (2007) 512.
URL http://dx.doi.org/10.1016/j.nimb.2007.03.093

[6] S. Giangrandi, T. Sajavaara, B. Brijs, K. Arstila, A. Vantomme, W. Vandervorst, Low-energy heavy-ion TOF-ERDA setup for quantitative depth profiling of thin films, Nucl. Instrum. Meth. B 266 (2008) 5144.
URL http://dx.doi.org/10.1016/j.nimb.2008.08.018

[7] M. Laitinen, M. Rossi, J. Julin, T. Sajavaara, Time-of-flight – Energy spectrometer for elemental depth profiling – Jyväskylä design, Nucl. Instrum. Meth. B 337 (2014) 55.
URL http://dx.doi.org/10.1016/j.nimb.2014.07.001

[8] J. Julin, M. Laitinen, T. Sajavaara, Time-of-flight ERD with a 200 mm2 Si3N4 window gas ionization chamber energy detector, Nucl. Instrum. Meth. B 332 (2014) 271.
URL http://dx.doi.org/10.1016/j.nimb.2014.02.076

[9] E. J. Knystautas, Extending the energy range of a 7 MV Van de Graaff using triply-charged beams: Applications to neon and argon ions, IEEE T. Nucl. Sci. 26 (1979) 1470.
URL http://dx.doi.org/10.1109/TNS.1979.4330413

[10] F. Busch, W. Pfeffer, B. Kohlmeyer, D. Schüll, F. Pühlhoffer, A position-sensitive transmission time detector, Nucl. Instrum. Methods 171 (1980) 71.
URL http://dx.doi.org/10.1016/0029-554X(80)90011-7

[11] Z. Siketić, I. Bogdanović Radović, M. Jakšić, Development of a time-of-flight spectrometer at the Ruder Bošković Institute in Zagreb, Nucl. Instrum. Meth. B 266 (2008) 1328.
URL http://dx.doi.org/10.1016/j.nimb.2007.12.070

[12] J. Julin, K. Arstila, T. Sajavaara, Simulations on time-of-flight ERDA spectrometer performance, Submitted to Rev. Sci. Instrum.

[13] Y. Zhang, H. J. Whitlow, T. Winzell, I. F. Bubb, T. Sajavaara, K. Arstila, J. Keinonen, Detection efficiency of time-of-flight energy elastic recoil detection analysis systems, Nucl. Instrum. Meth.B 149 (1999) 477.
URL http://dx.doi.org/10.1016/S0168-583X(98)00963-X

[14] U. Reinholz, W. Bremser, K.-W. Brzezinka, E. Strub, H.-P. Weise, S. Merchel, A thin-layer reference material for hydrogen analysis, Nucl. Instrum. Meth. B 266 (2008) 2418.
URL http://dx.doi.org/10.1016/j.nimb.2008.03.015

[15] K. Arstila, J. Julin, M. Laitinen, J. Aalto, T. Konu, S. Kärkkäinen, S. Rahkonen, M. Raunio, J. Itkonen, J.-P. Santanen, T. Tuovinen, T. Sajavaara, Potku – new analysis software for heavy ion elastic recoil detection analysis, Nucl. Instrum. Meth. B 331 (2014) 34.
URL http://dx.doi.org/10.1016/j.nimb.2014.02.016

[16] H. H. Andersen, F. Besenbacher, P. Loftager, W. Möller, Large-angle scattering of light ions in the weakly screened Rutherford region, Phys. Rev. A 21 (1980) 1891.
URL http://dx.doi.org/10.1103/PhysRevA.21.1891

[17] K. Arstila, T. Sajavaara, J. Keinonen, Monte Carlo simulation of multiple and plural scattering in elastic recoil detection, Nucl. Instrum. Meth. B 174 (2001) 163.
URL http://dx.doi.org/10.1016/S0168-583X(00)00435-3